Imperial College of Science, Technology and Medicine
Faculty of Natural Science
Department of Physics
Centre For Cold Matter

Developing a Transportable Quantum Inertial Sensor

Henry George Sewell

Supervisor- Joseph Cotter
Co-supervisor- Ben Sauer

Submitted in part fulfilment of the requirements for the degree of Doctor of Philosophy in Physics of the University of London and the Diploma of Imperial College, February 2024

Imperial College London

Declaration

I declare that this thesis has been composed solely by myself and that it has not been submitted, in whole or in part, in any previous application for a degree. Except where stated otherwise by reference or acknowledgement, the work presented is entirely my own.

Copyright

The copyright of this thesis rests with the author. Unless otherwise indicated, its contents are licensed under a Creative Commons Attribution-Non Commercial 4.0 International Licence (CC BY-NC). Under this licence, you may copy and redistribute the material in any medium or format. You may also create and distribute modified versions of the work. This is on the condition that: you credit the author and do not use it, or any derivative works, for a commercial purpose. When reusing or sharing this work, ensure you make the licence terms clear to others by naming the licence and linking to the licence text. Where a work has been adapted, you should indicate that the work has been changed and describe those changes. Please seek permission from the copyright holder for uses of this work that are not included in this licence or permitted under UK Copyright Law.

Acknowledgements

Firstly, I would like to thank my supervisor, Joe Cotter, for his guidance throughout my PhD, both as an academic and with his advice about life the universe and everything. Your relentless optimism and support has been a huge boost throughout this experiment.
I would also like to thank all of the members of CCM, and particularly the navigator group who have helped me throughout my PhD. Aisha has been like a second supervisor to me and has been an amazing teacher and sounding board for my many troubles and complaints. Thank you to Xiaxi, Shane, Nicola, Theo, Val, Rob, and Andy for your help and support whenever I have needed it. Thank you to Guanchen, who has been like a brother to me as we have gone through our PhDs together. Helping to diagnose each other's (many) experimental problems has made me a much better physicist. Good luck to the PhD students following me as well: Shengan, Keyu, Bryony, Alex, and Alessia.
Thank you to Sanja for your amazing day-to-day support, and for generally being the glue that holds the entire research group together.
Particular thanks must go to Jon and Dave, who through the various field trials, showcase events, and laboratory moves, have gone above and beyond what could be expected in support of this experiment. (Also for your advice about the best places for a full English breakfast).
Thank you for the support of Joseph, Rahul, and Sahani throughout the building of the experiment. Your help and advice has been invaluable at every stage of my PhD.
Finally, I would like to thank my friends and family for the support they have given me over the last four years. Thank you Alfie for supplying me with an endless supply of unusual physics questions, most of which I still probably haven't given good answers to. Thank you to Manon for bearing the brunt of my stress and anxiety for the whole of my time on this experiment. You have been my rock during this whole process and I cannot thank you enough for your unwavering support and encouragement.

In memory of Roy Eric Pulling
(1945-2021)

"Laws which are consistent in theory often prove chaotic in practice"
Mark Corrigan/Napoleon Bonaparte

Contents

List of Figures **xiv**

Abstract **xv**

Preface **xviii**

1 Introduction **1**
1.1 Navigation . . . 1
1.1.1 Global Navigation Satellite Systems (GNSS) . . . 1
1.1.2 Inertial Navigation . . . 2
1.2 Interferometry . . . 4
1.2.1 Matter-Wave Interferometry . . . 6
1.3 Thesis Outline . . . 7

2 Atom Interferometry **9**
2.1 Note on Atomic Transition Labels . . . 10
2.2 Stimulated Raman Interactions . . . 10
2.3 Atom-Light Interaction . . . 12
2.3.1 π and $\pi/2$ Pulses- . . . 15
2.3.2 Three Pulse Interferometer . . . 16
2.3.2.1 Interferometer Phases . . . 17
2.3.2.2 Acceleration Sensitivity . . . 18
2.3.3 Interferometer Contrast . . . 18
2.4 Raman Transition Implementation . . . 19
2.4.1 Polarisation Requirement . . . 19
2.4.1.1 Telescope Polarisation . . . 21
2.4.2 Raman Beam Geometry . . . 23
2.4.3 Collimation Requirement . . . 24
2.4.4 Raman Mirror Alignment . . . 27
2.4.5 The Double Interferometer . . . 27
2.4.6 Differential Light Shift . . . 28

2.4.6.1 Uncancelled Differential Light Shift and Beam Misalignment . . . 29

3 Atom Preparation **31**
3.1 Atom Trapping and Cooling . . . 31
3.1.1 1D MOT Theory . . . 32
3.1.2 2D+ MOT . . . 33
3.1.2.1 2D MOT . . . 33
3.1.2.2 Push Beam . . . 34
3.1.3 3D MOT . . . 35
3.1.4 Sub-Doppler Cooling . . . 36
3.1.4.1 Sisyphus Cooling . . . 36
3.1.4.2 Molasses Sequence . . . 38
3.1.5 Atom Launch . . . 40
3.1.5.1 Moving Molasses . . . 41
3.2 State Selection . . . 42
3.2.1 Preparation Scheme . . . 42
3.2.2 Stage 1 - Pumping Atoms Into $|F = 1\rangle$ . . . 44
3.2.3 Stage 2 - Pumping Atoms into $|F = 1, m_F = 0\rangle$ . . . 44
3.2.4 Velocity Selection . . . 44
3.2.4.1 Stage 3 - Microwave Transfer . . . 45
3.2.4.2 Stage 4- $|F = 1\rangle$ Blowaway . . . 45
3.2.4.3 Stage 5 - Velocity Selective Pulse . . . 46
3.2.4.4 Stage 6 - $|F = 2\rangle$ Blowaway . . . 47

4 Experimental Apparatus **48**
4.1 Apparatus Overview . . . 48
4.2 Laser System and Optical Distribution . . . 49
4.2.1 Laser System . . . 49
4.2.2 Laser Stabilisation . . . 50
4.2.2.1 Vapour Cell Lock . . . 50
4.2.2.2 Phase Lock . . . 53
4.2.3 Laser and Lock Stability . . . 54
4.2.3.1 Vapour-Cell Lock Photodiode Difference Signal 54
4.2.3.2 Mixed Phase Lock Beat Signal . . . 55
4.2.3.3 Master Output Power . . . 55
4.2.3.4 Apprentice Output PD . . . 56
4.3 Acousto-Optic Modulators . . . 57
4.4 System Electronics . . . 57
4.4.1 Direct Digital Synthesis (DDS) . . . 57
4.5 System Control Software . . . 58

4.5.1 MOTMaster and AxelHub . . . 58
4.5.2 DDS LabVIEW . . . 58
4.6 Science Chamber . . . 59
4.6.1 Achieving UHV . . . 60
4.7 Ex-vacuo Hardware . . . 61
4.7.1 Atom Source and 2D MOT . . . 61
4.7.1.1 3D MOT Coils . . . 62
4.7.1.2 3D MOT Optics . . . 63
4.7.2 Bias Magnetic Fields and Magnetic Field Compensation 64
4.7.3 Microwave Horn . . . 66
4.7.4 State Sensitive Detection . . . 67
4.7.4.1 Detection Apparatus . . . 67
4.7.4.2 Photodiode Signal to Atom Number . . . 68
4.7.4.3 Detection Sequence . . . 69
4.8 In-vacuo Hardware . . . 72
4.8.1 Raman Telescope . . . 73
4.8.2 Raman Mirror and Classical Accelerometer . . . 74
4.9 System Mounting and Transportability . . . 76

5 Results **77**
5.1 Atom Trapping and Cooling . . . 77
5.1.1 2D+ MOT . . . 77
5.1.2 3D MOT . . . 80
5.1.3 Sub-Doppler Cooling . . . 85
5.1.3.1 Atom Temperature . . . 85
5.1.3.2 Moving Molasses . . . 87
5.2 Hyperfine Spectra . . . 90
5.2.1 Raman Spectrum . . . 90
5.2.2 Microwave Spectrum . . . 91
5.3 State Selection . . . 92
5.3.1 State Selection Stage 1 . . . 93
5.3.2 State Selection Stage 2 . . . 93
5.3.3 State Selection Stage 3 . . . 95
5.3.4 State Selection Stage 4 . . . 96
5.3.5 State Selection Stage 5 . . . 96
5.3.6 State Selection Stage 6 . . . 98
5.4 Stimulated Raman Interactions . . . 99
5.4.1 The Raman Beam . . . 99
5.4.1.1 Collimation . . . 99
5.4.1.2 Polarisation . . . 100
5.5 Rabi Ocscillations . . . 103

5.5.1 Effect of Atom Cloud Temperature . . . 103
5.5.2 Velocity Selection . . . 104
5.6 Three-pulse Interferometry . . . 104
5.6.1 Interference Fringes . . . 105
5.6.1.1 Mirror Vibrations . . . 107

6 Field Trials **111**
6.1 The Navy POD . . . 111
6.1.1 Mounting . . . 112
6.2 Static Field Trial . . . 113
6.3 Sea trials . . . 115
6.3.1 XV Patrick Blackett . . . 115
6.3.2 Vibrations . . . 117
6.3.3 Laser and Laser Lock Noise . . . 120
6.3.4 Magnetic Fields . . . 121
6.3.5 Laser Cooling and Cloud Temperature . . . 122
6.3.6 Coherent Control . . . 125
6.4 Ruggedness . . . 125
6.4.1 Raman Mirror Mount . . . 126
6.4.2 Raman Telescope . . . 127
6.5 Lessons Learned During Sea Trials . . . 128

7 Conclusion and Future Work **130**
7.1 Summary of this work . . . 130
7.2 Outlook . . . 131
7.2.1 Current Landscape of Atom Interferometry for Navigation . . . 131
7.2.2 Next steps for this sensor . . . 131

Bibliography **132**

List of Figures

1 Experiment vacuum chamber with axes definitions used throughout the thesis. xvi

1.1 The basic function of GNSS 2
1.2 Two different types of classical accelerometer 3
1.3 Diagram of Young's double slit experiment with sunlight. . . . 4
1.4 Diagram of an optical Mach-Zehnder interferometer. 5
1.5 The neutron interferometer used in the COW experiment . . . 5
1.6 Experimental setup of the atom interferometer based on stimulated Raman transitions used by Kasevich and Chu. 6

2.1 Time-space diagram of a three-pulse atom interferometer. . . . 9
2.2 Definitions of σ^+ and σ^- transitions used in this thesis. 10
2.3 Energy level diagrams for the full three-level treatment of a two photon stimulated Raman transition, and a simplified two level atomic system. 11
2.4 Time-space diagram showing atom trajectories in a three pulse interferometer. 16
2.5 Energy levels in the ^{87}Rb D_2 line and the Raman transitions that are driven in this experiment. 20
2.6 Beam polarisation in each section of the Raman beam. 21
2.7 Schematic of quarter waveplate axes and deviation from perfect alignment. 22
2.8 Simulated Raman beam intensities during each interferometer pulse for a 2.5 cm wide Gaussian beam, and the truncated Gaussian beam used in the experiment. 24
2.9 Acceleration error against Raman beam divergence angle. . . . 26
2.10 Effect of Raman mirror misalignment on the effective k-vector of the Raman beam. 26
2.11 Time-space diagram showing the atom position and energy and momentum states for the double interferometer. 28
2.12 The differential light shift and magic ratio versus Raman beam detuning. 29

2.13 The ratio of Master and Apprentice beam intensities for a 1° misalignment of the Raman mirror. 30

3.1 Schematic of a MOT in one dimension, and an energy level diagram showing the cooling and repump transitions used in this experiment. 32
3.2 CAD design for science and CAS chambers and 2D MOT schematic. 33
3.3 Schematic of the 3D MOT. 35
3.4 Working principle of Sisyphus cooling. 36
3.5 Experimental sequence during 3D MOT loading and molasses ramps. 39
3.6 Comparison of theoretical relative Raman beam intensities during each interferometer pulse for a 25 ms interferometer with and without a vertical launch. 40
3.7 Experimental sequence during moving molasses. 41
3.8 Different stages of atom preparation during the experiment. . 43
3.9 Excitation probability of 10 µs and 100 µs Raman pulses, and Maxwell-Boltzmann probability distribution for 5 µK and 146 µK atom clouds. 46

4.1 Summary of all light and microwave inputs, and all magnetic field coils on the main science chamber. 48
4.2 Summary of laser light powers and frequencies used in the demonstrator. 49
4.3 Laser frequencies used in the experiment referenced to ^{87}Rb energy levels. 50
4.4 Distribution of light within the laser and optics layers of the experiment. 51
4.5 Saturated absorption spectroscopy apparatus and the photodiode difference signal used to lock the Master laser 52
4.6 Diagram of the phase-lock. 53
4.7 Typical vapour cell lock difference signal time series and power spectrum data taken in the laboratory. 54
4.8 Typical MPLB signal time series and power spectrum data taken in the laboratory. 55
4.9 Typical Master output power time series and power spectrum data taken in the laboratory. 56
4.10 Typical Apprentice output power time series and power spectrum data taken in the laboratory. 56
4.11 The science chamber 59

4.12 Image of vacuum chamber inside an oven. 60
4.13 CAD designs showing the 2D MOT source cell and optics, and how it is mounted to the main science chamber. 62
4.14 Position and dimensions of the MOT coils used to create the spherical quadrupole field for atom trapping. 62
4.15 Schematics showing the design of the 3D MOT collimators used in the experiment. 63
4.16 Cut-throughs of the CAD designs for the vacuum chamber. . . 64
4.17 CAD designs showing the positions of flux gates and bias coils. 65
4.18 Image detailing how errors arise in the current magnetic field compensation system. 66
4.19 CAD design of the vacuum chamber showing the microwave horn position. 67
4.20 Excitation beam path and detection optics positions. 67
4.21 Atom number measurement using fluorescence detection. . . . 70
4.22 Typical fluorescence detection signal recorded on a photodiode using two vertical MOT beams or the dedicated excitation beam. 71
4.23 Transition strengths for all possible $|F = 2\rangle$ and $|F' = 3\rangle$ transitions. 72
4.24 CAD drawing of the in-vacuum Raman optics. 72
4.25 Ray tracing diagram of Raman telescope. 73
4.26 CAD design for the Raman mirror 74
4.27 Raman mirror alignment method. 74
4.28 CAD designs for racks used to transport each part of the experiment. 75

5.1 Camera image of the 2D MOT. 77
5.2 3D MOT atom number against 2D MOT power and frequency. 78
5.3 3D MOT atom number against push beam power. 79
5.4 3D MOT atom number against push beam frequency. 80
5.5 Graphs showing 3D MOT magnetic field compared with theory. 81
5.6 Magnetic field during MOT coil switch off without reverse current. 82
5.7 Magnetic field during MOT coil switch of for different reverse currents. 83
5.8 3D MOT atom number against bias coil magnetic field. 83
5.9 3D MOT atom number against 3D MOT cooling beam power. 84
5.10 3D MOT loading curve. 85
5.11 Camera images of atom cloud falling under gravity. 85
5.12 Atomic cloud width over time. Used to measure cloud temperature. 86

5.13 Atomic cloud temperature against applied magnetic field. . . . 88
5.14 Atom trajectories and temperatures both with and without an atom launch. . . . 89
5.15 Example of a Raman spectrum showing two counter-propagating and one co-propagating peak. . . . 90
5.16 Microwave spectrum of all possible $|F = 1\rangle \rightarrow |F = 2\rangle$ transitions 92
5.17 All possible microwave transitions between F=1 and F=2. . . . 92
5.18 Atom number measurements before and after state selection stage 1. . . . 93
5.19 Microwave spectrum taken after state selection stages 1 and 2 94
5.20 Typical atom number measurement taken after state selection stages 1 and 2. . . . 95
5.21 Scan of the microwave pulse duration exibiting Rabi oscillations. 95
5.22 Fluorescence detection atom number data after state selection stages one, two and an $|F = 1, m_F = 0\rangle \rightarrow |F = 2, m_F = 0\rangle$ microwave transition, with and without an F=1 blowaway pulse. 96
5.23 Raman spectra with and without velocity selection. . . . 97
5.24 Fluorescence detection atom number data after a full state selection sequence. . . . 98
5.25 Sequence showing the population of each Zeeman sub-level at each stage of state selection. . . . 98
5.26 Slice from a CCD image of the Raman beam used to calculate beam collimation. . . . 99
5.27 Raman beam widths used to calculate divergence angle. 100
5.28 Optical setup used to measure Raman beam polarisation. . . . 101
5.29 Poincaré spheres showing Raman beam polarisation over time. 101
5.30 Raman beam polarisation over time. . . . 102
5.31 Rabi oscillations for varying atom cloud temperatures without any velocity selection. . . . 103
5.32 Rabi oscillations for varying durations of velocity selection pulses. . . . 104
5.33 Atom number versus velocity selection duration. 105
5.34 Power of the Raman beam during the full interferometry sequence 105
5.35 Interferometer fringe with a 2 ms T-time using a 77 µs velocity selection pulse. . . . 106
5.36 Interferometer contrast, and contrast over atom number versus velocity selection duration. . . . 106
5.37 Interferometer fringes before and after classical accelerometer correction. . . . 107

6.1 Photograph of the NavyPOD . . . 112
6.2 Images of experiment mounted inside of the NavyPOD during field trials. . . . 112
6.3 Atom cloud temperature measurements taken during the static field trial. . . . 113
6.4 Atom number stability measurement taken during the static field trial. . . . 114
6.5 Static field trial temperature stability . . . 114
6.6 Image of the XV Patrick Blackett and the route taken during the mobile field trials . . . 115
6.7 Photographs of the NavyPOD during transport to HMNB Portsmouth docks and loading onboard the XV Patrick Blackett naval research vessel. . . . 116
6.8 Power spectra of vibration data taken in the laboratory. . . . 117
6.9 Time-series and power spectra of acceleration data taken during the mobile field trials with both a stationary and moving ship. . . . 118
6.10 Time-series and power spectrum data taken with a 2 kHz bandwidth accelerometer along the ship travel direction during the second moving ship trial. . . . 119
6.11 Master and Apprentice laser lock noise power spectra both during the mobile field trials and in the laboratory. . . . 120
6.12 Power spectra for both Master and Apprentice optical output power taken during the mobile field trials and in the laboratory. 121
6.13 Magnetic field time-series and power spectrum data taken during the mobile field trials. . . . 121
6.14 Ballistic expansion images used to measure temperature with and without magnetic field compensation during the first Navy ship field trial. . . . 122
6.15 Temperature measurement taken with magnetic field compensation during first mobile field trial. . . . 123
6.16 Atom cloud position and width variation at a constant time after the molasses ramps with and without compensation taken during the first mobile field trial. . . . 124
6.17 Raman spectra taken during the first mobile field trial both with and without magnetic compensation engaged. . . . 125
6.18 Camera image of the scatter from the retro-reflected Raman beam after the mirror mount piezo had collapsed and image of the broken piezo. . . . 126

6.19 Camera image of the Raman beam at the atom position showing a large aberration and a photograph of the waveplate delamination which caused it. 127
6.20 Measured DOCP at several positions within the Raman beam. 127

Abstract

Atom interferometers have been used to measure accelerations and rotations in many laboratories around the world. They have demonstrated very high long-term stability, making them well suited for development into an inertial navigation system. The next stage of development towards a full navigation system is to move these laboratory demonstrators into the field, and improve their resilience to the effects of a more turbulent environment. This thesis presents the development of the first transportable quantum inertial sensor at the Centre for Cold Matter at Imperial College London, developing on the laboratory-based systems which have already been demonstrated. Rubidium-87 atoms are delivered into an ultra-high vacuum chamber with a 2D+ magneto optical trap (MOT), before being trapped in a 3D MOT and cooled to below 5 µK using polarisation gradient cooling. Atoms are efficiently prepared in a magnetically insensitive energy level, before a narrow velocity class of atoms is selected, to reduce the effect of thermal dephasing mechanisms. A three pulse, $\pi/2-\pi-\pi/2$, interferometer sequence coherently splits, reverses and recombines the atom cloud, and the atomic energy level populations are recorded after the third pulse using fluorescence imaging. Interference fringes have been demonstrated for a number of different interferometer times in the laboratory, and initial characterisation of the fringe contrast has been performed. In addition to in-laboratory characterisation, data from three field trials, alongside the Royal Navy, are presented. The trials have enabled us to benchmark the system's performance outside of the laboratory, and highlight the areas of development required for improved system performance in future field trials.

Preface

Note on Units

Throughout this thesis, most data will be presented in SI units, however there are a few situations where less common units will be used. When discussing magnetic fields, the unit of Gauss (G) will be used, which is equal to 10^{-4} T. For accelerations, acceleration due to gravity, g, will be used. While this varies depending on the global position, unless otherwise stated, the rounded value in London of $9.81\,\mathrm{m/s^2}$ will be used. Pressure will be presented in bar, where $1\,\mathrm{bar} = 10^5\,\mathrm{Pa}$ is roughly the Earth's atmospheric pressure. When referring to speeds and distances on a ship, velocities and distances will sometimes be referred to in knots, kn, or nautical miles, NM, but in each case these will also be converted to SI units in-text.

Note on Experimental Axes

Throughout this thesis, references to a standard coordinate system will be made. These axes are defined as in figure 1, where z is the measurement axis of the experiment, y points vertically upwards, and x points side to side of the vacuum chamber.

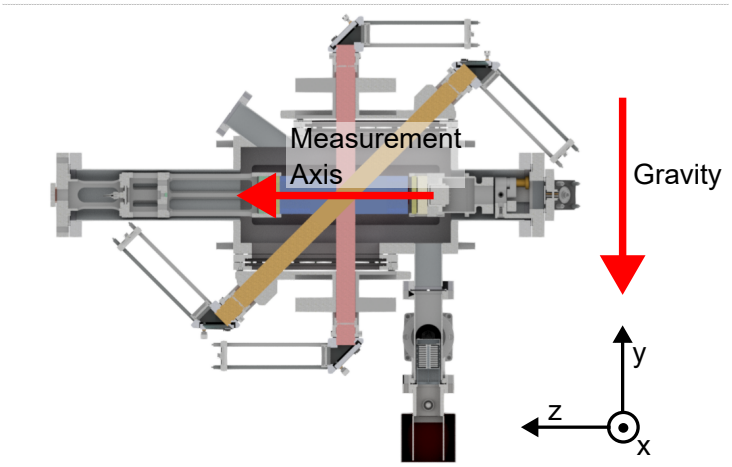


Figure 1: Experiment vacuum chamber with the definition of experimental axes used throughout this thesis. The z-axis is the measurement axis of the experiment, pointing from the in-vacuum mirror to the in-vacuum telescope. The y-axis points vertically upwards. The x-axis points across the vacuum chamber, from side to side.

Note on Detuning

Throughout this thesis, detuning from a given atomic transition will be described as negative for red-detuning, and positive for blue-detuning. For example light 5 MHz red-detuned from a transition would be described as −5 MHz detuned.

List of Useful Acronyms

AOM- Acousto-optic modulator
CAD- Computer aided design
CASC- Cold atom source cell
CCD- Charge coupled device
CCM- Centre for Cold Matter
COW- Neutron interferometry experiment performed by Colella, Overhauser and Werner
DDS-Direct digital synthesis
DLS- Differential light shift
DOCP- Degree of circular polarisation
DPSS laser- Diode pumped solid state laser
EOM- Electro-optic modulator
GNSS- Global navigation satellite system
GPS- Global positioning system
HMNB- His Majesty's naval base
MEMS- Microelectromechanical system
MOT- Magneto-optical trap
MPLB signal- Mixed phase lock beat signal
PBS- Polarising beamsplitter
PD- Photodiode
PFD- Phase frequency detector
PICAS- Photonically integrated cold atom source
PID controller- Proportional-integral-derivative controller
PIGA- Pendulous integrating gyroscopic accelerometer
PM optical fibre- Polarisation maintaining optical fibre
PODS- Persistent operational deployment systems
RF- Radio frequency
UHV- Ultra-high vacuum
VCL- Vapour cell lock
VCO- Voltage controlled oscillator

Chapter 1

Introduction

1.1 Navigation

Throughout history, humans have tackled the challenge of how to navigate their environment effectively. Explorers have used maps of the stars to define a reference frame, sextants to measure the angle between the sun and the horizon, and compasses to align themselves relative to the Earth's magnetic field [1]. Since the industrial revolution, global travel has become more widespread, and navigation techniques have become more advanced, requiring more sophisticated technology to deliver the required position accuracies. Today, Global Navigation Satellite Systems (GNSS), such as the US Global Positioning System (GPS), are ubiquitous in our everyday lives, facilitating the navigation of a vast number of vehicles and people around the world.

1.1.1 Global Navigation Satellite Systems (GNSS)

GNSS satellites transmit rf signals that can be detected by widely available receivers, such as mobile phones and in-car sat-navs. Figure 1.1 illustrates the operating principle of GNSS. The satellite signal contains information about its orbit, and the precise time determined by an onboard atomic clock. The receivers use signals from multiple satellites to determine their position on the surface of the Earth. GNSS is incredibly effective, delivering an accuracy of $\sim 30\,\text{cm}$ for civilian systems and $< 2\,\text{cm}$ for military systems, and can be used by anyone. However, GNSS does not provide a failsafe solution to positioning or timing. A study in 2017 by London Economics estimated the cost to the British economy of just a 5-day loss of GNSS coverage to exceed £5 billion. Subsequently, in 2018, the Blackett review of satellite-derived time and position stated all of the areas of the British economy which relied

on GNSS and highlighted the risks of losing access to these systems for even a short period [2]. The Blackett report made several suggestions about how to mitigate the risk of GNSS loss, with one major recommendation being research and investment into alternative, satellite-free positioning systems.

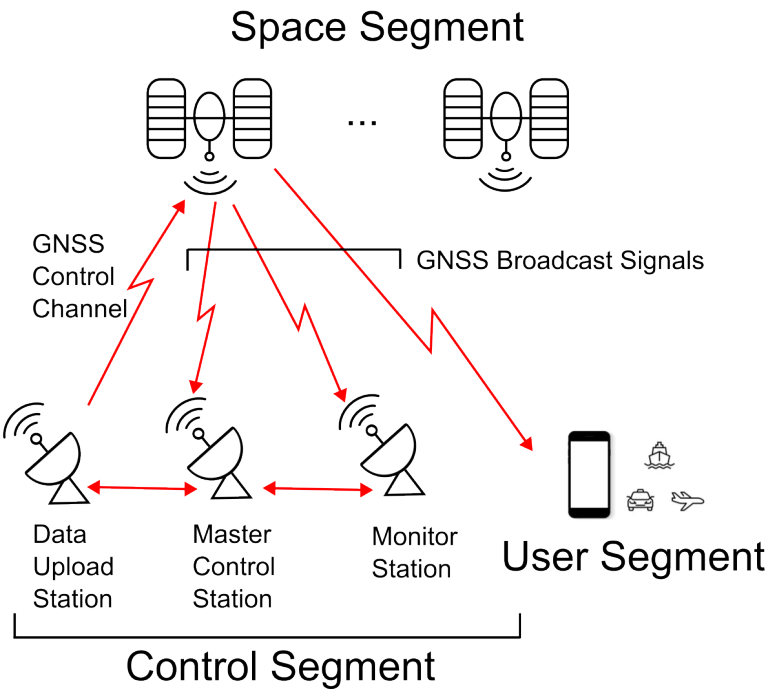
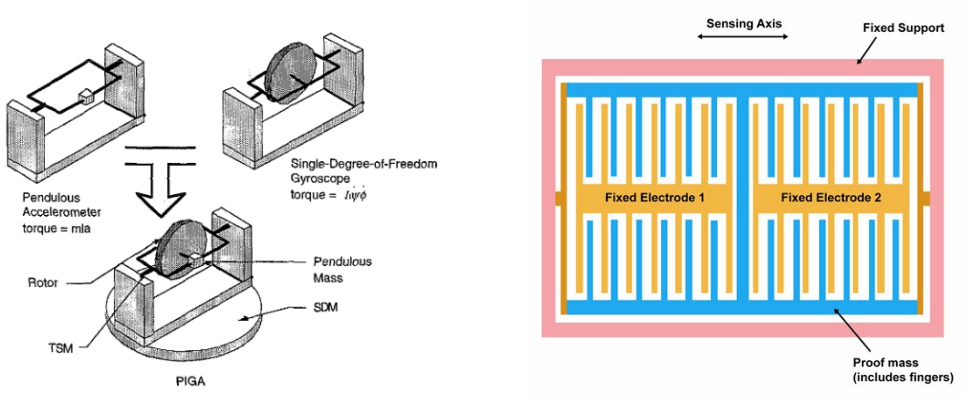


Figure 1.1: [3] The different stages of GNSS. The control segment involves ground stations used to monitor and correct the orbit and locations of satellites, which will be included in the information sent to receivers. The space segment includes satellites with onboard atomic clocks which send precisely time-stamped data packets to users. The user segment is any receiver, such as a mobile phone, which needs to calculate its position relative to the satellites.

1.1.2 Inertial Navigation

Inertial navigation is a technique which uses measurements of linear acceleration and rotation to track the position and orientation of a moving object, without the need for external points of reference. By integrating measurements from accelerometers and gyroscopes, inertial navigation systems calculate a vehicle's change in position and orientation in a given reference frame. The first inertial measurement units were the gyroscope, developed in 1852 by Léon Foucault [4], and the gyrocompass, invented in 1885 and refined in 1923 by Maximilian Schuler [5], with the former being used for measurement



(a) (b)

Figure 1.2: (a) The design of a PIGA, similar to that used in the German V2 rocket [7]. (b) Schematic of a MEMS accelerometer [8]. A moving mass (blue) is attached at either end to two flexible plates such that acceleration will change the distance between the moving (blue) and fixed (yellow) electrodes, changing the capacitance between them. The capacitance can then be measured and related to the system acceleration.

of the Earth's rotation, and the latter being used to determine an object's trajectory. However, the first use of a full inertial navigation system was during the second world war in the German V2 rocket [6]. Figure 1.2a shows a diagram of a Pendulous Integrating Gyroscopic Accelerometer (PIGA), similar to the ones used by the V2, which measures the deviation of a pendulous mass attached to a spinning gyroscope.

Modern quartz oscillator accelerometers measure the mechanical stress on a quartz crystal induced by the deviation of an attached pendulous mass to measure the system acceleration [9]. Another commonly used inertial sensor is the microelectromechanical system (MEMS). Figure 1.2b shows a schematic of a MEMS device, which uses the deviation of a mass supported by flexible bars or springs to cause a change in capacitance which can then be measured and used to calculate acceleration. Modern MEMS devices commonly achieve acceleration sensitivities of $\sim 1\mu g/\sqrt{Hz}$, and high precision devices can achieve $< 1ng/\sqrt{Hz}$ [10]. Despite the extremely high precision that MEMS sensors can achieve, they suffer from inherent bias and scale factor drift over time, which limits their long-term navigation capabilities. Even the most sophisticated, modern navigation systems will have a position error of around 1 NM (1.852 km) after a few days without correction [11], and with increasingly demanding navigation requirements, new navigation systems with lower drift need to be developed.

1.2 Interferometry

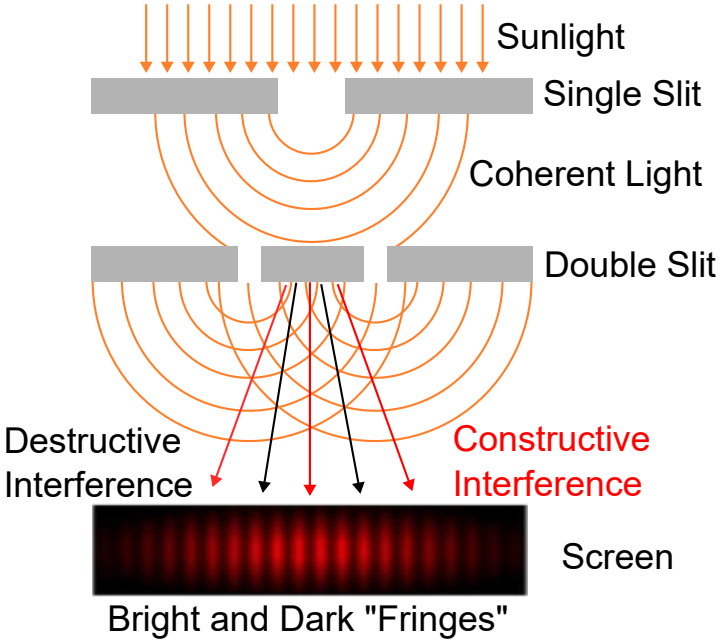


Figure 1.3: The setup of Young's double slit experiment using sunlight. A single slit is used to create coherent light which creates two wave fronts when passed through a double slit. The two wave patterns interfere to give a pattern of bright and dark fringes on a screen.

The first observation of optical interference was made by Young in 1801 using sunlight [12]. Figure 1.3 shows a diagram of Young's setup. A single slit in a metal plate was used to create a quasi-coherent beam of sunlight, which diffracted when passed through two closely spaced slits in a second plate downstream. Periodic dark and light and regions were observed in the far-field after the double slit. Young coined the term "interference fringes" to describe the pattern he had observed. Later in the 19^{th} century, experiments by Michelson [13], and Zehnder[14], extended Young's work, using mirrors and beam splitters to control the distances travelled by the two interfering waves. Figure 1.4 shows a diagram of an optical Mach-Zehnder interferometer. Through careful measurements of the interference pattern observed, the relative path lengths of each interferometer arm could be determined with high precision. This enabled measurements of physical properties, such as the pressure of a gas cell in one of the interferometer arms, to be made.

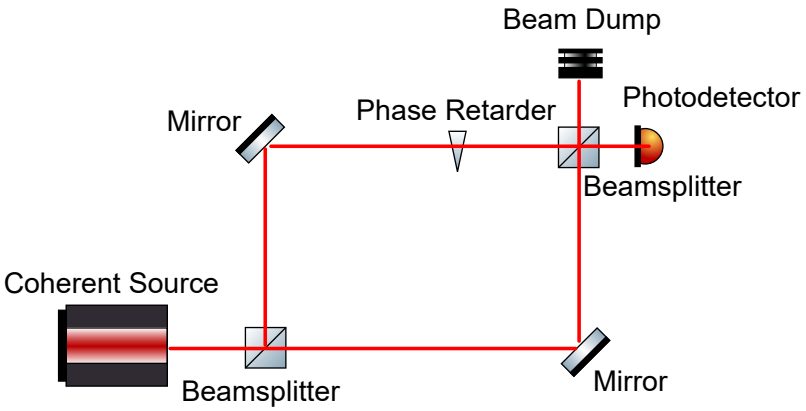


Figure 1.4: An optical Mach-Zehnder interferometer. Light beams are split by a beamsplitter, reflected by mirrors and recombined at a second beamsplitter. A photodetector at one of the output ports measures the interference fringes which are dependent on the phase difference between the two arms of the interferometer.

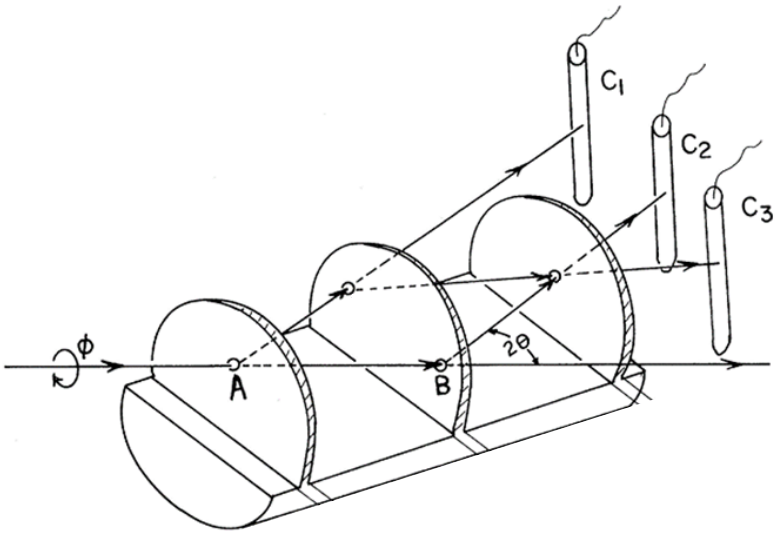


Figure 1.5: (Edited from [15]) The setup of the neutron interferometer as used in the COW experiment. A neutron beam was coherently split, reflected and then recombined before the number of neutrons at each output port was detected, using two Helium detectors (C_2 and C_3). By rotating the entire system about the axis AB, a relationship between the interferometer phase, or the neutron population at each detector, and the angle of the experiment to the direction of gravity was established.

1.2.1 Matter-Wave Interferometry

Atoms of a given isotope have physical properties which are constant in time and space, as well as having a very well defined mass. This makes them ideal candidates for use as stable inertial observers. As such, quantum enhanced sensors offer a potential route towards low-drift accelerometers and gyroscopes for future long-range inertial navigation systems.

The diffraction of matter waves was first observed in 1930 by Estermann and Stern using a sodium beam and a sodium chloride surface [17]. Since then, a number of matter wave diffraction and interferometry techniques have been developed using cold neutrons [18], atoms [19, 20, 16] and even large complex molecules [21]. In 1976 Colella, Overhauser, and Werner demonstrated the first inertial measurement using a matter-wave interferometer [15]. Figure 1.5 shows a schematic of the "COW experiment". A cold beam of neutrons passing through three silicon lattices in a Talbot-Lau configuration created an interference pattern in the neutron number density with a phase which was shifted by the local gravitational field. The COW experiment was limited by a "sagging" of the interferometer arms for large rotation angles, but was still able to measure the local gravitational acceleration to within 0.1 g [22].

In 1991, Kasevich and Chu demonstrated an inertially sensitive sodium interferometer [16] using stimulated Raman transitions. Figure 1.6 illustrates the Kasevich-Chu experiment. Sodium atoms were cooled to around 30 µK, at which point their wave-like properties dominated their dynamics. Pulses

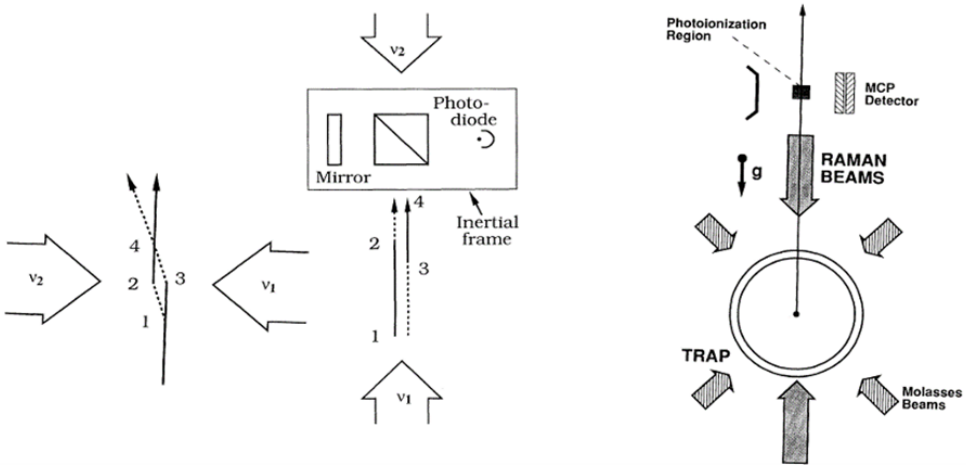


Figure 1.6: [16] Experimental setup of the atom interferometer based on stimulated Raman transitions in sodium used by Kasevich and Chu.

of light were then used to drive stimulated Raman transitions to split, reflect and recombine the matter-waves. The phase difference between the two paths of the interferometer was dependent on both the time between each light pulse and the local gravitational field. By measuring this phase difference, this experiment was able to measure the local gravity with a precision of 3×10^{-6} g, an improvement of around 10^5 compared to the COW neutron interferometer [16].

Atom interferometers similar to that used by Kasevich and Chu have since been demonstrated using rubidium [23], caesium [24], and strontium [25], with applications in measurements of fundamental constants [26, 27], tests of fundamental physics [28, 29], precision measurements of magnetic fields [30], geodesy [31, 32] and inertial sensing [33, 34, 35]. As well as stimulated Raman interactions [36, 37], modern interferometry experiments have been demonstrated using Bragg diffraction to coherently manipulate atom clouds [38, 39]. There are also proposals to perform multiple Bragg or Raman transitions to use Bloch Oscillations in an optical lattice to create large momentum transfer atom interferometers [40, 41]. The high precision and inherent resilience to systematic errors that can be achieved with atom interferometry make it ideally suited to inertial sensing for long-range inertial navigation.

1.3 Thesis Outline

The Centre for Cold Matter at Imperial College London has developed a number of laboratory based atom interferometers, and have used them to measure accelerations [42, 43] and rotations [44] for inertial navigation. The next step towards a full inertial navigation system is to ruggedise these sensors and test them in the field.

During my PhD I have built and tested the first transportable inertial sensor demonstrator at Imperial College London, and have begun characterisation of its performance outside of the laboratory. In chapter 2, I will introduce the theory describing an atom interferometer, starting from the light-atom interaction and building up to show the acceleration sensitivity of such a system. Chapter 3 describes the processes used to trap and cool an atom cloud, before preparing the atoms in a magnetically insensitive energy level. Chapter 4 describes the experimental apparatus of my transportable demonstrator. This includes the design process for critical experimental sub-components, as well as details of construction and optimisation of each part of the experiment. In-laboratory experimental results showing the characterisation

of the experiment are presented in chapter 5, and chapter 6 describes the field trials undertaken with the Royal Navy, as well as proposals for future improvements to enhance future trials.

Chapter 2

Atom Interferometry

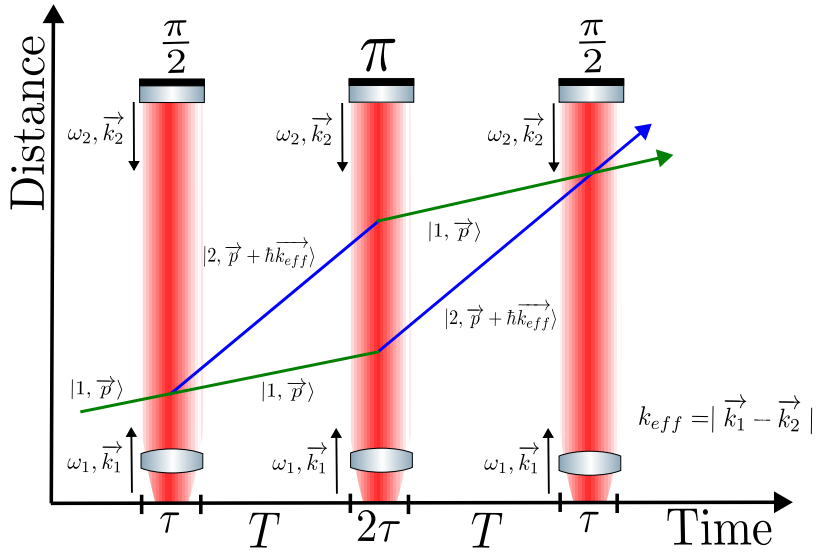


Figure 2.1: An atom interferometry sequence in the absence of acceleration. Each pulse of light acts like a beamsplitter or a mirror, as in the optical case. By measuring the atomic energy level populations after the third interferometer pulse, the phase difference between the two arms is determined.

Figure 2.1 shows a time-space diagram of the atom interferometer used in this experiment, with no system acceleration. This chapter will provide a theoretical description of how two-photon stimulated Raman pulses can be used to coherently manipulate atoms, before extending to a description of a full acceleration-sensitive interferometer. I will then describe the Raman beam, and how it can be used to provide the light needed to drive interferometry pulses.

2.1 Note on Atomic Transition Labels

Throughout this thesis, I will use the following convention relating to σ^+ and σ^- transitions [45].

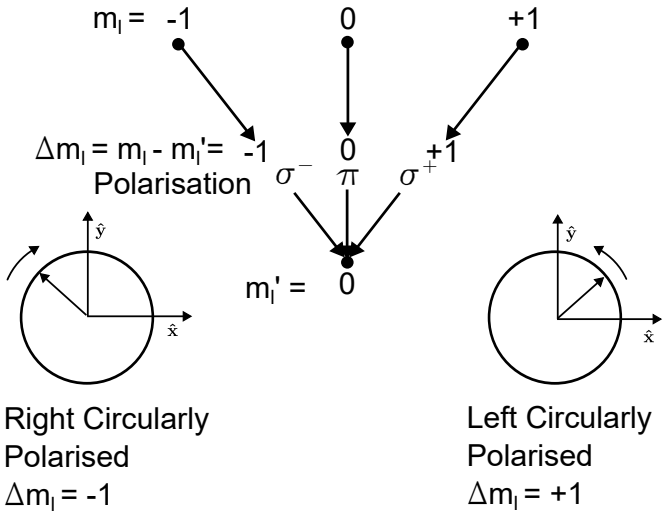


Figure 2.2: Selection rules for magnetic quantum number m_l and emitted light polarisation observed from the positive z direction for σ^+ and σ^- transitions. (Based on [45])

Light emitted through an electric dipole transition for which $\Delta m_l = +1$ is left circularly polarised, with respect to the positive z axis and the transition will be referred to as σ^+. Equivalently, $\Delta m_l = -1$ transitions associated with the emission of right circularly polarised light are labelled σ^-. The selection rules for these transitions can be seen in figure 2.2.

2.2 Stimulated Raman Interactions

Stimulated Raman transitions involve the simultaneous absorption of a photon from one light field, and stimulated emission of a photon into a second light field. As atoms absorb from one light field, and emit into the other, this process is also associated with a transfer of momentum.

Figure 2.3a shows an energy level diagram for a three level atom interacting with two optical fields, L1 and L2, of angular frequency ω_{L1} and ω_{L2}. The three atomic levels are labelled $|1\rangle$, $|2\rangle$, and $|3\rangle$, in order of increasing angular frequency. The angular frequency difference between $|1\rangle$ and $|2\rangle$ is ω_0. The light fields L1 and L2 couple $|1\rangle$ and $|2\rangle$ respectively to a virtual energy

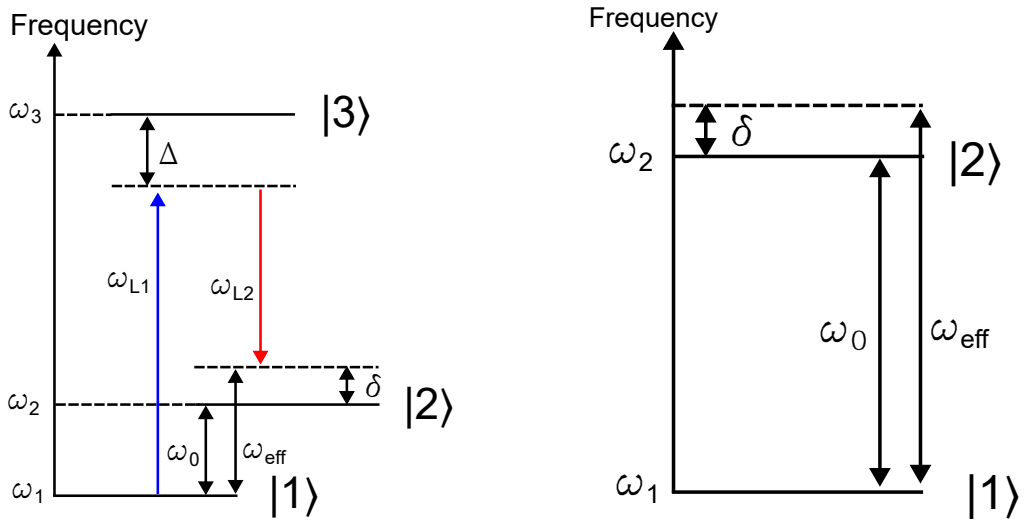


Figure 2.3: (a) Energy level diagram showing the full, three-level system during a two photon stimulated Raman transition. The blue and red lines show transitions due to the two different light fields L1 and L2. The single photon detuning from the intermediate state is Δ and the two photon detuning from $|2\rangle$ is δ (b) The simplified, two-level atomic system during a stimulated Raman transition after eliminating the intermediate state.

level which is red detuned from $|3\rangle$ by Δ. Assuming an atom is initially in state $|1\rangle$, it can "virtually" absorb a photon from L1, and simultaneously emit a photon into L2, making a transition from $|1\rangle$ to $|2\rangle$ via the virtual intermediate state. The two photon detuning of the light fields from $|2\rangle$ is labelled δ. Consider the two oscillating electric fields of L1 and L2, with the form

$$\begin{aligned} \mathbf{E}_{\mathrm{L1}} &= \mathbf{E}_{\mathrm{L10}} \cos\left(\omega_{\mathrm{L1}} t + \phi_{\mathrm{L1}}\right) \\ \mathbf{E}_{\mathrm{L2}} &= \mathbf{E}_{\mathrm{L20}} \cos\left(\omega_{\mathrm{L2}} t + \phi_{\mathrm{L2}}\right) \end{aligned} \tag{2.1}$$

where $\mathbf{E}_{\mathrm{Li0}}$ is the electric field amplitude of beam i, t is time, and ϕ_{Li} is the light phase of beam i at $t = 0$. The coupling of each state $|1\rangle$ and $|2\rangle$ to the intermediate state, $|3\rangle$, is characterised by a Rabi frequency Ω_{i3}, where i is the initial state. L1 and L2 are far enough detuned from the $|F = 1\rangle \rightarrow |F = 2\rangle$ transition that Ω_{12} can be ignored. In the case where $\Delta \gg \Omega_{\mathrm{i3}}$ and $\Delta \gg \delta$, the intermediate state can be removed from the equations of motion of the system, which can be treated as an effective two-level system, with an effective Rabi frequency [42]

$$\Omega_{\mathrm{eff}} = \frac{\Omega_{13}\Omega_{23}^{*}}{2\Delta}, \tag{2.2}$$

an effective frequency $\omega_{\text{eff}} = \omega_{\text{L1}} - \omega_{\text{L2}}$, and an effective phase $\phi_{\text{eff}} = \phi_{\text{L1}} - \phi_{\text{L2}}$. Since the system can be treated as a two-level system, with a single photon transition, a "Raman beam" will often be referred to during this thesis. This is an effective laser beam with frequency $\omega_{\text{eff}} = \omega_{\text{L1}} - \omega_{\text{L2}}$ which drives the stimulated Raman transition. This is for ease of explanation and when referring to the Raman beam it is implied that a two-photon stimulated Raman transition is being driven.

2.3 Atom-Light Interaction

Since the intermediate atomic state can be ignored, consider electromagnetic radiation with an oscillating electric field of the form

$$\mathbf{E} = \mathbf{E}_0 \cos(\omega t + \phi), \tag{2.3}$$

where the eff subscript has been dropped for readability. Now consider the two level atomic system shown in figure 2.3b, with energies $\hbar\omega_1$ and $\hbar\omega_2$, where the frequency difference $\omega_0 = \omega_2 - \omega_1$. The atomic Hamiltonian acts on vectors describing the ground and excited states $|1\rangle$ and $|2\rangle$ such that

$$\begin{aligned} \hat{H}_{\text{A}} |2\rangle &= E_2 |2\rangle \\ \hat{H}_{\text{A}} |1\rangle &= E_2 |1\rangle , \end{aligned} \tag{2.4}$$

where $|1\rangle = [0\ 1]^{\text{T}}$ and $|2\rangle = [1\ 0]^{\text{T}}$, and $E_{\text{i}} = \hbar\omega_{\text{i}}$. The total Hamiltonian, $\hat{H}$, acting on the atomic state, $|\psi\rangle$ can be written as

$$\begin{aligned} \hat{H} |\psi\rangle &= \left(\hat{H}_{\text{A}} + \hat{H}_{\text{I}}\right) |\psi\rangle \\ &= a_1(t)\hbar\omega_1 |1\rangle + a_2(t)\hbar\omega_2 |2\rangle + \hat{H}_I |\psi\rangle \\ &= \hbar c_1(t) e^{-i\omega_1 t}\omega_1 |1\rangle + \hbar c_2(t) e^{-i(\omega_2+\delta)t}\omega_2 |2\rangle + \hat{H}_{\text{I}} |\psi\rangle , \end{aligned} \tag{2.5}$$

where $\hat{H}_{\text{I}}$ is the interaction Hamiltonian, a_1 and a_2 are probability amplitudes of an atom being in each state at time t, $\delta = \omega - \omega_0$ is the detuning of the incident light from the transition frequency, and where a transformation of $a_1(t) = c_1(t)e^{-i(\omega_1 t)}$, $a_2(t) = c_2(t)e^{-i(\omega_2+\delta)t}$ is made to the probability amplitudes to remove time dependance from the Hamiltonian. Differentiating the atomic state $|\psi\rangle$ with respect to time gives

$$\begin{aligned} i\hbar\frac{d|\psi\rangle}{dt} = {} & i\hbar\frac{dc_1(t)}{dt}e^{-i\omega_1 t}|1\rangle + i\hbar\frac{dc_2(t)}{dt}e^{-i(\omega_2+\delta)t}|2\rangle \\ & + \hbar c_1(t)e^{-i\omega_1 t}\omega_1 |1\rangle + \hbar c_2(t)e^{-i(\omega_2+\delta)t}(\omega_2+\delta)|2\rangle . \end{aligned} \tag{2.6}$$

Substituting equations (2.5) and (2.6) into the time-dependent Schrödinger equation gives

$$\hat{H}_{\mathrm{I}} |\psi\rangle = i\hbar \left(\frac{dc_1}{dt} e^{-i\omega_1 t} |1\rangle + \frac{dc_2}{dt} e^{-i(\omega_2+\delta)t} |2\rangle - ic_2\delta e^{-i(\omega_2+\delta)t} |2\rangle \right), \quad (2.7)$$

where the time dependencies of c_1 and c_2 have been removed for readability. Applying the mapping $\langle 2|$, the left hand side of equation (2.7) is

$$c_1 e^{-i\omega_1 t} \langle 2| \hat{H}_{\mathrm{I}} |1\rangle + c_2 e^{-i(\omega_2+\delta)t} \cancelto{0}{\langle 2| \hat{H}_{\mathrm{I}} |2\rangle}, \quad (2.8)$$

where the second term is cancelled as it is an odd function integrated over all space. The right hand side becomes

$$i\hbar \left(\frac{dc_1}{dt} e^{-i(\omega_1 t)} \cancelto{0}{\langle 2|1\rangle} + \left(\frac{dc_2}{dt} e^{-i(\omega_2+\delta)t} - ic_2\delta e^{-i(\omega_2+\delta)t} \right) \cancelto{1}{\langle 2|2\rangle} \right). \quad (2.9)$$

Combining the left and right hand sides gives

$$c_1 e^{-i\omega_1 t} \langle 2| \hat{H}_{\mathrm{I}} |1\rangle = i\hbar \left(\frac{dc_2}{dt} e^{-i(\omega_2+\delta)t} - ic_2\delta e^{-i(\omega_2+\delta)t} \right). \quad (2.10)$$

Defining $\mathbf{d}_{21} = \langle 2| \hat{\mathbf{D}} |1\rangle$, where $\hat{\mathbf{D}}$ is the dipole operator, $\langle 2| \hat{H}_{\mathrm{I}} |1\rangle$ can be evaluated:

$$\begin{aligned} \langle 2| \hat{H}_{\mathrm{I}} |1\rangle &= -e\mathbf{E}_0 \cdot \mathbf{d}_{21} \cos(\omega t + \phi) \\ &= -e\mathbf{E}_0 \cdot \mathbf{d}_{12}^* \cos(\omega t + \phi) \\ &= \hbar\Omega^* \cos(\omega t + \phi), \end{aligned} \quad (2.11)$$

where $\Omega = -e\mathbf{E}_0 \cdot \mathbf{d}_{12}/\hbar$ is the Rabi frequency of the $|1\rangle \to |2\rangle$ transition. Then substituting back into equation (2.10), the dynamic equation for c_2 becomes

$$\begin{aligned} c_1 \hbar\Omega^* \cos(\omega t + \phi) e^{-i(\omega_1 t)} &= i\hbar \left(e^{-i(\omega_2+\delta)t} \frac{dc_2}{dt} - ic_2\delta e^{-i(\omega_2+\delta)t} \right) \\ \implies i\frac{dc_2(t)}{dt} &= \Omega^* \cos(\omega t + \phi) e^{i(\omega_0+\delta)t} c_1(t) - \delta c_2(t), \end{aligned} \quad (2.12)$$

and similar analysis for c_1 gives

$$i\frac{dc_1(t)}{dt} = \Omega\cos(\omega t+\phi)e^{-i(\omega_0+\delta)t}c_2(t), \tag{2.13}$$

where the time dependencies have been re-included. Applying the rotating wave approximation, defining $\Omega' = \Omega e^{i\phi}$, and noting that $\omega - \omega_0 - \delta = 0$, the dynamic equations for c_1 and c_2 can be written as

$$\begin{aligned} i\frac{dc_1(t)}{dt} &= \frac{\Omega}{2}e^{i(\omega-\omega_0-\delta)t}c_2(t) \\ i\frac{dc_2(t)}{dt} &= \frac{\Omega^*}{2}e^{-i(\omega-\omega_0-\delta)t}c_1(t) - \delta c_2(t) \\ \implies i\frac{dc_1(t)}{dt} &= \frac{\Omega'}{2}c_2(t) \\ \implies i\frac{dc_2(t)}{dt} &= \frac{\Omega'^*}{2}c_1(t) - \delta c_2(t), \end{aligned} \tag{2.14}$$

which can be written in matrix form as

$$i\begin{pmatrix}\dot{c_1}\\ \dot{c_2}\end{pmatrix} = \begin{pmatrix}0 & \frac{\Omega'}{2}\\ \frac{\Omega'^*}{2} & -\delta\end{pmatrix}\begin{pmatrix}c_1\\ c_2\end{pmatrix}. \tag{2.15}$$

Solving these equations and defining $\Omega\Omega^* = \Omega^2$ and $\sqrt{\delta^2+\Omega^2} = \Omega_{\mathrm{G}}$, where Ω_{G} is the "generalised Rabi frequency", the matrix for the time evolution of c_1 and c_2 is

$$\begin{pmatrix}c_1(t)\\ c_2(t)\end{pmatrix} = U_c\cdot\begin{pmatrix}c_1(t_0)\\ c_2(t_0)\end{pmatrix}, \tag{2.16}$$

where U_{c} is the propagation matrix for the probability amplitudes c_1 and c_2 given by

$$U_c(t_0,\tau) = \begin{pmatrix}\cos\left(\frac{\Omega_{\mathrm{G}}\tau}{2}\right) - i\frac{\delta}{\Omega_{\mathrm{G}}}\sin\left(\frac{\Omega_{\mathrm{G}}\tau}{2}\right) & -i\frac{\Omega}{\Omega_{\mathrm{G}}}e^{i\phi(t)}\sin\left(\frac{\Omega_{\mathrm{G}}\tau}{2}\right)\\ -i\frac{\Omega^*}{\Omega_{\mathrm{G}}}e^{-i\phi(t)}\sin\left(\frac{\Omega_{\mathrm{G}}\tau}{2}\right) & \cos\left(\frac{\Omega_{\mathrm{G}}\tau}{2}\right) + i\frac{\delta}{\Omega_{\mathrm{G}}}\sin\left(\frac{\Omega_{\mathrm{G}}\tau}{2}\right)\end{pmatrix}, \tag{2.17}$$

where a global phase factor has been ignored. The terms $e^{\pm i\phi(t)}$ include an extra phase due to the light pulse occurring at a time $t \neq 0$ so that $\phi(t\neq 0) = \phi(t=0) + \omega t_0$. Here, t_0 is defined as the start time of the light pulse, and τ is the duration of the light pulse.

To include the Doppler shift into this propagator, the incident light frequency simply changes by a factor δ_{D} so that $\omega \to \omega + \delta_{\mathrm{D}}$. If all atoms are initially in $|1\rangle$, then the probability of finding an atom in $|2\rangle$ after a Raman pulse of duration τ is

$$\begin{aligned} P_2(\tau) &= |\langle 2| U_c(\tau) |\psi(t)\rangle|^2 \\ &= \frac{\Omega^2}{\Omega_{\mathrm{G}}^2} \sin^2\left(\frac{\Omega_{\mathrm{G}}\tau}{2}\right). \end{aligned} \tag{2.18}$$

To start to extend this towards a full interferometry sequence, a free propagation matrix is defined as

$$U_f(T) = \begin{pmatrix} e^{\frac{i\omega_0 T}{2}} & 0 \\ 0 & e^{\frac{-i\omega_0 T}{2}} \end{pmatrix}, \tag{2.19}$$

where T is the duration of free propagation, and where the zero of energy has been set half way between the excited and ground states of the system.

2.3.1 π and $\pi/2$ Pulses-

For a single pulse of light with duration τ incident on an atom initially in $|1\rangle$, with no detuning, the atomic state can be represented as

$$|\psi\rangle_{\mathrm{single}} = \begin{pmatrix} \sin^2\left(\frac{\Omega\tau}{2}\right) \\ \\ \cos^2\left(\frac{\Omega\tau}{2}\right) \end{pmatrix}. \tag{2.20}$$

If the duration of the pulse is tuned such that $\Omega\tau = \frac{\pi}{2}$, the probability of the atom being in each of the two atomic states is 0.5. This is known as a "$\pi/2$-pulse". If instead the pulse is tuned such that $\Omega\tau = \pi$, the probability of the atom being transferred to $|2\rangle$ is 1, this known as a "π-pulse". In each case, if the atom absorbs a photon and is excited into $|2\rangle$, it will receive a momentum kick of $\hbar k_{\mathrm{eff}}$, where k_{eff} is the effective k vector of the two photon transition. This means that the $\pi/2$-pulse creates a superposition of momentum states. It also means that a π-pulse will act to reduce the momentum of an atom which was previously excited, and increase the momentum of an atom which was not previously excited. These pulses can be interpretted in the same way as beamsplitters ($\pi/2$) and mirrors (π) in the optical Mach-Zehnder interferometer.

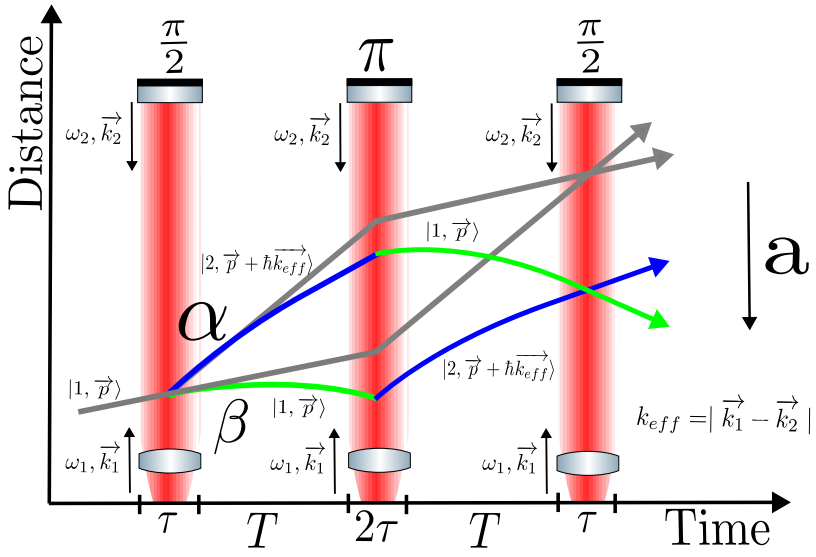


Figure 2.4: Time-space diagram showing the trajectories of the two arms of a three pulse atom interferometer without acceleration (grey) and with acceleration (blue and green). The path α corresponds to the interferometer arm where atoms are excited to $|2\rangle$ during the first $\pi/2$-pulse and β corresponds to the arm where atoms remain in $|1\rangle$.

2.3.2 Three Pulse Interferometer

By combining $\pi/2$ and π-pulses to coherently split, reverse, and recombine atoms, a Mach-Zehnder-type interferometer can be created, as shown in figure 2.4. Atoms are initially in state $|1, p\rangle$ where p is a momentum state. After a $\pi/2$-pulse, the atoms are coherently split into a superposition of energy and momentum states, being in either $|1, p\rangle$ or $|2, p + \hbar k_{\text{eff}}\rangle$. The atoms then freely propagate for a time, T, which is the interferometer "T-time", before a π-pulse switches the momenta of the atomic wavepackets. This means atoms which were previously in $|1, p\rangle$ are now in $|2, p + \hbar k_{\text{eff}}\rangle$ and vice-versa. After a second T-time, the two arms of the interferometer will spatially overlap again, so a second $\pi/2$-pulse is used to recombine them and allow the atomic states to be measured.

To simulate the effect of the interferometer, the propagators for the light atom interaction, in equation (2.17), and for free propagation, in equation (2.19), can be combined to give the atomic state after all three pulses

$$|\Psi\rangle = U_{\pi/2}(3\tau + 2T, \tau) \cdot U_f(T) \cdot U_\pi(\tau + T, 2\tau) \cdot U_f(T) \cdot U_{\pi/2}(0, \tau) \, |\Psi_0\rangle \,, \quad (2.21)$$

where $|\Psi_0\rangle$ is the atomic state before the interferometer, and $U_{\pi/2}$ and U_π are

the propagators for a $\pi/2$ and π-pulse respectively. For an atom starting in $|1\rangle$, P_2 is the probability of detecting the atom in $|2\rangle$ after the interferometer

$$P_2 = |\langle 2|\Psi\rangle|^2 = \sin^2\left(\frac{\Delta\Phi}{2}\right) = \frac{1}{2}(1-\cos(\Delta\Phi)), \tag{2.22}$$

where $\Delta\Phi$ is the overall phase difference between the two interferometer arms.

2.3.2.1 Interferometer Phases

The total interferometer phase

$$\Delta\Phi = \Delta\phi_{\text{int}} + \Delta\phi_{\text{prop}}, \tag{2.23}$$

comprises of two sources of phase which can be picked up by the atoms, ϕ_{int}, due to the interaction of the atomic cloud with the Raman beam, and ϕ_{prop}, due to the phase picked up during the propagation of the atomic cloud during the interferometer. There is also a contribution due to shifts in the internal state from second order magnetic field shifts and AC Stark shifts. However, by stabilising the magnetic field and cancelling the AC Stark shift, these can be neglected. The methods for accounting for these shifts are described in detail later in this thesis. The propagation phase is determined by comparing the classical action

$$S = \int_{\text{path}} L(x(t), \dot{x}(t))dt, \tag{2.24}$$

along each arm of the interferometer. Here, L is the Lagrangian for the atom at position x and time t. For uniform acceleration, this turns out to equal zero [43, 46]. This means that the entirety of the interferometer phase is determined by the interaction with the Raman beam. In the simplified case where $\delta = 0$, equation (2.17) becomes

$$U_c(\delta=0) = \begin{pmatrix} \cos\left(\frac{\Omega_{\text{eff}}\tau}{2}\right) & -ie^{i\phi_{\text{eff}}}\sin\left(\frac{\Omega_{\text{eff}}\tau}{2}\right) \\ -ie^{-i\phi_{\text{eff}}}\sin\left(\frac{\Omega_{\text{eff}}\tau}{2}\right) & \cos\left(\frac{\Omega_{\text{eff}}\tau}{2}\right) \end{pmatrix}, \tag{2.25}$$

where the eff subscript has been re-included for completeness. It can be seen that upon a transition from $|1\rangle \to |2\rangle$, or $|2\rangle \to |1\rangle$, the atoms pick up phases of $e^{i\phi_{\text{eff}}}$ and $e^{-i\phi_{\text{eff}}}$ respectively. By separating the interferometer into arms α and β, as in figure 2.4, the total phase accumulated can be summed to give

$$\Delta\Phi = \left(\phi^{(1)}_{\text{eff}} - \phi^{(2)}_{\text{eff},\alpha}\right) - \left(\phi^{(2)}_{\text{eff},\beta} - \phi^{(3)}_{\text{eff}}\right), \tag{2.26}$$

where superscript (i) refers to interferometer pulse i.

2.3.2.2 Acceleration Sensitivity

Figure 2.4 shows how, when the atoms are subject to a uniform acceleration, a, the interferometer arm trajectories become asymmetric. Since the only phase picked up by the atoms during the interferometer is due to the Raman laser phase, the phase accumulated during each pulse, i, can be expressed as the local laser phase at time t_i and position $x\left(t_\mathrm{i}\right)$

$$\phi_\mathrm{i} = k_\mathrm{eff} x\left(t_\mathrm{i}\right) + \omega_\mathrm{eff} t_\mathrm{i} + \phi_\mathrm{i0}, \tag{2.27}$$

where ϕ_i0 is a "laser offset phase", which is well controlled in the laboratory. The positions of the atoms at each interferometer pulse are

$$\begin{aligned} x(t_1) &= x_0 \\ x_\alpha(t_2) &= x_0 + (v_0 + v_\mathrm{rec})T - a\frac{T^2}{2} \\ x_\beta(t_2) &= x_0 + v_0 T - a\frac{T^2}{2} \\ x(t_3) &= x_0 + (2v_0 + v_\mathrm{rec})T - 2aT^2 \end{aligned} \tag{2.28}$$

where $v_\mathrm{rec} = \hbar k_\mathrm{eff}/m$ is the recoil velocity imparted during a Raman transition, v_0 is the initial atom velocity, and T is the interferometer T-time. Substituting equations (2.27) and (2.28) into equation (2.26) gives

$$\Delta\Phi = k_\mathrm{eff} a T^2 + (\phi_{10} - 2\phi_{20} + \phi_{30}), \tag{2.29}$$

which shows that the interferometer phase is determined by the acceleration, a, the interferometer T-time, the effective wavenumber, k_eff, and the laser offset phase during each pulse. If there is also atomic motion perpendicular to the Raman beam propagation direction, then the atom interferometer will enclose a physical area. This physical area is sensitive to the rotation of the experiment, and will add an additional phase, known as the Sagnac phase [47]. This phase can be used to create a gyroscope, which has been studied in a previous thesis at Imperial College [44]. However, this effect will not be studied as part of this thesis.

2.3.3 Interferometer Contrast

Equation (2.22) describes the interference pattern for a single atom. The probability of the atom being observed in the excited energy level, $|2\rangle$, as the interferometer phase is varied, has a cosine shape, with an amplitude of one. When extending to an ensemble of atoms, the detected interference

fringe is a combination of the interference patterns due to each single atom. Any phase differences in each interference pattern will reduce the amplitude, or "contrast", of the overall interference fringe. Mechanisms which cause reduction in the fringe amplitude are referred to as "dephasing mechanisms". When averaging over a large number of atoms, equation (2.22) becomes

$$P_2 = \frac{1}{2}(1 - C\cos(\Delta\Phi)), \tag{2.30}$$

where C is the interferometer contrast. If a measurement of P_2 is made, with an associated error σ_{P_2}, the interferometer phase error, $\sigma_{\Delta\Phi}$, is given by

$$\sigma_{\Delta\Phi} = \frac{\sigma_{P_2}}{\frac{dP_2}{d\Delta\Phi}} = \frac{2\sigma_{P_2}}{C\sin(\Delta\Phi)}. \tag{2.31}$$

This means that, to minimise the interferometer error, and therefore the acceleration error, the system contrast needs to be maximised, and the interferometer phase should be close to $\pi/2$.

2.4 Raman Transition Implementation

So far, all discussion of interferometry and stimulated Raman transitions has been general and could be used for any similar atomic system. For the experiment described in this thesis, the ^{87}Rb D_2 line is used throughout, making states $|1\rangle$ and $|2\rangle$ the $|F = 1\rangle$ and $|F = 2\rangle$ hyperfine levels of the $5^2S_{1/2}$ energy level. The intermediate $|3\rangle$ state will have contributions from multiple different possible states, which will be shown in section 2.4.1. From this point on, the angular frequency difference between these two states will often be referred to as ω_{hf}, which is equal to $2\pi\nu_{\text{hf}}$, where $\nu_{\text{hf}} \approx 6.834\,682\,\text{GHz}$ is the frequency difference between the $|F = 1\rangle$ and $|F = 2\rangle$ hyperfine levels.

2.4.1 Polarisation Requirement

When running the interferometer, to reduce the impact of magnetic fields to a second order effect, the magnetically insensitive $|F = 1, m_F = 0\rangle \rightarrow |F = 2, m_F = 0\rangle$ transition is driven. Further discussion of how this is achieved is seen in chapter 3. By carefully selecting an appropriate polarisation for each beam, called the Master and Apprentice beams due to the names of the lasers they are emitted from, it can be ensured that atoms are only driven in the $\Delta m_F = 0$ transition. From the definition of the Rabi frequency given in equation (2.11), the Rabi frequency for each photon interaction with an atom is given by

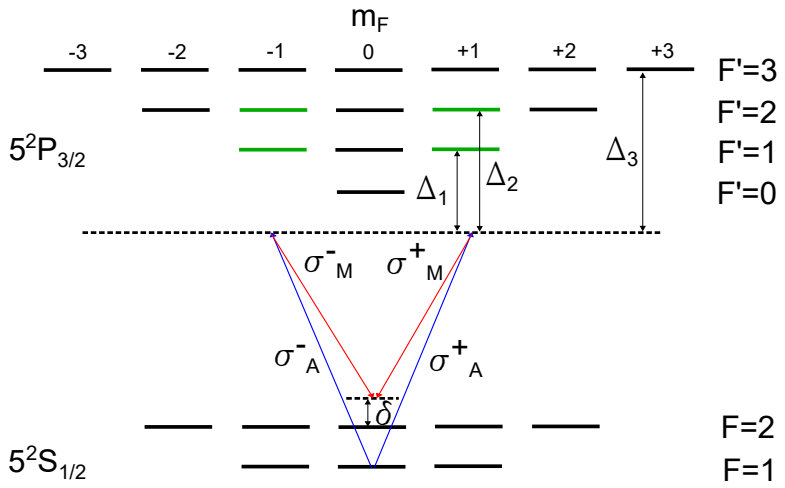


Figure 2.5: All energy levels present in the ^{87}Rb D_2 line. The transitions shown are the possible 2-photon stimulated Raman transitions which can be driven by σ^+/σ^+ and σ^-/σ^- transitions, highlighted with the superscripts + and -. The single photon transitions to and from the intermediate state are coloured to indicate the photons from the Master (red) and Apprentice (blue) lasers with subscripts M and A respectively. The detunings Δ_i correspond to the two-photon detunings from $|F' = i\rangle$. The states highlighted in green show the states which contribute to the effective two photon Rabi frequency in the interferometer.

$$\Omega^q_{\mathrm{g,i}} = \frac{\langle g|\, e\mathbf{r}\cdot\boldsymbol{\epsilon}^q_0\,|i\rangle}{\hbar}, \tag{2.32}$$

where q refers to the Δm_F of the transition (e.g. $q = +1 \rightarrow \Delta m_F = +1$) with amplitude $\boldsymbol{\epsilon}^q_0$, g refers to the initial state of the transition, and i refers to the final state of the transition, which will be the intermediate state in this case. For two photons which drive σ^+ transitions, the effective two-photon Rabi frequency is given by a sum over all possible intermediate states

$$\begin{aligned}\Omega^{+1,+1}_{\mathrm{eff}} &= \sum_{F'=1,2} \frac{\left(\Omega^{+1}_{\{1,0\},\{F',+1\}}\right)^* \left(\Omega^{+1}_{\{2,0\},\{F',+1\}}\right)}{2\Delta_{\{F',+1\}}} \\ &= \sum_{F'=1,2} \frac{\left(\Omega^{-1}_{\{1,0\},\{F',+1\}}\right) \left(\Omega^{+1}_{\{2,0\},\{F',+1\}}\right)}{2\Delta_{\{F',+1\}}},\end{aligned} \tag{2.33}$$

where the sum includes states $|F' = \{1,2\}, m_F = +1\rangle$. The $|F' = 3, m_F = +1\rangle$ state is not included, as it does not couple to the $|F = 1, m_F = 0\rangle$ state with a single photon transition. An equivalent Rabi frequency can also be written

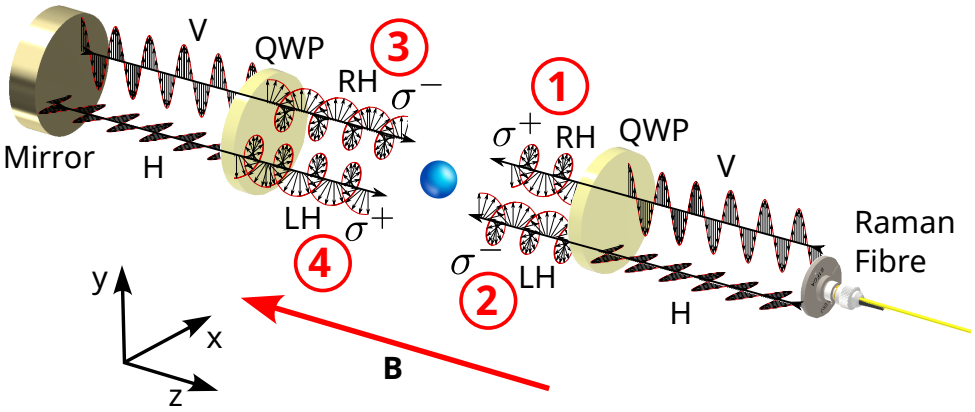


Figure 2.6: Light polarisations in each section of the Raman beam. A fibre delivers Master and Apprentice light in orthogonal, linear polarisations. A quarter waveplate converts this into orthogonal, circular polarisations. The beams pass through a second quarter waveplate and are reflected, before passing back through the second waveplate. This maintains their polarisation but flips the atomic transitions that each beam will drive. This creates two pairs of counter-propagating and two pairs of co-propagating beams which can drive stimulated Raman transitions.

for σ^-/σ^- transitions as seen in figure 2.5. In both cases, the overall effect is a Raman transition with $\Delta m_F = 0$.

2.4.1.1 Telescope Polarisation

To provide the required, circularly polarised light to the atoms, two frequencies of orthogonal, linearly polarised light are passed through a quarter waveplate. Figure 2.6 shows the polarisations at each stage of the Raman beam used in the experiment. To give perfect circularly polarised light, the axes of the waveplate would need to be angled at exactly 45 ° from the axes of linear polarisation. However, in practice, there will be a small misalignment, due to human error during positioning. To see how this impacts the interferometer, the Jones matrix for the optical system will be considered. The Jones matrix for a quarter waveplate at an angle, θ, from the horizontal is [48]

$$\mathrm{QWP}(\theta) = \begin{pmatrix} \frac{1}{\sqrt{2}} + \frac{i\cos(2\theta)}{\sqrt{2}} & \frac{i\sin(2\theta)}{\sqrt{2}} \\ \frac{i\sin(2\theta)}{\sqrt{2}} & \frac{1}{\sqrt{2}} - \frac{i\cos(2\theta)}{\sqrt{2}} \end{pmatrix}. \tag{2.34}$$

So for an angle $\pi/4 + \epsilon$ where ϵ is a small misalignment angle of the quarter waveplate, the matrix becomes

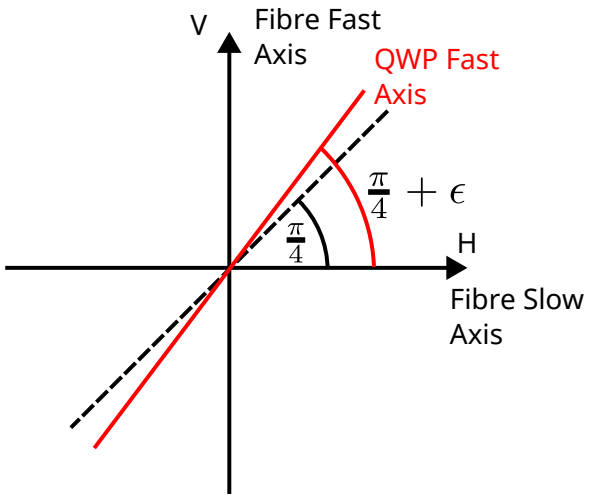


Figure 2.7: Definitions of axes of the quarter waveplate in the Raman telescope with respect to the polarisation maintaining fibre axes. ϵ is a small deviation angle from perfect angular alignment of the quarter waveplate.

$$\mathrm{QWP}\left(\frac{\pi}{4}+\epsilon\right) = \begin{pmatrix} \frac{1-2i\epsilon}{\sqrt{2}} & \frac{i}{\sqrt{2}} \\ \frac{i}{\sqrt{2}} & \frac{1+2i\epsilon}{\sqrt{2}} \end{pmatrix}, \tag{2.35}$$

which describes the system shown in figure 2.7. For horizontally polarised input light this gives

$$\mathrm{QWP}\left(\frac{\pi}{4}+\epsilon\right)\cdot\begin{pmatrix}1\\0\end{pmatrix} = \begin{pmatrix} \frac{1-2i\epsilon}{\sqrt{2}} \\ \frac{i}{\sqrt{2}} \end{pmatrix}, \tag{2.36}$$

which can be factorised into right and left handed components

$$\begin{aligned} \mathrm{QWP}\left(\frac{\pi}{4}+\epsilon\right)\cdot \mathrm{H} &= \begin{pmatrix} \frac{1-2i\epsilon}{\sqrt{2}} \\ \frac{i}{\sqrt{2}} \end{pmatrix} \\ &= \mathrm{L} + \frac{1}{\sqrt{2}}\begin{pmatrix}-2i\epsilon\\0\end{pmatrix} \\ &= \mathrm{L} - i\sqrt{2}\epsilon\ \mathrm{H} \\ &= (1-i\epsilon)\mathrm{L} - i\epsilon\ \mathrm{R}, \end{aligned} \tag{2.37}$$

where H, R and L are the Jones matrices for horizontal linearly polarised, right hand circularly polarised, and left hand circularly polarised light respectively. Following the same logic for vertically polarised input light, V, gives

$$\mathrm{QWP}\left(\frac{\pi}{4}+\epsilon\right)\cdot \mathrm{V} = (i-\epsilon)\mathrm{R} + \epsilon\ \mathrm{L}. \tag{2.38}$$

On passing through a quarter waveplate twice and being reflected, the polarisation is unchanged, but right handed light will now drive σ^- transitions and left handed light will now drive σ^+ as the beam k-vectors are anti-parallel to the magnetic field direction rather than parallel. The electric fields for the four beams are then

$$\begin{aligned}
\mathbf{E}_1 &= E_\mathrm{m}\cdot(i-\epsilon)\cdot R_{\uparrow\uparrow} + \epsilon L_{\uparrow\uparrow})\cos\left(k_\mathrm{m}z+\omega_\mathrm{m}t\right)\\
\mathbf{E}_2 &= E_\mathrm{a}\cdot(1-i\epsilon)\cdot L_{\uparrow\uparrow} - i\epsilon R_{\uparrow\uparrow})\cos\left(k_\mathrm{a}z+\omega_\mathrm{a}t\right)\\
\mathbf{E}_3 &= E_\mathrm{m}\cdot(i-\epsilon)\cdot R_{\uparrow\downarrow} + \epsilon L_{\uparrow\downarrow})\cos\left(k_\mathrm{m}z-\omega_\mathrm{m}t\right)\\
\mathbf{E}_4 &= E_\mathrm{a}\cdot(1-i\epsilon)\cdot L_{\uparrow\downarrow} - i\epsilon R_{\uparrow\downarrow})\cos\left(k_\mathrm{a}z-\omega_\mathrm{a}t\right),
\end{aligned} \tag{2.39}$$

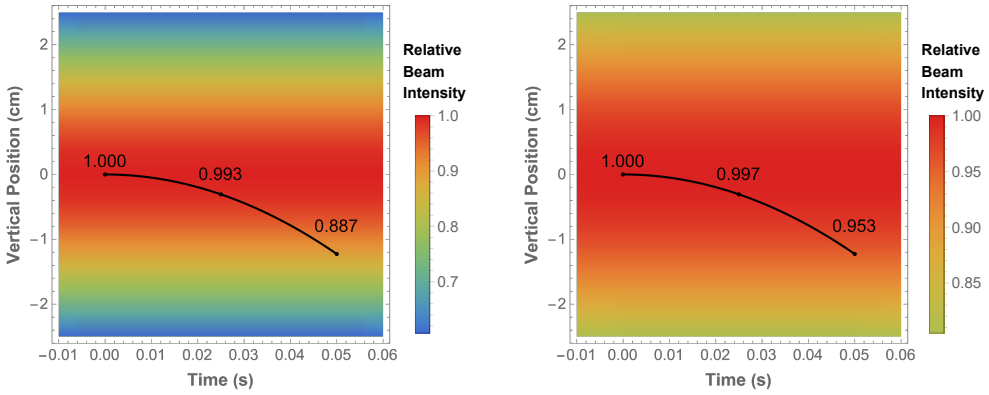
where $E_{\mathrm{m,a}}$ are the electric field strength of the Master and Apprentice beams, $k_{\mathrm{m,a}}$, and $\omega_{\mathrm{m,a}}$ are the wavenumber and frequency of the Master and Apprentice beams. The subscripts $\uparrow\uparrow$ and $\uparrow\downarrow$ refer to beams being aligned or anti-aligned to the magnetic field respectively. Then taking each combination of two beams with frequency difference $\omega_2-\omega_1$ which will drive σ^+/σ^+ or σ^-/σ^- transitions, the two-photon Rabi frequencies are

$$\begin{aligned}
\Omega_{12} &\propto 2E_\mathrm{m}E_\mathrm{a}\epsilon\\
\Omega_{34} &\propto 2E_\mathrm{m}E_\mathrm{a}\epsilon\\
\Omega_{14} &\propto E_\mathrm{m}E_\mathrm{a}\\
\Omega_{23} &\propto E_\mathrm{m}E_\mathrm{a},
\end{aligned} \tag{2.40}$$

ignoring small terms proportional to ϵ^2. Here, the subscript ij refers to the two photons coming from beams i and j from figure 2.6. The terms containing ϵ both refer to transitions where the two photons have the same k-vector direction, which are referred to as "co-propagating" transitions. These transitions can only be driven if there is some polarisation impurity in the Raman beam, such that $\epsilon \neq 0$. The terms without the ϵ are "counter-propagating" transitions which are Doppler sensitive and are used in the accelerometer.

2.4.2 Raman Beam Geometry

The Raman beam used in this experiment is a Gaussian beam with a $1/e^2$ width of 6 cm, truncated with an aperture. The reasons for truncation are discussed in chapter 4. Such a wide beam is used for two reasons. Firstly, as atoms fall perpendicularly to the Raman beam during the interferometer, variation in beam intensity will cause a proportional change in Rabi



(a) (b)

Figure 2.8: Simulated Raman beam intensities relative to the central intensity for a Gaussian beam with width 2.5 cm (a), and the real truncated Gaussian beam used in this experiment (b). The atom position is determined only by acceleration due to gravity, and the time between interferometer pulses is 25 ms. The two plots have the same colour scaling.

frequency, and therefore imperfect atom transfer during each interferometer pulse, reducing contrast. The wide beam ensures that the central region has a relatively flat intensity profile. Figure 2.8 shows the comparison of beam intensities for a 2.5 cm radius Gaussian beam, and the wide, truncated Gaussian beam used in this experiment. In each case, the atom starts at the centre of the Raman beam and falls under gravity with no initial, vertical velocity. The interferometer T-time is 25 ms in both cases. The wider beam allows more homogeneous beam intensities during the three interferometer pulses.

A second benefit of the wide beam is the increased interferometer times it allows. As atoms fall under gravity during the interferometry sequence, they will eventually fall out of the Raman beam. A wider beam increases the time before the atoms drop too far and can no longer be interacted with. Equation (2.29) shows that as the interferometer time, T, increases, the phase shift for a given acceleration will increase as T^2, meaning the sensitivity of the interferometer increases. The width of the Raman beam sets a limit on the achievable interferometer times, and therefore the sensitivity of the accelerometer.

2.4.3 Collimation Requirement

During interferometry, the phase imprinted on the atoms is the local laser phase at the time of each interferometry pulse. In the absence of any hori-

zontal acceleration, if the laser phase varies across the Raman beam, then, as atoms fall under gravity, the laser phase will be different during each pulse. When detecting the atomic state at the end of the interferometer, phase due to variations across the Raman beam will be interpreted as acceleration phase shifts, increasing the accelerometer error. For a perfectly collimated Raman beam, variation in phase from the incoming beam is cancelled by variation in the retro-reflected beam, such that the overall "effective phase wavefront" of the Raman beam is uniform. However, if the Raman beam diverges, this is no longer the case, and there will be phase variation across the beam.

The equation for the phase of the incoming and reflected part of the Raman beam, under the paraxial approximation is

$$\phi(r, z) = kz + k\frac{r^2}{2R(z)} - \psi(z), \tag{2.41}$$

where k is the beam wavenumber, r is the radial distance from the centre of the beam, $R(z)$ is the radius of curvature of the beam given by

$$R(z) = z\left(1 + \left(\frac{z_R}{z}\right)^2\right), \tag{2.42}$$

at longitudinal position z, $\psi(z)$ is the Gouy phase, and z_R is the Rayleigh range. As the focus is on wavefront inhomogeneity in the radial direction, kz and $\psi(z)$ can be ignored, as they do not vary with r. Accounting for the phase contributions of both incoming and retro-reflected beams gives

$$\phi_{\text{tot}}(r) = \frac{kr^2}{2}\left(\frac{1}{R(z_{\text{atom}})} - \frac{1}{R(z_{\text{atom}} + 2z_{\text{am}})}\right), \tag{2.43}$$

where z_{atom} is the longitudinal position of the atom cloud and z_{am} is the distance from the atom cloud to the retro-reflecting mirror. This can be substituted into equation (2.29) to calculate the total interferometer acceleration error due to a given divergence angle

$$\Delta a = \frac{\phi}{k_{\text{eff}}T^2}, \tag{2.44}$$

where k_{eff} is the effective wavenumber of the two beams contributing to the Raman beam, and T is the interferometer T-time. The result of this analysis for atoms falling under gravity, for a 25 ms interferometer T-time is shown in figure 2.9.

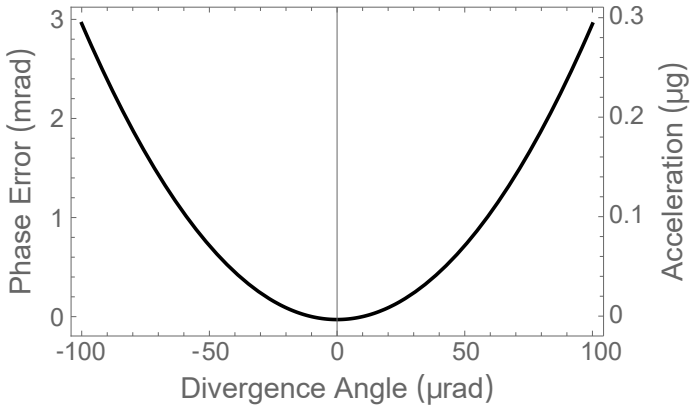


Figure 2.9: Phase and associated acceleration error for a 50 ms (2T) interferometer due to divergence or convergence of the Raman beam. The calculation is performed for atoms falling under gravity with no initial velocity.

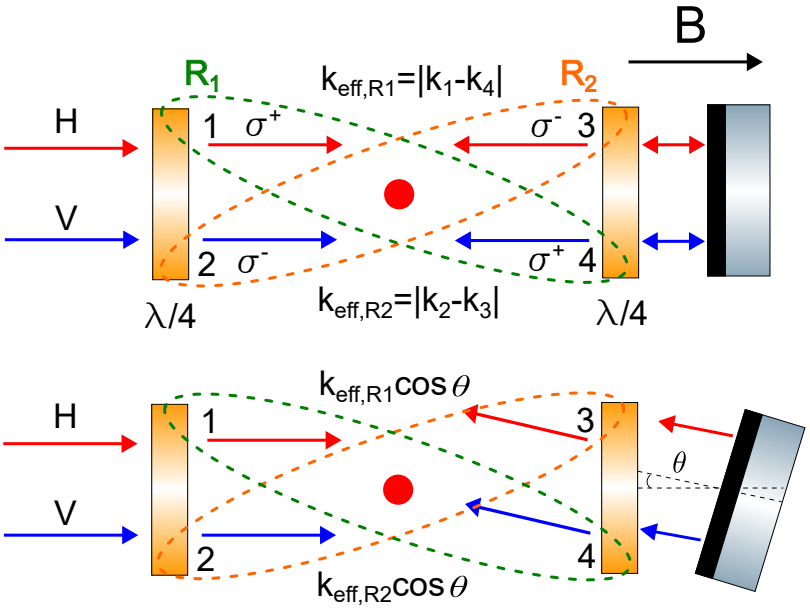


Figure 2.10: (a) All four beams which can be used to drive two-photon stimulated Raman transitions in the experiment. Beams from the Master and Apprentice lasers are coloured red and blue respectively. The two beam pairs, labelled R_1 and R_2, can drive Raman transitions with opposite momentum transfer. (b) The effect of Raman mirror misalignment. When the Raman mirror is misaligned by an angle θ, the effective k vector of the Raman beam is scaled by $\cos(\theta)$.

2.4.4 Raman Mirror Alignment

Figure 2.10 shows the path of the Raman light through the telescope, to the retro-reflecting "Raman mirror". When considering the Raman beam up to this point, the forward and reflected beams have always been considered as perfectly overlapping, such that their k-vectors are anti-parallel. Misalignment of the Raman mirror by an angle, θ, causes the k-vectors of the incoming and retro-reflected parts of the Raman beam to become misaligned. This causes the effective k-vector to be scaled by $\cos(\theta)$ such that the overall interferometer phase becomes

$$\begin{aligned} \Delta\Phi &= k_{\text{eff}} \cos(\theta) a T^2 \\ &\approx k_{\text{eff}} \left(1 - \frac{\theta^2}{2}\right) a T^2. \end{aligned} \tag{2.45}$$

This creates an additional phase of $-k_{\text{eff}}\theta^2 a T^2/2$, which will be interpreted as an erroneous acceleration.

2.4.5 The Double Interferometer

By creating two pairs of beams which can drive stimulated Raman transitions, two possible interferometers can be created, as seen in figure 2.11. The two interferometers give opposite momentum shifts, but are created using Raman pulses at the same time, with beams along the same path. As the physical separation between the clouds in each interferometer is negligible, the phase imparted onto the clouds during each interferometer will be equal in magnitude, but opposite in sign. This means that, if both interferometers are resonantly driven, their phases will cancel each other out, and the ratio of detected atoms in each energy state will be insensitive to acceleration. To counteract this effect, a velocity can be imparted onto the atomic cloud. The Doppler shift caused by atomic velocity along the Raman beam will shift the Raman transition frequencies for each interferometer in opposite directions, such that they are no longer resonant at the same frequency. If the Raman beam angular frequency is then tuned to be $\omega_{hf} \pm 2|\mathbf{k}_{\text{eff}} \cdot \mathbf{v}|$, where $\mathbf{v}$ is the atomic velocity and $\mathbf{k}_{\text{eff}}$ is the Raman beam effective k-vector, only one of the interferometers will be resonant with the Raman beams. By moving one of the interferometers away from resonance, the resonant interferometer can be selected, and the detected atom population ratio will be acceleration dependent.

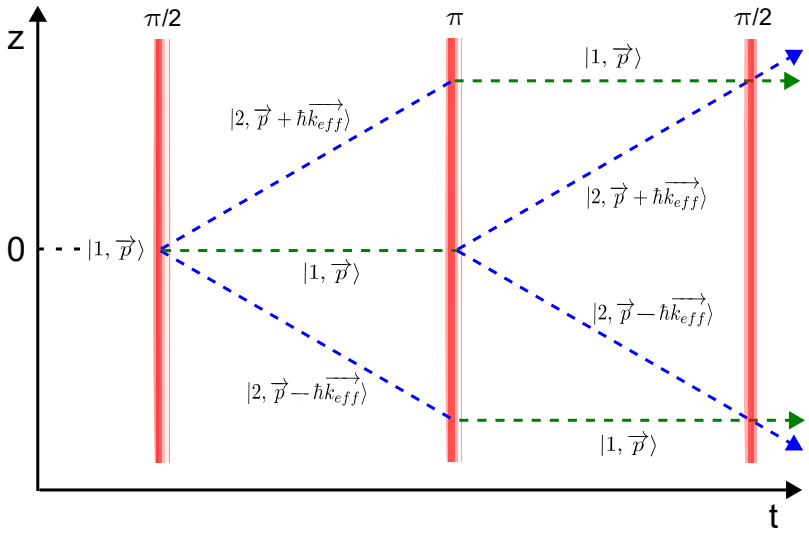
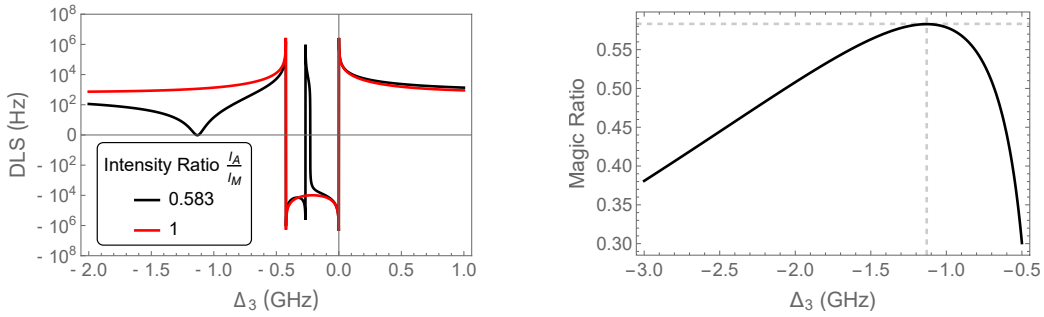


Figure 2.11: Time-space diagram showing the different atomic energy and momentum states during an interferometer when both counter-propagating interferometers are resonant with the atom. The interferometer phases from the two interferometers are of equal magnitude but opposite sign.

2.4.6 Differential Light Shift

In the presence of an oscillating electric field, such as that produced by the Raman beam, the AC Stark shift will cause a shift of the two hyperfine states used in the interferometer. In general, the shifts will be different for each state. The difference between the shifts of the two states will be referred to as the "differential light shift" (DLS). As the AC Stark shift is dependent on the laser beam frequency, without cancellation, laser frequency fluctuation will cause a change in the DLS, causing significantly different detunings during each interferometer pulse. The Stark shift is also dependent on laser beam intensity, so it is possible to choose a ratio of Master and Apprentice intensities, as well as a detuning from $|F' = 3\rangle$, Δ_3, for which the AC Stark shifts from each beam cancel each other out. Δ_3 is defined as in figure 2.5. Figure 2.12a shows a graph of the DLS for different values of Δ_3. In the case of equal Master and Apprentice intensities (red), there are two values of Δ_3 where the DLS cancels out, but at each of these detunings, a small change in laser frequency would cause a large increase in the DLS. When the intensities of the Master and Apprentice beams are imbalanced, a turning point appears in the DLS. The black line shows the DLS for an intensity ratio of 0.583. For a given value of Δ_3, the beam intensity ratio which gives a turning point in the DLS is referred to as the "magic ratio ",



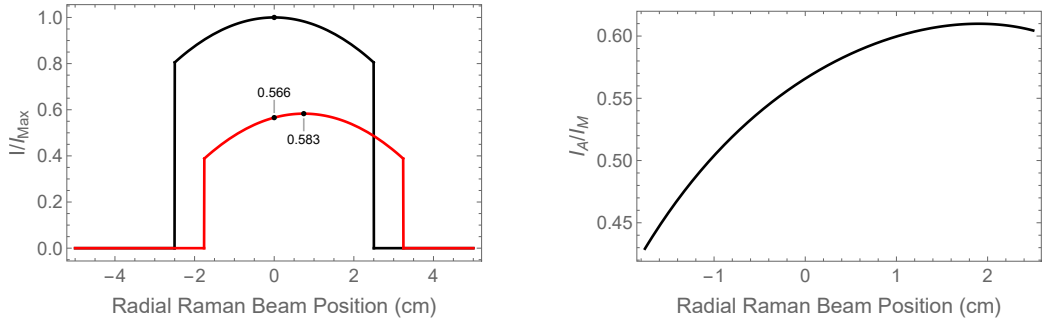
(a) (b)

Figure 2.12: (a) The differential light shift versus Raman beam detuning from $|F' = 3\rangle$ (Δ_3 as in figure 2.5) for an Apprentice to Master intensity ratio of 0.583 (black) and for equal Master and Apprentice intensities (red). For both graphs, the Master intensity was set to $1\,\mathrm{mW/cm^2}$, and the Raman beam polarisations were set to drive σ^+/σ^+ transitions. (b) The magic ratio versus detuning from $|F' = 3\rangle$. The gridlines show the turning point of the graph at a detuning of $-1.13\,\mathrm{GHz}$ and a magic ratio of 0.583. This detuning and magic ratio are used in the experiment. Both graphs are plotted from calculations by Prof. E. A. Hinds.

as at this detuning and intensity ratio, a small change in laser frequency will have a negligible effect on the DLS. The magic ratio is plotted against Δ_3 in figure 2.12b, and the gridlines show the turning point, where a change in Δ_3 has the smallest effect on the magic ratio. A detuning of $-1.13\,\mathrm{GHz}$ and a magic ratio of 0.583 are used in the experiment to cancel out the DLS, and minimise the impact of frequency variation.

2.4.6.1 Uncancelled Differential Light Shift and Beam Misalignment

The calculations used to plot the graphs in figure 2.12 assume that the intensity ratio of the Master and Apprentice light remain constant across the Raman beam. In the case of perfectly retro-reflected beams, this is indeed the case. However, if there is a misalignment of the Raman mirror, the intensity profiles of the incoming and retro-reflected beams will no longer be identical. If the intensity ratio of the Master and Apprentice beams is set such that the intensities at the centre of each beam are 0.583, as is required to cancel the DLS, figure 2.13a shows the beam profiles for a 1° misalignment of the Raman mirror. Figure 2.13b shows how the ratio of Apprentice to Master intensity varies radially across the Raman beam for the same misalignment. This will mean that not only will the DLS at the centre of the atom cloud not be properly cancelled, but that the DLS will vary across the atom cloud due to the cloud having a finite width. The uncancelled DLS



(a) (b)

Figure 2.13: (a) Theoretical beam intensities, relative to the central intensity of the Master light, in the Raman beam for the Master light (black) and Apprentice light (red), for a 1 ° misalignment of the Raman mirror. The marked points show the intensity ratio at the centre of the incoming Master light, and at the centre of the reflected Apprentice light. (b) Ratio of Apprentice to Master beam intensity at the axial atom position for a 1 ° misalignment of the Raman mirror.

will add a detuning to the generalised effective Rabi frequency in equation (2.20), which will change the Rabi oscillation frequency and amplitude for each atom differently. This will act as a dephasing mechanism which will reduce the system contrast.

Chapter 3

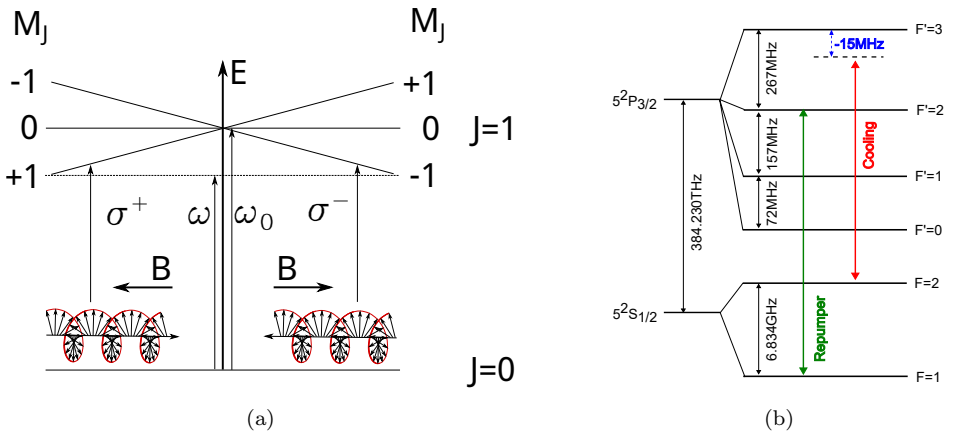
Atom Preparation

Atom interferometry requires a large ensemble of atoms to obtain measurements with a high signal to noise ratio. The atoms must be cooled to reduce their distribution of Doppler shifts, and allow interaction with Raman light over a period of tens of milliseconds. Section 3.1 describes how laser trapping and cooling techniques are used to achieve both of these requirements.

In a transportable accelerometer, robustness against varying magnetic fields is particularly important to prevent unwanted phase shifts of the interferometer. Section 3.2 will describe the process of preparing atoms in a magnetically insensitive energy level to limit the impact of background magnetic fields. I will then also describe how the selection of a narrow velocity class of atoms is used to reduce the effects of thermal dephasing on the interferometer.

3.1 Atom Trapping and Cooling

Since its development in the 1980s, the workhorse of atomic physics experiments has undoubtedly been the magneto-optical trap (MOT) [49, 50, 51]. The MOT is able to trap large atom numbers in three dimensions, while cooling them to around the Doppler temperature. Also in the 1980s, the optical molasses technique was developed [52, 53, 54]. When combined with an atom trap, such as the MOT, optical molasses allows atoms to be further cooled towards the recoil limit. Both the MOT and optical molasses are utilised in this experiment.



(a) (b)

Figure 3.1: (a) Schematic of a one-dimensional magneto-optical trap (1D-MOT). The vertical axis shows increasing energy. If an atom moves away from the trap centre, beams opposing its motion move closer to resonance, and after a large number of absorption-spontaneous emission cycles, the atomic velocity averages to zero. (b) Cooling and repumper transitions during magneto-optical trapping of ^{87}Rb.

3.1.1 1D MOT Theory

Consider a two-level atomic system with transition frequency ω_0, illuminated by a pair of counter-propagating cooling beams of frequency ω such that $\omega_0 > \omega$. If the atom moves in one direction, the beam opposing its motion will be Doppler shifted closer to resonance, increasing the absorption rate. The opposite will be true for the beam in the direction of travel. The atom may then undergo stimulated emission, and emit a photon back into the cooling beam, cancelling the initial momentum kick due to absorption, or it may spontaneously emit a photon in a random direction. Because the absorbed photon gives a momentum kick opposing the atom's motion, but the spontaneously emitted photon gives a momentum kick in a random direction, after a large number of absorption-spontaneous emission cycles, the momentum due to the spontaneously emitted photons will average out to zero, giving a net force in the direction opposing the atom's motion, creating a velocity dependent force that slows and cools the atoms down.

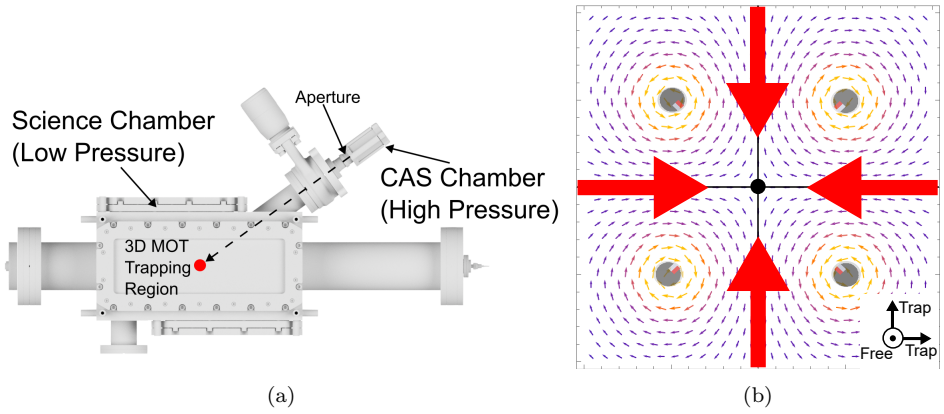
To create a trap for the atoms, a position dependent force is provided by the addition of a linear magnetic field gradient. Figure 3.1a illustrates how this field gradient induces a position-dependent Zeeman shift of the excited state energy level for a hypothetical atom with a $|J = 0\rangle$ groundstate. This means atoms which move away from the trap centre are more likely to scatter a photon from a beam which opposes this motion.

When only considering the two level system shown in figure 3.1a, atoms will indefinitely cycle back and forth between the two states. However, in reality, the excited state is usually more complex, and the effect of off-resonant scattering must be considered. In ^{87}Rb, off-resonant scattering to $|F' = 1\rangle$ and $|F' = 2\rangle$ allows atoms to decay into $|F = 1\rangle$, where they become dark to the cooling light. To drive atoms back into the cooling cycle, a second, "repumper" frequency of light can be added, which drives the $|F = 1\rangle \rightarrow |F' = 2\rangle$ transition. Atoms in $|F' = 2\rangle$ can decay into $|F = 2\rangle$, where they will continue to be cooled.

The atomic system shown in figure 3.1a, has a total angular momentum quantum number $|J = 0\rangle$ in its groundstate, which is not the case for ^{87}Rb. In reality, the groundstate will also experience a splitting in a magnetic field due to the presence of multiple Zeeman sub-levels. However, this does not change the working principle of the MOT described during this section, and the diagram was presented with no groundstate splitting for ease of understanding.

3.1.2 2D+ MOT

3.1.2.1 2D MOT



(a) (b)

Figure 3.2: (a) CAD design showing the science and CAS chambers. The two chambers are separated by an aperture to prevent pressure build up in the science chamber. (b) Schematic of the 2D MOT. Two pairs of counter-propagating beams, shown in red, containing cooling and repumper light trap atoms along the two trapping dimensions. The coloured arrows show the magnetic field which creates a cylindrically symmetric magnetic field gradient. The black spot shows the position of the trapped atoms, which are free to travel into or out of the page, along the free axis.

To load a MOT quickly, a high pressure of atoms is required. However, because collisions with background gas will cause dephasing of the interferometer, it is not desirable to have this high pressure in the main science chamber. Instead, a secondary, cold atom source (CAS) chamber, which contains a Rubidium dispenser, is attached to the science chamber, as shown in figure 3.2a. The two chambers are connected by a small aperture, which prevents pressure from building in the science chamber. Figure 3.2b shows the schematic of a two dimensional MOT, which is used to deliver light from the CAS chamber into the main science chamber. Two orthogonal pairs of counter propagating laser beams are transversely delivered into the CAS chamber, along with a cylindrically symmetric magnetic field gradient. This creates a beam of atoms which are trapped along two directions. The third, un-trapped axis is known as the "free-axis". The atomic beam is directed towards the zero of the 3D MOT magnetic field. This means that the efficiency of atoms entering the 3D MOT trapping region, is higher than if a high background pressure in the science chamber was used for loading. The 2D MOT cools the atoms transversely, but thermalisation within the cloud causes some axial cooling as well. This reduces the axial velocity of the atomic beam entering the science chamber. When loading into the 3D MOT, only atoms with velocity below the "capture velocity", which is determined by specific trap parameters, will be trapped. By pre-cooling the atoms in the 2D MOT, the efficiency of 3D MOT trapping is increased.

3.1.2.2 Push Beam

Despite the pre-cooling due to the 2D MOT, most of the atoms entering the science chamber will have an axial velocity greater than the 3D MOT capture velocity, and will not be trapped [55]. As the 2D MOT has no trapping along its free axis, and therefore no preferred direction of travel, the atomic velocity distribution is the same both towards and away from the main chamber. This means that approximately half of the atoms will travel away from the main chamber, and never reach the trapping region. To improve the 3D MOT trapping efficiency, a "push beam" can be included. This is a beam directed down the free-axis of the 2D MOT, towards the main chamber. This configuration is often called a "2D+ MOT". This beam accelerates atoms which previously had too low a velocity to reach the trapping region of the 3D MOT, and reverses the direction of some atoms which were previously moving away from the main chamber. By choosing the push beam power and frequency appropriately, a large number of atoms can be shifted to velocities where they can be trapped in the 3D MOT.

3.1.3 3D MOT

Figure 3.3 shows a schematic of the 3D MOT. Two coils with opposite current directions create a quadrupole magnetic field, which gives a cylindrically symmetric linear magnetic field gradient along each trapping direction. Three pairs of counter-propagating, circularly polarised beams, containing both cooling and repumper light, then trap atoms at the zero of the magnetic field.

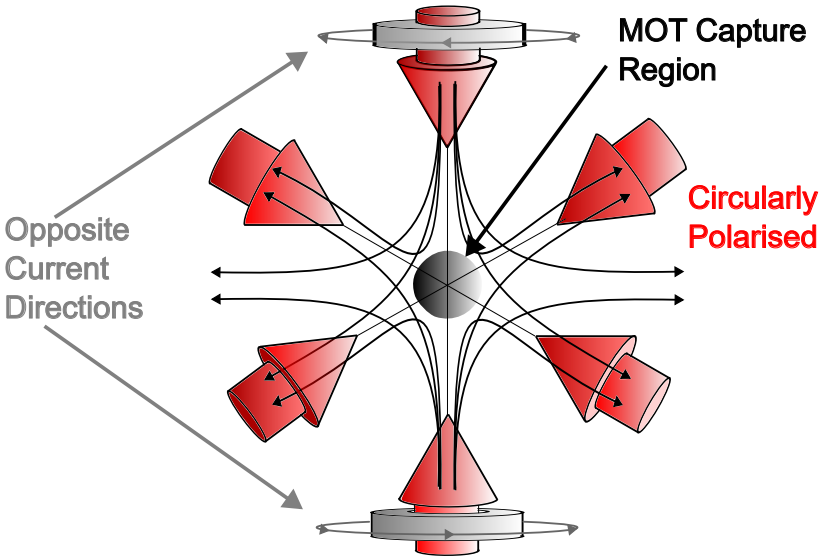


Figure 3.3: Schematic of the 3D MOT. Two coils with opposite current directions (grey lines) create a quadrupole magnetic field (black lines). Three pairs of circularly polarised beams, containing cooling and repumper light, trap the atoms in three dimensions. The trapping region is shown in black.

A 3D MOT is an efficient way of trapping a large number of atoms quickly, however its cooling is limited to the Doppler temperature. While the large number of absorption-spontaneous emission cycles during MOT cooling reduces the average velocity of the atoms to zero, the root mean squared velocity of the atoms is not zero, and as such they experience a random walk which limits their temperature. The Doppler temperature, T_D, is given by

$$T_D = \frac{\hbar\Gamma}{2k_B}, \tag{3.1}$$

where $\hbar$ is the reduced Planck constant, Γ is the transition linewidth, and k_B is the Boltzmann constant [56]. In ^{87}Rb this is 146 µK. To cool the atoms

further, to below around 10 µK, polarisation gradient cooling, also known as Sisyphus cooling, is used [53].

3.1.4 Sub-Doppler Cooling

3.1.4.1 Sisyphus Cooling

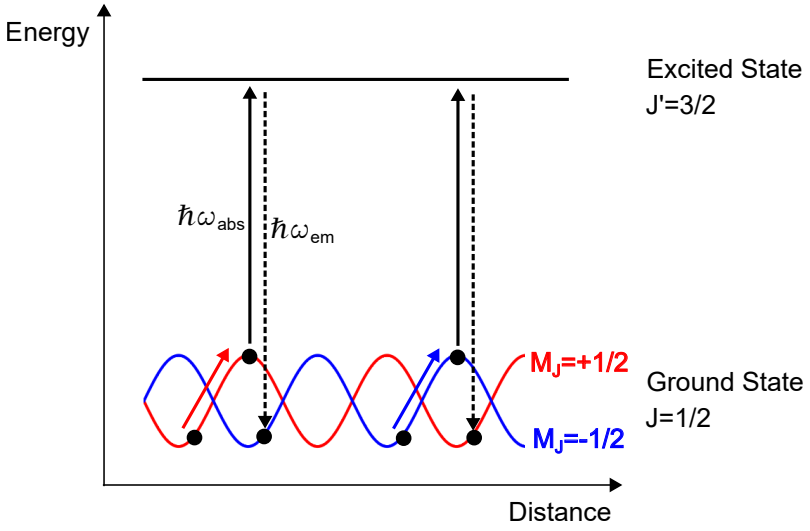


Figure 3.4: Working principle of Sisyphus, or polarisation gradient, cooling. The local polarisation varies with position, causing a periodic modulation of the AC Stark shift of the ground state M_J levels. Atoms at the top of a potential hill absorb a photon (solid line) and then spontaneously emit a photon (dashed line) of a higher frequency. Each absorption-spontaneous emission cycle reduces the atom energy by the height of the potential hill.

Consider two counter-propagating laser beams, of wavelength λ, with orthogonal polarisations. The beams will form a standing wave with a polarisation which is dependent on the relative phase of the two beams. This causes the resultant polarisation to become position dependent, with period $\lambda/4$. Now consider a two-level atom, with ground state $|J = 1/2\rangle$ and excited state $|J' = 3/2\rangle$, and incident laser beams red detuned from the transition. In the absence of any other energy shifts, the AC Stark shift caused by the light field, which depends on the local polarisation, lifts the degeneracy between the hyperfine levels of the atom's ground state. If the atom has a velocity along the standing wave, the position dependent light shift will cause a periodic change in the atom's ground state energy levels. This can be seen

in figure 3.4, where the ground state modulation creates a series of potential hills and valleys. As the atom moves through the standing wave, it will lose kinetic energy as it climbs a hill, and gain it as it falls into a valley. Consider the case where the atom is in $|M_J = -1/2\rangle$, and the local polarisation is σ^+. The atom can absorb a photon of energy $\hbar\omega_{\text{abs}}$ and be excited to the $|M'_J = +1/2\rangle$ state, whereupon it can spontaneously decay into either the $|M_J = -1/2\rangle$ state, in which case the process will restart, or the $|M_J = +1/2\rangle$ state. If the atom decays to $|M_J = +1/2\rangle$, the light will drive it into $|M'_J = +3/2\rangle$. This state does not couple to $|M_J = -1/2\rangle$, so the atom can only return to $|M_J = +1/2\rangle$. As the atom has moved from the top of a hill in $|M_J = -1/2\rangle$, to the bottom of a valley in $|M_J = +1/2\rangle$, it experiences an overall energy loss of $\hbar\omega_{\text{em}} - \hbar\omega_{\text{abs}}$, where $\hbar\omega_{\text{em}}$ is the energy of the spontaneously emitted photon. After several cycles of absorption and spontaneous emission, the atom will no longer have enough energy to climb a potential hill, and the cooling process will stop. To continue cooling, the potential hills can be reduced in height. The height of the potential hills can be approximated as

$$U_{Stark} = \frac{\hbar\Gamma^2 I}{8|\delta|I_{\text{sat}}}, \tag{3.2}$$

where δ is the red detuning from the transition frequency, I is the light intensity, and I_{sat} is the saturation intensity of the transition [57]. As U_{Stark} is proportional to $I/|\delta|$, the hill height can be reduced by increasing the beam detuning and decreasing the intensity. Once the atom can no longer climb a potential hill, its temperature will no longer change, meaning U_{Stark} can be related to the final atom temperature, T_{Sis},

$$\begin{aligned} U_{\text{Stark}} &= k_{\text{B}} T_{\text{Sis}} \\ T_{\text{Sis}} &= \frac{\hbar\Gamma^2 I}{8k_B|\delta|I_{\text{sat}}}. \end{aligned} \tag{3.3}$$

However, equation 3.3 implies that there is no lower limit on the temperatures achievable using Sisyphus cooling. In reality, the cooling process can continue until the energy loss from the atom moving from the top of a hill to the bottom of a valley is equal to the recoil energy, E_{r}, acquired when the atom spontaneously emits a photon. E_{r} can be calculated from the recoil velocity, v_{r} when emitting a photon

$$
\begin{aligned}
v_{\mathrm{r}} &= \frac{\hbar k}{m} = \frac{h}{m\lambda} \\
E_{\mathrm{r}} &= \frac{1}{2} m v_r^2 \\
&= \frac{h^2}{2m\lambda^2},
\end{aligned}
\tag{3.4}
$$

where k is the laser wavenumber, and m is the atomic mass [58]. This sets a limit on the achievable temperature, T_{r} using Sisyphus cooling,

$$
\begin{aligned}
T_{\mathrm{r}} &= \frac{E_{\mathrm{r}}}{k_B} \\
&= \frac{h^2}{2k_B m\lambda^2}.
\end{aligned}
\tag{3.5}
$$

For the D_2 line in ^{87}Rb, the recoil temperature is 362 nK. The processes of increasing the cooling detuning and decreasing the intensity will be referred to as the frequency and intensity molasses ramps respectively, and the combination of effects will be referred to as the "molasses ramp". This cooling mechanism relies on the fact that the AC Stark shift is the dominant effect on the energy levels in the cooling transition. If a magnetic field is present, there will be additional energy level splitting due to the Zeeman effect. To see which energy shift is likely to be dominant during Sisyphus cooling, the size of each can be compared for typical molasses ramp settings. For the ^{87}Rb cooling transition, the natural linewidth is $2\pi \times 6.065$ MHz. At the start of the molasses ramp, for a typical detuning of -15 MHz and a beam intensity of I_{sat}, equation 3.2 gives a frequency shift of 307 kHz. The Zeeman splitting of the energy levels in the ^{87}Rb cooling transition is $0.7\,\mathrm{MHz\,G^{-1}}$, so if Earth's field ($\sim 0.5$ G) is the dominant background field, this gives a shift of 350 kHz, already larger than the AC Stark shift. As the detuning and power are ramped, to give a colder temperature, the Stark shift decreases even further. If the detuning is increased to 50 MHz and the power decreased to $0.1 I_{\mathrm{sat}}$, the Stark shift becomes 9 kHz. The Zeeman shift causes the Sisyphus cooling to stop. To ensure that the Stark shift is the dominant energy shift throughout Sisyphus cooling, the background magnetic field is cancelled with three pairs of "bias coils". This process of field cancellation will be described in detail in section 4.7.2.

3.1.4.2 Molasses Sequence

Figure 3.5 shows the control sequence for the power and detuning of the cooling beams in both the 2D+ and 3D MOTs, as well as the 3D MOT coil

current, used to create the quadrupole magnetic field, during MOT loading and molasses stages. The ramps in frequency and power in figure 3.5 are shown to be linear, however this is not the case in reality. The frequency ramp is performed by linearly ramping the voltage to a piezo-electric actuator controlling the Master laser cavity length. While the piezo is initially set to be close to the centre of its range, its length change with voltage will not be perfectly linear. The power ramp is performed by ramping down the rf amplitude supplied to an accousto-optic modulator (AOM) which controls the cooling laser beams. In general, the AOM response to rf amplitude is not linear.

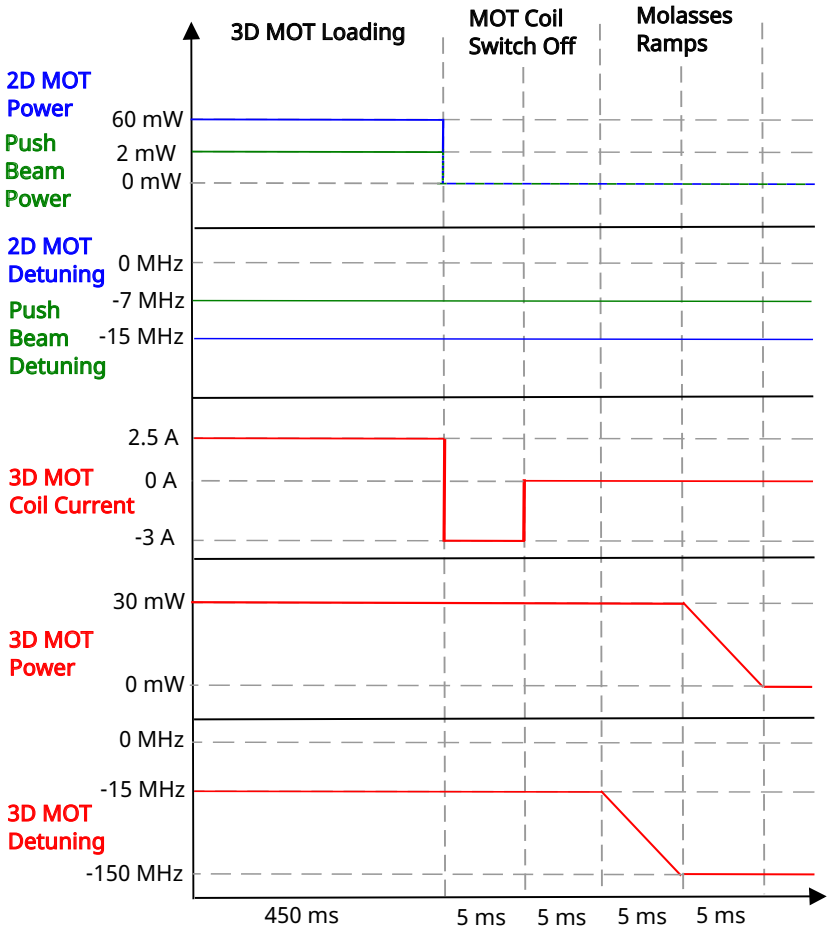


Figure 3.5: 2D and 3D MOT settings during MOT loading and molasses stages. While the molasses ramps shown are linear in frequency and power, in reality these ramps have a nonlinear shape.

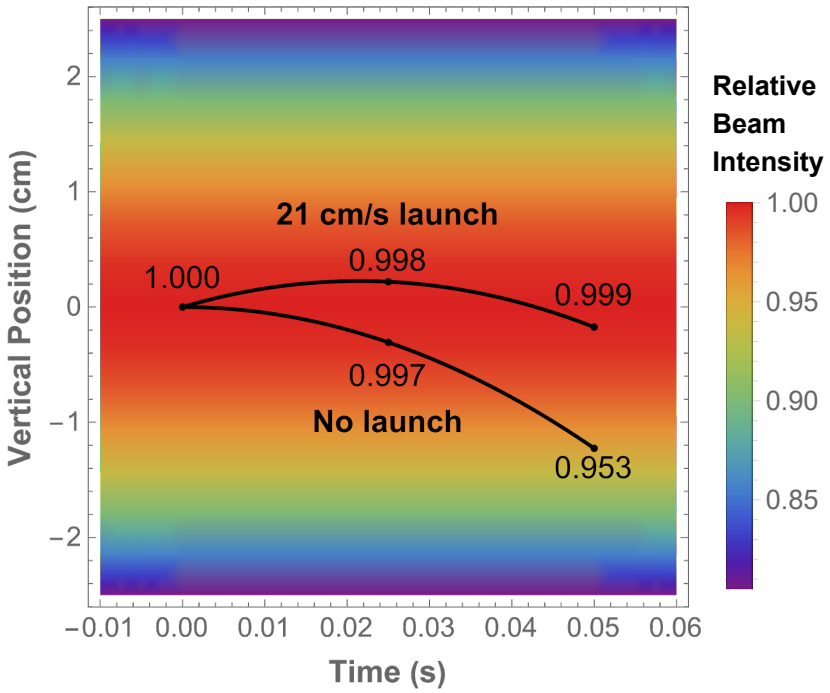


Figure 3.6: Theoretical Raman beam intensities during each interferometer pulse relative to the central intensity. The upper trajectory has an optimised vertical launch of 21 cm s^{-1}, and the lower trajectory has no initial velocity. Both trajectories fall under gravity during the 50 ms interferometer 2T-time.

3.1.5 Atom Launch

During the interferometer sequence, the atom cloud is "launched" both vertically and horizontally. A vertical launch is used to keep the atom cloud close to the centre of the Raman beam, improving the homogeneity of the Raman beam intensities during each interferometer pulse, improving contrast. Figure 3.6 shows theoretical Raman beam intensities relative to the intensity at the centre of the Raman beam, for two atom trajectories during a 25 ms T-time interferometer. The upper trajectory has a 21 cm s^{-1} vertical launch, and the lower trajectory has no initial velocity. The launch velocity was chosen to minimise the distance of the atoms away from the beam centre, and therefore reduce the variation in Raman beam intensity. Section 2.4.5 described how two different pairs of beams can be used to create acceleration sensitive interferometers in this experiment. The two interferometers have equal and opposite responses to acceleration, so their effects will cancel each other out. To remove the degeneracy of the double interferometer, the atom cloud is launched horizontally, giving a constant velocity along the Raman beam during the interferometer. The two pairs of beams experience opposite

Doppler shifts, and by tuning the Raman beam frequency appropriately, one interferometer can be "selected", while the other will be off-resonant.

3.1.5.1 Moving Molasses

To launch the atoms, a "moving molasses" technique is used. In the optical molasses described in section 3.1.4.1, the two counter-propagating cooling beams have equal frequency, so that any atomic motion in the lab frame is opposed. However, if one beam is increased in frequency by $\delta f_v = \delta v/\lambda$, where λ is the laser wavelength, and the opposing beam is decreased by the same amount, then the atoms will be cooled into a reference frame moving with a velocity δv. In other words, the atoms will still be cooled as previously described, but the mean velocity will be non-zero. In the horizontal plane, the two MOT beams used to launch the atoms are angled at 45° to the Raman beam, so the frequency shift applied to each beam is $\delta f_h = \delta v/\sqrt{2}\lambda$. Figure 3.7 shows the control sequence used for the launching MOT beams during the moving molasses. The overall cooling beam detuning is varied by

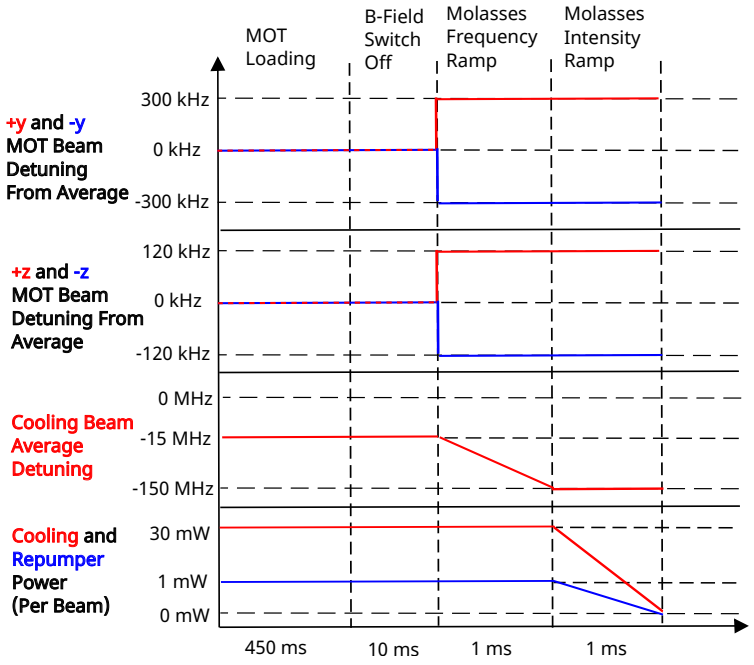


Figure 3.7: Control sequence for the cooling and repumper frequencies and powers during MOT loading and moving molasses. Red lines show changes in the cooling light, blue lines show changes in repumper light, and red/blue dashed lines show changes of both simultaneously.

ramping the actuator controlling the Master laser cavity length, which affects all MOT beams at the same time. The frequency step for the moving molasses is performed by changing the frequency of the fibre-coupled AOMs which are used to control each MOT beam individually. In this figure, the vertical (y) launch frequency is 300 kHz, corresponding to a vertical launch velocity of $300\,\text{kHz} \times 780\,\text{nm} = 23.4\,\text{cm}\,\text{s}^{-1}$ and the horizontal (z) launch frequency is 120 kHz, corresponding to a horizontal launch velocity of $120\,\text{kHz} \times \sqrt{2} \times 780\,\text{nm} = 13.2\,\text{cm}\,\text{s}^{-1}$. While the settings for the moving molasses were often changed, these values are typical for what was used during the experimental sequence.

3.2 State Selection

To improve the robustness of the experiment to both time and position-varying magnetic fields, atoms are prepared in the $|F = 1, m_F = 0\rangle$ state. This state is not affected by first order Zeeman shifts, but does experience a second order shift of $575\,\text{Hz}/\text{G}^2$. Because the second order shift is relatively small compared to the Zeeman shift of the other sub-levels within $|F = 1\rangle$, the $m_F = 0$ state will often be referred to as a "magnetically insensitive state".

After preparing atoms in the $|F = 1, m_F = 0\rangle$ state, their velocity distribution is determined by their temperature. To reduce the effect of Doppler shifts due to thermal motion causing interferometer dephasing, atoms can be "velocity selected". By selecting atoms within a narrow velocity class, and removing all other atoms from the experiment, the width of the cloud velocity distribution is narrowed, and thermal dephasing effects are reduced.

3.2.1 Preparation Scheme

This section will give a brief overview of each state selection stage, before each is described in more detail in the following sections. The process of preparing the atomic cloud is performed in six stages:

Stage 1- After the optical molasses stage, almost all atoms are in $|F = 2\rangle$. The Master laser is tuned to the $|F = 2\rangle \rightarrow |F' = 2\rangle$ transition. Atoms are optically pumped from $|F = 2\rangle$ to $|F = 1\rangle$ via the intermediate state $|F' = 2\rangle$.

Stage 2- After state selection stage 1, the atoms are evenly distributed be-

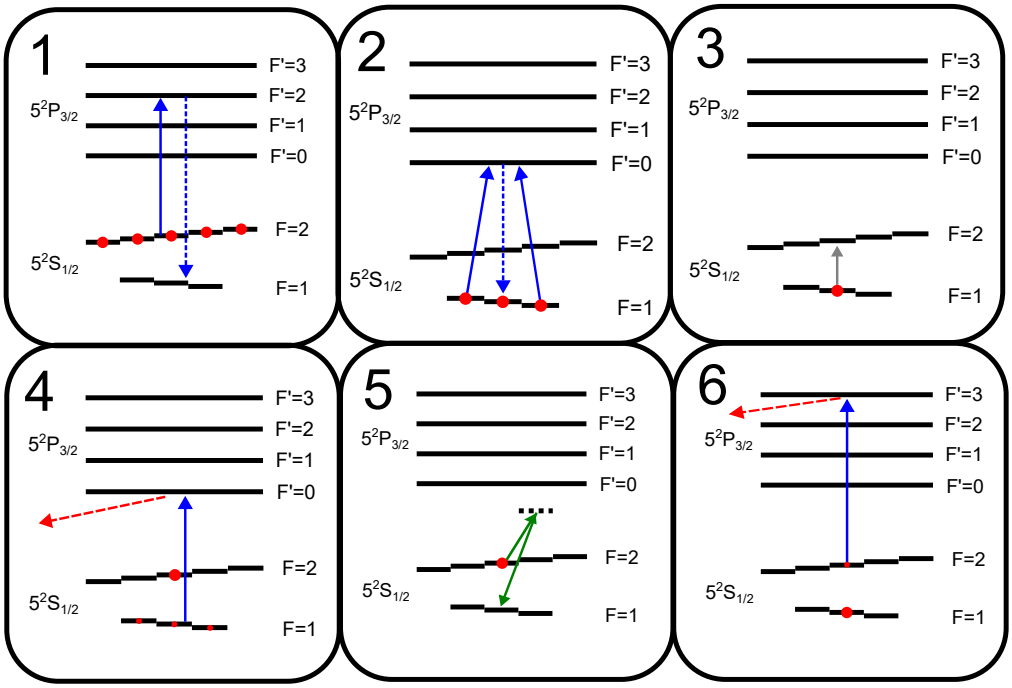


Figure 3.8: Different stages of atom preparation during the experiment. Blue lines show optical pumping from light provided by MOT beams, grey lines indicate microwave transitions, green lines show stimulated Raman transitions, and red lines show atoms being blown away. Large red dots indicate a large number of atoms in a given state, whereas small red dots indicate a small atom number.

tween the three Zeeman sub-levels of $|F = 1\rangle$. The Apprentice laser is tuned to the $|F = 1\rangle \rightarrow |F' = 0\rangle$ transition. Atoms are optically pumped into $|F = 1, m_F = 0\rangle$ via the intermediate state $|F' = 0\rangle$.

Stage 3- A microwave pulse drives the atoms from $|F = 1, m_F = 0\rangle$ to $|F = 2, m_F = 0\rangle$.

Stage 4- A pulse from the Apprentice laser is applied in one direction, resonant with the $|F = 1\rangle \rightarrow |F' = 0\rangle$ transition. As the pulse is not balanced by a counter-propagating beam, it acts to push atoms away. This "blows away" any atoms from $|F = 1\rangle$ which were not transferred by the microwaves.

Stage 5- After the $|F = 1\rangle$ blowaway, atoms are all in the $|F = 2, m_F = 0\rangle$

state with a velocity distribution width determined by their temperature. A velocity selective, 2-photon stimulated Raman transition transfers the slower moving atoms from $|F = 2, m_F = 0\rangle$ to $|F = 1, m_F = 0\rangle$.

Stage 6- A blowaway pulse from the Master laser 1 MHz detuned from the $|F = 2\rangle \rightarrow |F' = 3\rangle$ transition removes the faster moving atoms which were not transferred during the velocity selective pulse.

3.2.2 Stage 1 - Pumping Atoms Into $|F = 1\rangle$

After the optical molasses stage, all of the atoms will be in the $|F = 2\rangle$ level due to the presence of the repumper beam. The first stage of state preparation is to optically pump all atoms in the experiment into $|F = 1\rangle$. Resonant light drives atoms from $|F = 2\rangle$ into $|F' = 2\rangle$. After being pumped into the $|F' = 2\rangle$ state, atoms can spontaneously decay into the $|F = 1\rangle$ ground state, where they become dark to the applied light field. In the case of zero magnetic field, there will be static dark states in $|F = 2\rangle$ which will prevent atoms from being pumped. These states can be "destabilised" by applying a magnetic field along the direction of the driving field [59], and the time to drive atoms into $|F = 1\rangle$ will depend on the strength of the applied magnetic field [43].

3.2.3 Stage 2 - Pumping Atoms into $|F = 1, m_F = 0\rangle$

After state selection stage 1, atoms will be distributed amongst the three different Zeeman sub-levels of $|F = 1\rangle$. To drive the magnetically insensitive $|F = 1, m_F = 0\rangle \rightarrow |F = 2, m_F = 0\rangle$ transition, atoms must all be driven into $|F = 1, m_F = 0\rangle$. By applying two counter-propagating, circularly polarised beams resonant with the $|F = 1\rangle \rightarrow |F' = 0\rangle$ transition, along with a uniform magnetic field parallel to the beam k-vectors, σ^+ and σ^- transitions will drive atoms in $|F = 1, m_F = \pm 1\rangle$ into $|F' = 0, m'_F = 0\rangle$. Once in $|F' = 0, m'_F = 0\rangle$, atoms can only decay into $|F = 1, m_F = 0\rangle$, where they, along with atoms already in that state, become dark to the incident light. After this stage, in the absence of any off-resonant scattering, all atoms will be in $|F = 1, m_F = 0\rangle$.

3.2.4 Velocity Selection

The probability of an atom, initially in $|F = 1\rangle$, being excited to $|F = 2\rangle$ from a single Raman pulse is given by

$$P_2(\tau) = \frac{\Omega_{\text{eff}}^2}{\Omega_{\text{G}}^2} \sin^2\left(\frac{\Omega_{\text{G}}\tau}{2}\right), \tag{3.6}$$

from equation (2.18), where $\Omega_{\text{G}} = \sqrt{\Omega_{\text{eff}}^2 + \delta^2}$. This shows that as the two photon detuning, δ, is increased, the excitation probability is decreased. In a full interferometry sequence, when this is extended to an ensemble of atoms, with a distribution of detunings, this causes a reduction in interferometer contrast. Atoms with a finite temperature will have a distribution of velocities, and therefore Doppler shifts, given by the Maxwell-Boltzmann distribution, which give each atom a different two-photon detuning. The higher the atom cloud temperature, the wider the distribution of Doppler shifts, and therefore the lower the interferometer contrast. Sub-Doppler cooling reduces the cloud temperature to a few µK, reducing the dephasing to a level where interference can be observed [60]. To narrow the velocity distribution further, a velocity sensitive Raman pulse can be used to select a velocity class of atoms, before a blowaway pulse removes those not in that velocity class. This can be thought of as reducing the cloud's "effective temperature" in order to improve the interferometer contrast.

3.2.4.1 Stage 3 - Microwave Transfer

The first stage of velocity selection is to drive atoms into $|F = 2, m_F = 0\rangle$ using a microwave pulse. A microwave pulse is used, rather than a two-photon optical pulse, as the Doppler shift of a microwave pulse will be much smaller than for the optical pulse, due to its longer wavelength. As a result, all atoms, except those of very high velocity will be transferred during a microwave pulse. Due to the low atom temperature, there should be very few atoms with such high velocities, and the microwave transition efficiency should be close to 1. As a result, the microwave pulse is referred to as "velocity insensitive". The microwave pulse is a magnetic dipole transition, and so the transition rate is proportional to $\boldsymbol{\mu} \cdot \mathbf{B}$, where $\boldsymbol{\mu}$ is the atom's magnetic dipole moment, and $\mathbf{B}$ is the magnetic field of the microwaves. To align the two, a magnetic field is applied perpendicularly to the microwave propagation direction, which provides a quantisation axis for the atoms' dipole moments.

3.2.4.2 Stage 4- $|F = 1\rangle$ Blowaway

Despite the microwave pulse being velocity insensitive, it may not have an efficiency of 1. Effects such as collisional dephasing due to background gas, and misalignment of the applied quantisation magnetic field, can cause reduced transfer efficiency. Any atoms which are not transferred by the microwave

transition, will be in the wrong state during interferometry, and will add to the accelerometer noise. To remove them, a "blowaway" pulse can be used to remove them from the system. By applying an unbalanced incident beam, resonant with the $|F = 1\rangle \rightarrow |F' = 0\rangle$ transition, atoms remaining in $|F = 1\rangle$ will be pushed away from the rest of the cloud, and out of the experiment.

3.2.4.3 Stage 5 - Velocity Selective Pulse

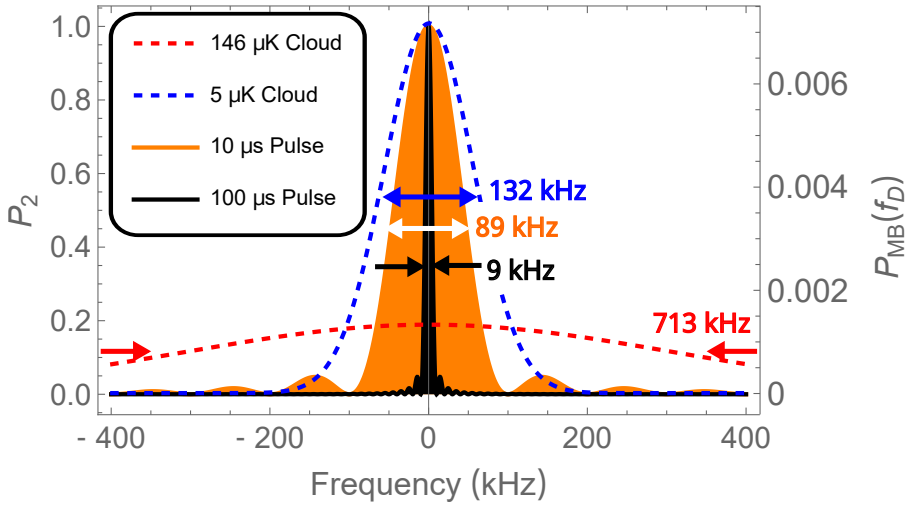


Figure 3.9: The excitation probability, P_2 of an atom, initially in $|F = 1\rangle$ for single Raman pulses of 10 µs and 100 µs, and the Maxwell-Boltzmann probability distribution of Doppler shifts for atom clouds of 5 µK and 146 µK. The arrows show the full, $1/e^2$ width of each Maxwell Boltzmann distribution, and the full width at half maximum of the central peak of each P_2 distribution.

After the microwave pulse and $|F = 1\rangle$ blowaway, all atoms should be in the $|F = 2, m_F = 0\rangle$ state. Figure 3.9 shows a plot of the excitation probability, from equation (2.18), for two Raman pulse durations of 10 µs and 100 µs, and the probability distribution of Doppler shifts for atom clouds of 5 µK and 146 µK. As the linewidth of a Raman pulse is narrower for longer pulse durations, the length of a Raman pulse can be tuned to transfer only atoms with a narrow velocity class from $|F = 2, m_F = 0\rangle$ to $|F = 1, m_F = 0\rangle$. This highlights a further need to cool the atom cloud effectively during the molasses cooling stage of the experiment. If the atom cloud is at 146 µK, fewer atoms will lie within the selected velocity class than for a 5 µK cloud, which will decrease the number of atoms which can subsequently take part in the interferometer.

3.2.4.4 Stage 6 - $|F = 2\rangle$ Blowaway

After the selected velocity class of atoms are transferred to $|F = 1, m_F = 0\rangle$, those remaining in $|F = 2, m_F = 0\rangle$ are removed with a blowaway pulse. An un-balanced beam 1 MHz detuned from the $|F = 2\rangle \rightarrow |F' = 3\rangle$ transition pushes all of the unselected atoms away from the rest of the cloud and out of the experiment.

Chapter 4

Experimental Apparatus

4.1 Apparatus Overview

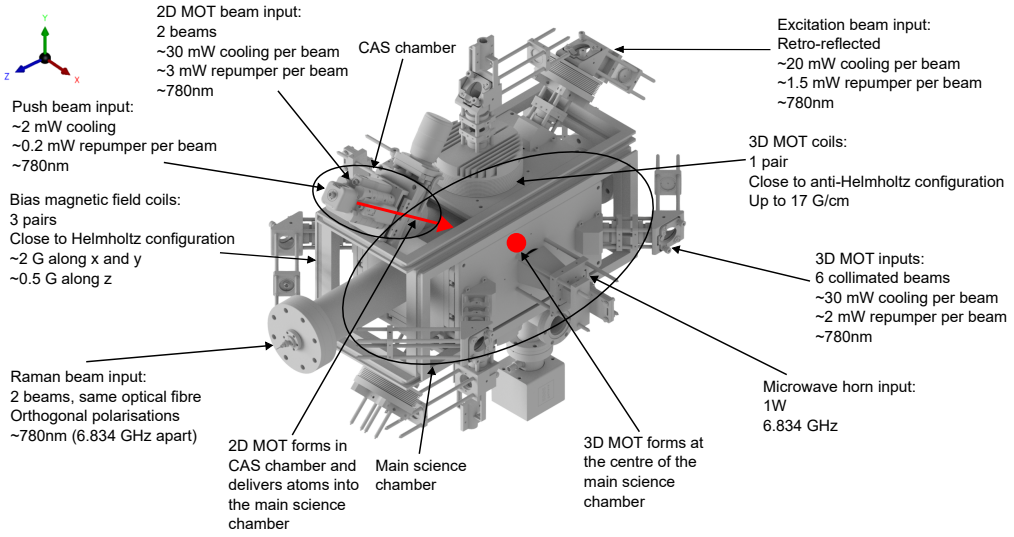


Figure 4.1: A CAD image of the main science chamber used in this experiment. Summaries of each optical input to the chamber, including powers and wavelengths are shown. All light is delivered to the chamber in optical fibres. The microwave input, with a summary of power and frequency is also shown. The microwaves are delivered by a horn waveguide. Magnetic field coils are also summarised, giving maximum magnetic field strength, for bias coils, and magnetic field gradient, for MOT coils.

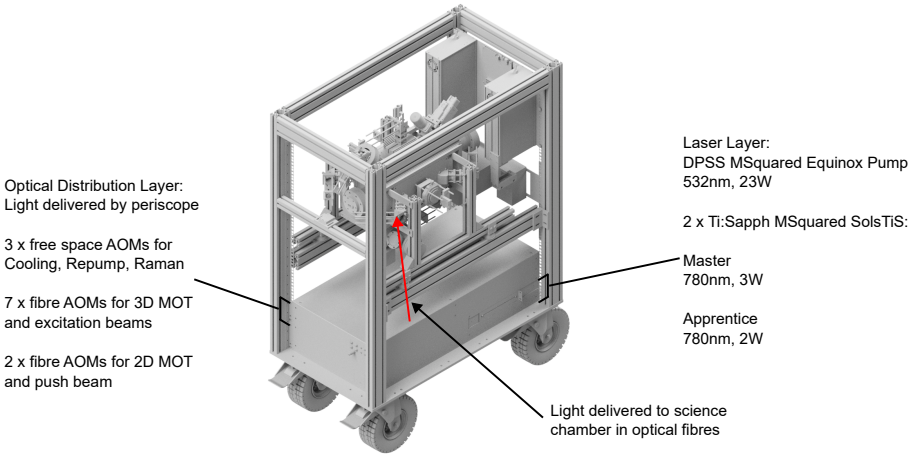


Figure 4.2: A CAD image of the 19-inch rack which houses the main science chamber and laser system. Summaries of the laser output powers and wavelengths, as well as the acousto-optic modulators used to control the light being delivered to the science chamber, are also shown.

4.2 Laser System and Optical Distribution

4.2.1 Laser System

Figure 4.3 shows an energy level diagram of the ^{87}Rb D_2 line, together with all of the laser frequencies used in the experimental sequence. From this point onwards only atomic transitions shown in figure 4.3 will be considered, and energy level labels will be dropped for readability. Transitions will be labelled in accordance with section 2.1, where an apostrophe will describe energy levels within the $5^2P_{3/2}$ level. For example, a transition from $5^2S_{1/2}, |F = 2\rangle$ to $5^2P_{3/2}, |F = 3\rangle$ will be referred to as $|F = 2\rangle \rightarrow |F' = 3\rangle$.

Two M-Squared SolsTiS Titanium-Sapphire (Ti:Sapph) lasers are phase locked together at a controllable frequency offset from each other to provide light for cooling and trapping, interferometry, and detection. The two Ti:Sapph lasers are pumped by the same 23 W M-Squared 532 nm Equinox diode pumped solid state (DPSS) laser to give outputs of 3.5 W and 2.5 W at 780 nm. The laser used to address the states $|F = 2\rangle$ and $|F = 1\rangle$ are known as the "Master" and "Apprentice" respectively. Figure 4.4 shows the optical setup of the experiment, including the pump and two Ti:Sapph lasers. The two SolsTiS lasers have the same internal components, other than the Apprentice laser containing an inter-cavity EOM. This is used to modulate the Apprentice

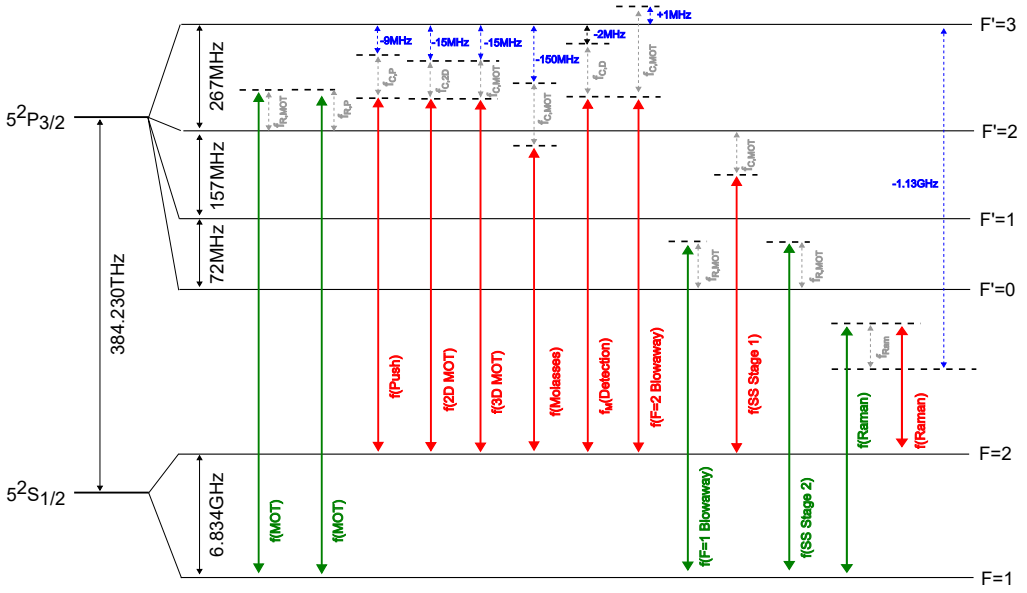


Figure 4.3: Energy levels for the D_2 line in ^{87}Rb, with transition frequencies for each experimental step labelled. Apprentice and Master light frequencies are coloured green and red respectively. The frequencies added by AOMs are coloured grey, and detuning from resonance with a transition is coloured blue. AOM frequencies are labelled with subscripts corresponding to which AOMs contribute to the frequency shift. The subscripts are as follows: repumper (R), cooling (C), MOT (MOT), push (P), 2D MOT (2D), Raman (Ram).

laser phase, which is described in section 4.2.2.2. The absolute frequency of the Master laser is stabilised to the $|F = 3\rangle \rightarrow |F' = (3, 4)\rangle$ crossover transition in ^{85}Rb using frequency modulation spectroscopy. This will be referred to as the "vapour cell" lock and is described in detail in section 4.2.2.1. The relative frequency of the Apprentice laser relative to the Master laser is stabilised through a phase-lock, which is described in section 4.2.2.2.

4.2.2 Laser Stabilisation

4.2.2.1 Vapour Cell Lock

Figure 4.5a shows a diagram of the saturation absorption spectroscopy setup used to reference the Master laser frequency. Saturated absorption spectroscopy is performed in a cell of ^{85}Rb gas, and the difference between the two photodiodes, PD1 and PD2, gives the Doppler free saturated absorption spectrum. This signal is referred to as the "photodiode difference signal". Figure 4.5b shows this difference signal for the $|F = 3\rangle \rightarrow |F'\rangle$ transitions. To reference the laser to the gas cell, the Master light is passed through an

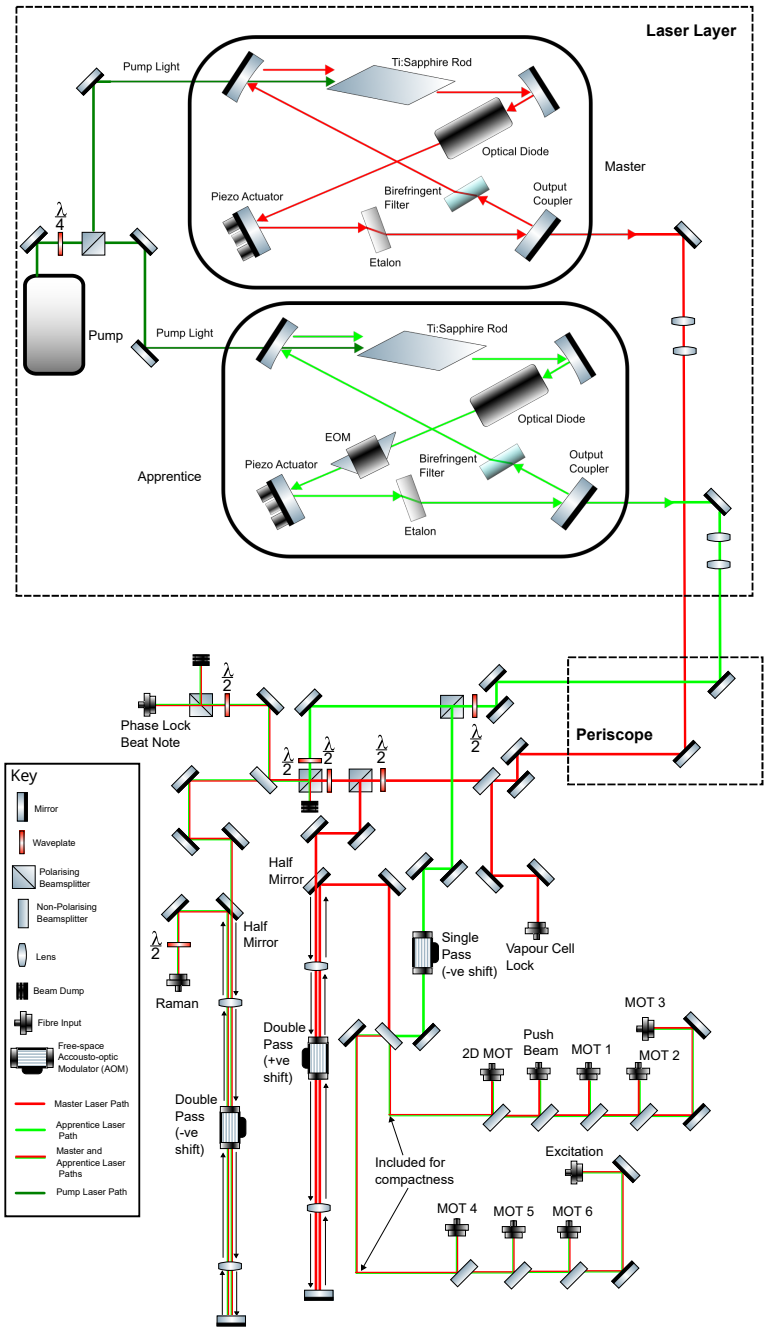
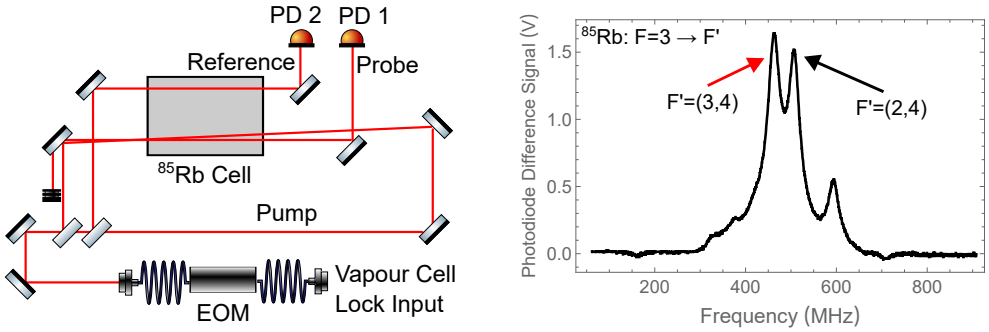


Figure 4.4: Schematic of the optics used for the distribution of laser light during the experiment. The pump laser and two Ti:Sapph lasers are on one layer, which is connected via a periscope to the optics layer above. Two points (labelled) show changes in beam direction with no optics. These are included for compactness of the figure and are not present in the real system.



(a) (b)

Figure 4.5: a) Vapour cell lock saturation absorption spectroscopy set up. Photodiode (PD) 1 measures the combined Doppler-broadened and hyperfine Lamb dip spectrum, PD 2 measure only the Doppler broadened spectrum. The vapour cell lock input is shown in figure 4.4. b) The photo diode difference signal (PD 2 - PD1) provides a Doppler-free saturated absorption spectrum. Here, the $|F = 3\rangle \rightarrow |F'\rangle$ transitions in the D_2 line of ^{85}Rb are shown, including crossover peaks. The $F' = (3, 4)$ crossover peak generates the strongest signal and is used to provide an absolute frequency reference for the Master laser.

Electro-Optic Modulator (EOM). When a signal from a voltage controlled oscillator (VCO) is applied to the EOM, the output is a main "carrier" frequency as well as sidebands which are separated from the carrier by the frequency of the VCO. The input to the EOM is labelled "Vapour Cell Lock" in figure 4.4. The first blue sideband is locked to the $|F = 3\rangle \rightarrow |F = (3, 4)\rangle$ crossover frequency shown in figure 4.5b. To lock the EOM sideband, we apply a 20 kHz "dither" to the VCO frequency, which modulates the sideband back and forth over the spectral feature being locked to. This converts the frequency modulation into an amplitude modulation of the photodiode difference signal. The amplitude of the oscillating signal will be proportional to the slope of the spectral feature at the central frequency of the modulation. When this signal is mixed with the original dither signal used to modulate the EOM, a DC signal is obtained which is the derivative of the spectral feature. By feeding this "error signal" back to the Master laser cavity actuator, which controls the cavity length, the signal can be kept close to zero, stabilising the sideband to the top of the spectral feature [61]. This feedback is performed inside the laser cavity, and so the error signal is not available to the user. With the sideband stabilised in frequency, the VCO voltage can be varied to change the frequency of the central "carrier" frequency, to any desired frequency within the bandwidth of the EOM. During the experimental sequence, the VCO frequency is varied over a range of 1.38 GHz to 2.04 GHz.

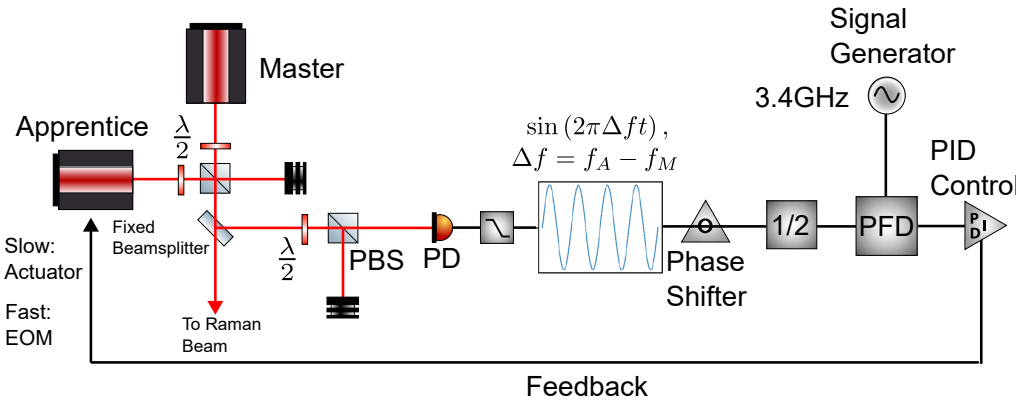


Figure 4.6: Phase lock set-up. The Master and Apprentice light is combined to give a beat-note which is detected with a high-speed photodiode. The summed frequency is too high to be detected, and the difference frequency is halved before passing into a phase frequency detector (PFD), along with a signal from an oscillator set to half the desired phase lock offset frequency. The PFD then measures the phase and frequency difference between the two signals and produces two error signals, one fast one slow, which are fed into a PID controller. The fast error signal is used to feed back to an inter-cavity EOM to control the Apprentice phase, and the slow error signal is fed back to the cavity actuator to control the Apprentice frequency.

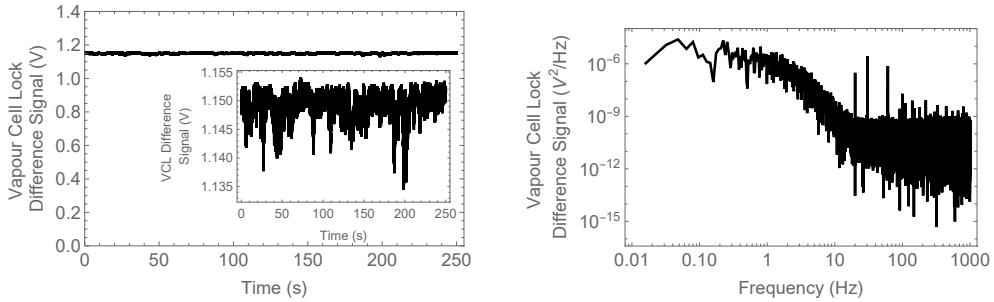
4.2.2.2 Phase Lock

Variations in phase between the Master and Apprentice beams during an interferometry pulse will be imprinted onto the atomic wavepacket, and contribute to the system error. This phase variation is minimised by "phase-locking" the Master and Apprentice lasers together. Figure 4.6 shows a diagram of the phase locking system used to reference the Apprentice laser frequency and phase. The Master and Apprentice beams are combined with a polarising beamsplitter (PBS) so that the two beams have orthogonal polarisations. A half waveplate then rotates the beam polarisations, which allows the power ratio of the two beams to be controlled as they pass through a second PBS. The transmitted beams, now with both Master and Apprentice beams having the same, linear polarisation, are coupled into the same optical fibre, creating a beat note. Figure 4.4 shows this in the "Phase Lock Beat Note". The beat note is an optical signal with a frequency modulated by the sum and the difference of the Master and Apprentice beam frequencies. The modulated beam is converted into an electrical signal using a high speed detector. The high "summed" frequency is too high to be detected, so only the "difference" signal remains. This signal passes through a phase shifter, which allows an analog voltage to change the phase of the beat signal by up to 2π. The frequency is then divided by two before being fed into a phase

frequency detector (PFD), along with a signal from a reference oscillator set to half the desired Master-Apprentice frequency offset. The PFD mixes the oscillator and beat note signals and removes the summed frequency to give the "mixed phase-lock beat signal", MPLB, which is accessible by the user. The PFD outputs two error signals, one fast and one slow. The slow error signal is dependent on the frequency difference between the phase shifted beat note and the oscillator, and the fast error signal is dependent on the phase difference between the two. After each error signal is sent to separate PID circuits, the outputs are fed back into the Apprentice laser. The slow signal is fed to the Apprentice cavity actuator, which alters the Apprentice frequency, to keep it at twice the oscillator frequency from the Master laser. The fast error signal is fed into an inter-cavity EOM, which alters the output laser phase, to keep the Apprentice at a constant phase from the Master laser, set by the value of the phase shifter [62].

4.2.3 Laser and Lock Stability

4.2.3.1 Vapour-Cell Lock Photodiode Difference Signal



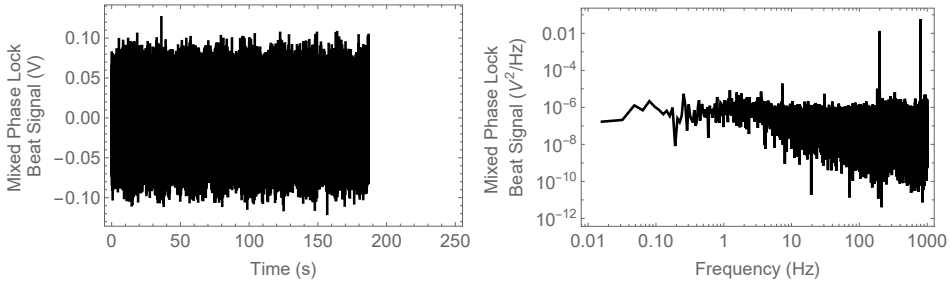
(a) (b)

Figure 4.7: Typical vapour cell lock difference signal time series (a) and power spectrum (b) data taken in the laboratory. As the Master laser varies in frequency, the value of the photodiode difference signal from the saturated absorption spectroscopy system in the vapour cell lock will move away from the centre of the locking peak, causing a change in this signal.

If the Master laser varies in frequency, the vapour cell lock EOM sideband will drift away from the peak of the spectral feature used as a frequency reference. This will cause a decrease in the photodiode difference signal as the sideband moves from the peak to the side of the spectral feature. As such, the difference signal can be used to characterise the variation in Master laser frequency. Figure 4.7 shows a typical set of data taken from the vapour cell lock difference signal. The maximum value of around 1.153 V is the maximum

height of the locking peak, and the decreasing signal occurs as the Master laser drifts away from the desired locking frequency. The power spectrum shown in figure 4.7b shows roughly white noise above around 10 Hz, with increasing noise at lower frequencies.

4.2.3.2 Mixed Phase Lock Beat Signal



(a) (b)

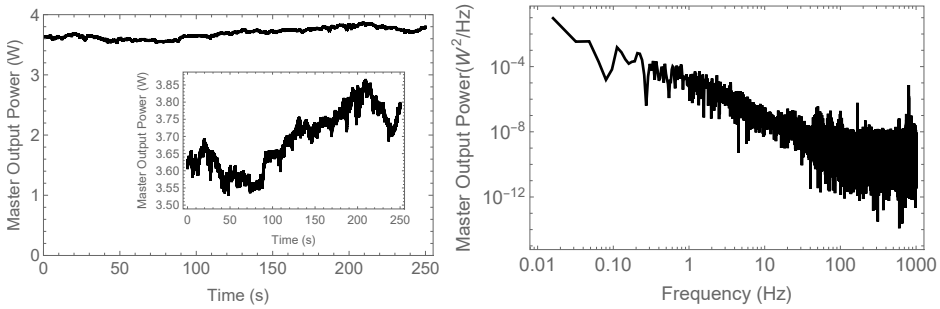
Figure 4.8: Typical MPLB signal time series (a) and power spectrum (b) data taken in the laboratory. As the Master and Apprentice laser drift apart from each other in frequency, the difference between their beat note and the local oscillator frequency will drift away from zero, causing a change in this signal.

Variation of the MPLB signal is caused by the Apprentice laser drifting away in frequency from the Master. This could be caused by either the Master or the Apprentice laser varying in frequency, but it can be used as a measure of the frequency stability of the Raman light in the experiment. Figure 4.8 shows typical time series and power spectrum data from the MPLB taken in the laboratory. The power spectrum in figure 4.8b shows white noise over almost the entire frequency spectrum shown, with two narrow peaks at 170 Hz and 800 Hz.

Future versions of this experiment will incorporate a wavelength meter which can measure the Master and Apprentice laser frequencies explicitly, rather than using the photodiode difference and MPLB signals.

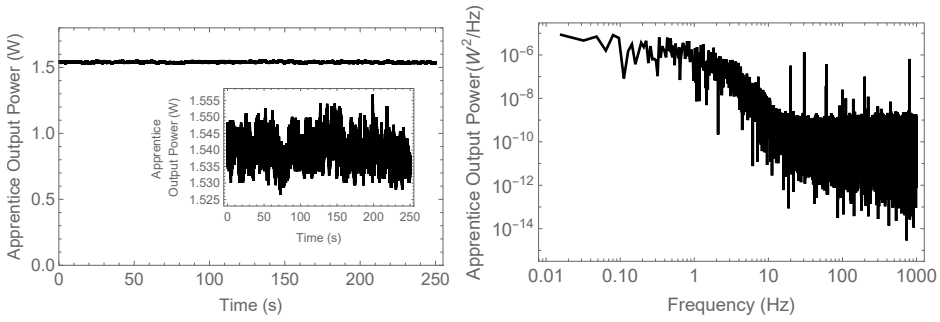
4.2.3.3 Master Output Power

A photodiode at the output of the Master laser is used to measure its power. Time series and power spectrum data for the Master output power are shown in figure 4.9. The Master power seen in figure 4.9a is around 3.7 W. However, while working in the laboratory, depending on the cooling or repumper power requirements for various stages of system optimisation, the pump power splitting ratio was often changed. For example, while investigating the MOT



(a) (b)

Figure 4.9: Typical Master output power time series and power spectrum data taken in the laboratory. The data was measured using a photodiode on the output of the Master laser.



(a) (b)

Figure 4.10: Typical Apprentice output power time series and power spectrum data taken in the laboratory. The data was measured using a photodiode on the output of the Apprentice laser.

loading and molasses cooling, more pump light was directed towards the Master laser and away from the Apprentice, to give the highest 3D MOT atom number. The power spectrum data shown in figure 4.9b shows some low frequency noise, as well as two small peaks around 170 Hz and 800 Hz. Both of these frequencies were seen in the MPLB signal data (figure 4.8b), suggesting that the variation in beat note frequency was caused by a changing input power to the phase lock.

4.2.3.4 Apprentice Output PD

As for the Master laser, a photodiode positioned on the output of the Apprentice is used to measure the laser power. Typical time series data for the Apprentice output PD is shown in figure 4.10a. The power spectrum shows a decrease below around 1 Hz, with roughly white noise above 10 Hz.

4.3 Acousto-Optic Modulators

To control the overall powers and frequencies of the Master, Apprentice and Raman beams independently, each beam is passed through a free space acousto-optic modulator (AOM). While this gives fast control of the power and frequency of all beams in the experiment, in some stages of the experiment, such as the moving molasses, individual beams need to be at different frequencies or powers, and frequencies need to be ramped on a timescale faster than is possible for the laser lock. To give independent control of each beam in the experiment, after passing through the free space AOMs, the Master and Apprentice beams are combined and coupled into the same fibre-coupled AOMs (fibre AOMs). These AOMs apply additional frequency shifts to each individual beam, and can also be used to quickly ramp beam frequencies and amplitudes by ramping the applied radio frequency (rf) signal. Each of the AOMs used in this experiment is described in table 4.1.

AOM	**Central Frequency**	**Configuration**	**Shift**
Cooling	80 MHz	Double	Positive
Apprentice	80 MHz	Single	Negative
Push beam and Excitation	150 MHz	Single	Positive
2D and 3D MOT	135 MHz	Single	Positive
Raman	80 MHz	Double	Negative

Table 4.1: Description of each acousto-optic modulator in the experiment, including the central operating frequency of each, whether they are in single or double-pass configuration, and if they act to increase or decrease the incident light frequency.

4.4 System Electronics

4.4.1 Direct Digital Synthesis (DDS)

In previous versions of this experiment, the rf electrical signal for each AOM was provided by Voltage Controlled Oscillators (VCOs) [42, 43, 44]. However, these devices are extremely sensitive to environmental changes, particularly temperature. As this accelerometer is transportable, it is often subject to significant temperature changes, which means a more stable rf source is required. Instead, a direct digital synthesis (DDS) system is used, with 10 rf output channels. These channels are used to control the cooling, Raman, and

repumper free-space AOMs, as well as the 6 MOT beam fibre-AOMs. The DDS channels can be programmed to provide rf frequencies from 300 kHz to 400 MHz with sub Hz resolution. The AOMs used for the push beam, 2D MOT, and excitation beam do not need to have the agility of the MOT beams, as during the experimental sequence they are always at one frequency. Instead of the DDS, these AOMs are controlled by static signal generators, and are turned on or off with an rf switch.

4.5 System Control Software

4.5.1 MOTMaster and AxelHub

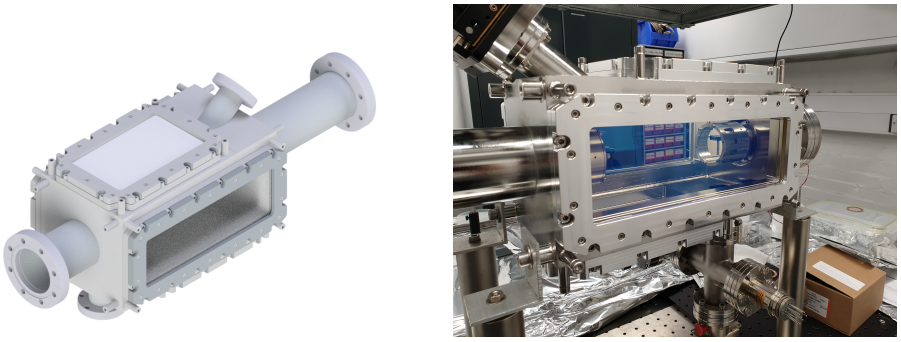
The experiment is run using custom-made control software called MOTMaster, which was developed using the C# language within the Centre for Cold Matter at Imperial College [63]. The software allows the user to define a control sequence, which determines the state of each of three analog and digital acquisition and output cards used to run the experiment. The sequence is split up into a grid, where each column corresponds to a time block of the experiment, and each row corresponds to an analog or digital channel. These settings are saved in internal memory, allowing the sequence to be repeated a desired number of times. Certain parameters can also be left as variables, allowing them to be scanned over several experimental sequences. All time blocks are referenced to an internal clock. Alongside MOTMaster is a data visualisation and acquisition program called AxelHub. AxelHub is linked to both the analog input card, and to the internal clock, to allow real time visualisation of the photodiode and classical accelerometer data from the experiment. Axelhub communicates with MOTMaster, to determine which time blocks correspond to the interferometry and detection sequences, and only displays the relevant time-series accelerometer and photodiode data. As well as plotting the raw data from the photodiode, the signal is averaged and converted into a ratio of atom numbers in each of the atomic states detected. Detailed descriptions of the MOTMaster and Axelhub software can be found in [63].

4.5.2 DDS LabVIEW

Alongside the control software described in section 4.5.1, the DDS used to control the system AOMs has its own software. During this project, a program was created using LabView, which loads the time block durations and names from the MOTMaster sequence, and sets both the rf power and fre-

quency settings for each DDS channel. The program then converts the sequence data into serial code, which is sent to the DDS via ethernet connection, and a digital trigger controlled by MOTMaster starts the sequence. To more easily control the experiment, a version of this software is currently being created within MOTMaster, which will allow all of the experimental control to be performed from the same user interface. However, this is still in progress and has not been used during this experiment.

4.6 Science Chamber



(a) (b)

Figure 4.11: (a) 3D CAD model of the science chamber (b) Photograph of the science chamber, before external optics and coils were attached. The large windows are sealed in a sandwich between two pieces of aluminium to improve robustness.

Figure 4.11 shows the utra-high vacuum (UHV) science chamber where the interferometer is housed. The science chamber has a cubic shape to make it easier to mount in a 19-inch rack, and to improve the overall packing density of the demonstrator. The body is made from 316LN low-magnetisation steel. Four indium sealed windows provide optical access for cooling, trapping and imaging beams. Two DN63 flanges are used to mount the Raman telescope and mirror, which will be described in section 4.8. The 2D MOT atom source is mounted to a DN40 flange on the top of the chamber, at an angle of 36 ° to the horizontal, so that atoms leaving the 2D MOT are aligned with the centre of the 3D MOT trapping region. A second DN40 flange on the bottom of the chamber is used to mount an angle valve, pressure gauge, and ion pump, through a 4-way cross.

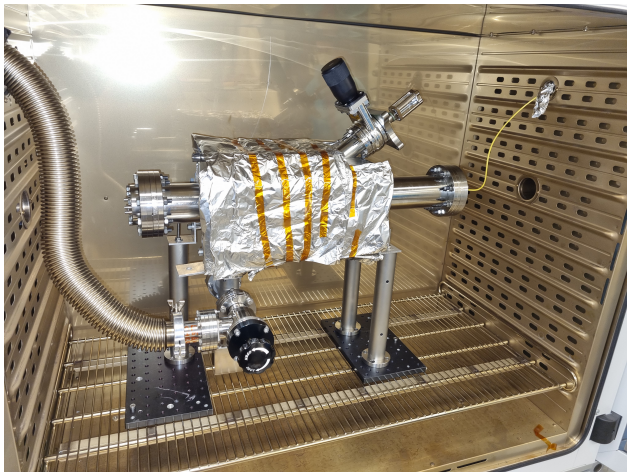


Figure 4.12: Image of the vacuum chamber inside an oven before baking. The foil wrapped around the body of the chamber is to help protect the window.

4.6.1 Achieving UHV

To achieve UHV, the science chamber was cleaned and baked to remove hydrocarbon and water residue remaining from the manufacturing process, which could potentially outgas. The cleaning process involved washing sequentially in detergent (Citranox), deionised water, acetone, deionised water, isoproponol, and deionised water. After cleaning, the open ports were sealed with flanges and a turbo molecular pump was attached. The chamber was then baked in an oven at 80 °C for 10 days. A low temperature, long bake was chosen because of the low melting point of indium, used to seal the large windows. Particular care was taken to avoid large temporal or spatial temperature gradients in the windows, which due to their size can be prone to cracking under thermal stress. Figure 4.12 shows the chamber inside the oven prior to baking. The oven provided a uniform heat source and enabled the heating and cooling rate to be controlled at $< 1\,\mathrm{K/min}$. After baking, a Helium leak detector revealed a $10^{-6}\,\mathrm{mbar\,L\,s^{-1}}$ leak from the indium sealed windows. After extensive investigations, together with the manufacturer, it was concluded that thermal fatigue of the indium wire, caused by multiple bakes[1], was the cause of the leak. An alternative sealing method, using gold wire seals instead of indium has been proposed and will be tested in a future experiment. After replacing the fatigued indium seals the chamber was leak checked again, and no leak $> 10^{-11}\,\mathrm{mbar\,L\,s^{-1}}$ was observed. The chamber was then re-cleaned and pumped down to a pressure of $10^{-7}\,\mathrm{mbar}$ using a

[1]The indium sealed windows were baked more than once by the manufacturer before assembly of the full science chamber. The precise parameters of these bakes are unknown.

turbo molecular pump without baking. A combination of a $6\,\mathrm{L\,s^{-1}}$ (Ar) ion pump and a passive $200\,\mathrm{L\,s^{-1}}$ (H_2) sublimation pump reduced the pressure to 9×10^{-9} mbar, before the angle valve was closed and the turbo pump was removed.

During interferometry, collisions with background gas causes decoherence of the interferometer [64], reducing contrast. The rate at which these collisions occur, neglecting intra-cloud collision [65] can be approximated as $R_\mathrm{c} = n_\mathrm{b}\sigma v_\mathrm{p}$, where n_b is the number density of background atoms, σ is the cross section of the cloud-background gas collision, and v_p is the peak of the velocity disribution of background gas [66]. If the assumption of an ideal background gas is made, then the collision rate becomes

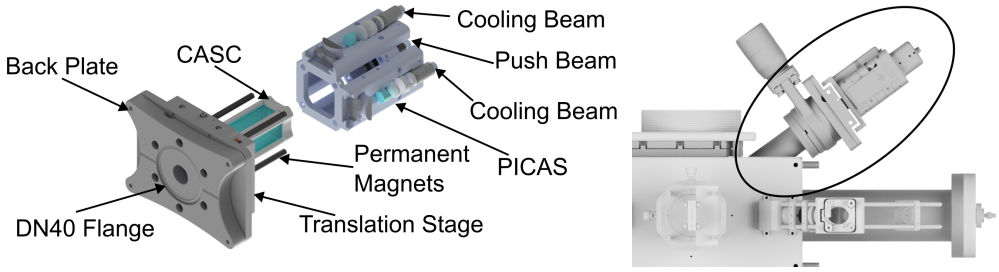
$$R_\mathrm{c} = \frac{1}{\tau} = \frac{P\sigma v_\mathrm{p}}{k_\mathrm{B}T}, \tag{4.1}$$

where τ is the average time between collisions, P is the background pressure, k_B is the Boltzmann constant, and T is the background gas temperature. At low pressures, it is a good assumption that the background gas consists only of hydrogen at room temperature [67], the most probable speed, $v_p \approx 1600\,\mathrm{m\,s^{-1}}$, and the collisional cross section between ^{87}Rb and H_2 is $2.95 \times 10^{-18}\,\mathrm{m^2}$ [68]. For collisional dephasing to be negligible, the average time between collisions, $\tau \gg 2\mathrm{T}$, where T is the interferometer time. For a pressure of 9×10^{-9} mbar, the average time between collisions with background gas will be around 975 ms, or around 50 times the anticipated interferometer 2T-time. This base pressure is about a factor of 10 larger than my aim, and may negatively impact the interferometer performance for large T-time interferometry through collisional dephasing. Future baking of the system once the improved seals have been tested will remove this potential issue.

4.7 Ex-vacuo Hardware

4.7.1 Atom Source and 2D MOT

Figure 4.13a shows a 3D CAD model for the 2D MOT cold atom source, which includes a UHV glass cell (CASC) containing a rubidium getter source together with a 3D printed Photonically Integrated Cold Atom Source (PICAS, circled in figure 4.13b), both commercially available [69]. The CASC is pumped down to UHV together with the science chamber via a 1 mm aperture. The low conductance of atoms through this aperture is necessary so

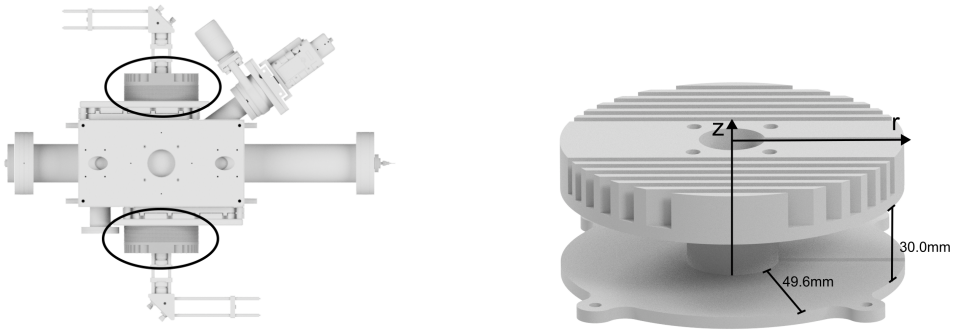


(a) (b)

Figure 4.13: (a) Source cell (CASC) and Photonically Integrated Cold Atom Source (PICAS). The back plate attaches to a gate valve, which is in turn connected the science chamber. A translation stage attached to the permanent magnet rods allows the zero of the field gradient to be aligned to the CASC aperture. (b) CAD design showing the mounting of the CASC and PICAS (circled) to the science chamber.

that a high pressure can be maintained within the CASC without significantly raising the pressure in the science chamber. Rubidium atoms are released into the CASC through the Ohmic heating of the getter. Typically $\sim 3\,\mathrm{A}$ of current running through the dispensers provides a large enough rubidium density to efficiently load our 3D MOT from the 2D+ MOT source. The PICAS houses the optics and magnets required by the 2D+ MOT, and plugs directly onto the CASC. Three fibre inputs deliver cooling and repumper light for transverse cooling, and near resonant light for the push beam.

4.7.1.1 3D MOT Coils

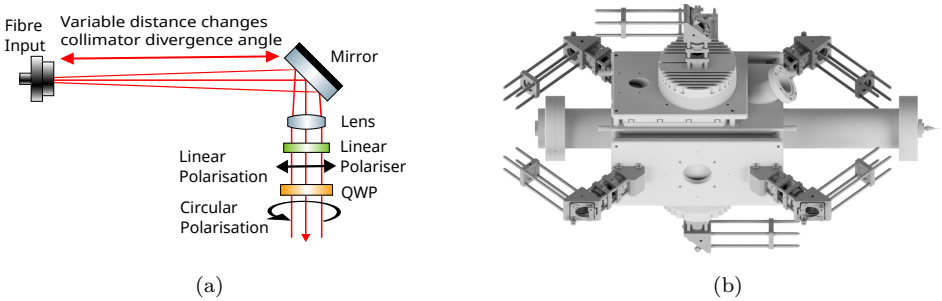


(a) (b)

Figure 4.14: (a) CAD design showing the mounting of the 3D MOT coils (circled) to the main science chamber. The coils attach to a metal plate secured to the chamber via four bosses on each corner. (b) Dimensions of the MOT coil formers.

The spherical quadrupole magnetic field for the 3D MOT is produced using a pair of coils close to the anti-Helmholtz arrangement. Figure 4.14 shows a 3D CAD model of the coils and how they are mounted to the science chamber, together with the dimensions of the coils formers. Each coil contains 34 radial turns and 27 axial turns of polyamide coated copper wire. A square cross-section is used to provide a tight packing density, and help conduct heat away from the coils. An inductance metre was used to measure the coil inductance of 9.44 mH, and the resistance of the coil was calculated from $R = \rho L/A$ to be 4 Ω. Here, ρ is the resistivity of copper, L is the total length of the wire coil, and A is the wire cross-sectional area.

4.7.1.2 3D MOT Optics



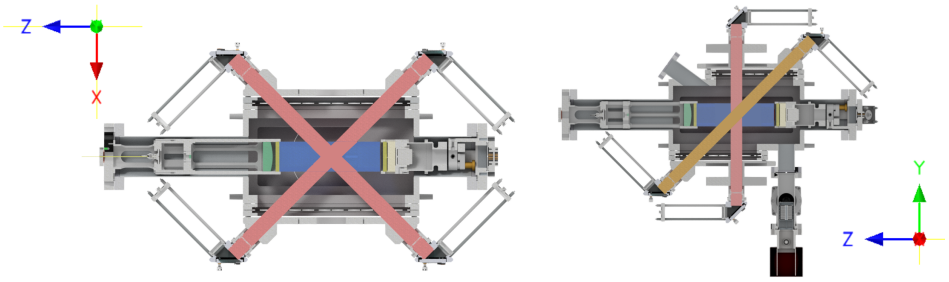
(a) (b)

Figure 4.15: (a) The optics used in the 3D MOT collimators. The linear polariser converts any polarisation drift into power drift, which will be corrected with a power stabilisation system in future versions of the experiment. The polarisations before and after the quarter waveplate are also shown. (b) 3D CAD design of the 3D MOT collimators. Cage rods allow the fibre input plate position to be varied during collimation. Rotation mounts allow both the linear polariser and quarter waveplate to be properly aligned to give circularly polarised output light.

The trapping light for the 3D MOT and molasses is delivered to the science chamber through six one inch, circularly polarised, collimated beams. Figure 4.15a shows how light is expanded from the optical fibre output of one of the fibre AOMs. Light leaving the fibre input plate expands, is reflected at a mirror, before being collimated with a lens to give a $1/e^2$ radius of 10 mm. A linear polariser after the lens filters the polarisation, projecting any polarisation variation into power variation[2]. A quarter waveplate creates circularly polarised light at the output.

[2]As a result of my work, an active intensity stabilisation system has been developed, but will not be described in this thesis.

Figure 4.15b shows a 3D CAD design of the collimators mounted to the science chamber. The vertical collimators are mounted to the centre of the MOT coils. The horizontal collimators are secured to metal side-plates using angled sections, which ensure light from each collimator roughly overlaps at the centre of the chamber, where the magnetic field from the MOT coils is close to zero. The angled sections allow the collimators to be remounted without significant realignment. The paths of the MOT beams are shown in red in figure 4.16.



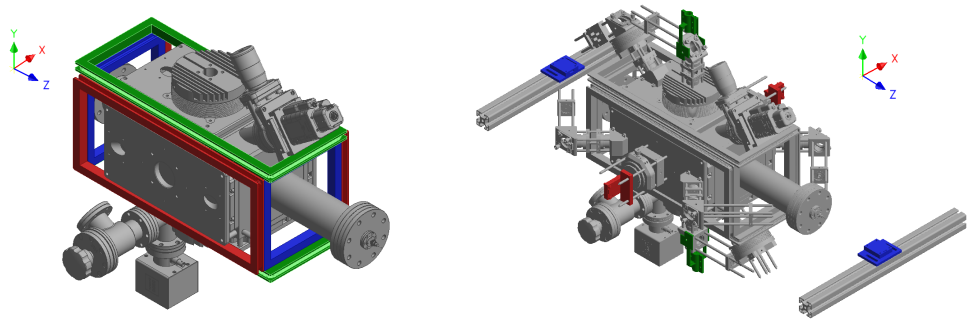
(a) (b)

Figure 4.16: (a) Top-down cut-through of the CAD design for the science chamber. The blue beam shows the Raman beam path. The red beams show the MOT beam paths. (b) Side cut-through of the CAD design for the science chamber. The blue and red beams are as in (a) and the orange beam is the excitation beam path.

4.7.2 Bias Magnetic Fields and Magnetic Field Compensation

During state preparation, interferometry, and detection, bias magnetic fields are used to align the magnetic dipoles of the atoms. These fields define quantisation axes for the atomic transitions taking place during each experimental step. Figure 4.17a shows the positions of three pairs of "bias" coils, close to Helmholtz configuration which are used to create these magnetic fields. Each coil contains forty turns of 0.7 mm diameter polyamide coated copper wire, with dimensions as shown in table 4.2. The magnetic field at the centre of the science chamber for each pair of coils is: $B_x = 1.57\,G\,A^{-1}$, $B_y = 1.61\,G\,A^{-1}$, and $B_z = 0.28\,G\,A^{-1}$.

As well as applying bias fields during the experiment, these coils are used to cancel both static, and time-varying background magnetic fields. When the experiment is stationary, the magnetic field at the atom position can be zeroed by manually varying the coil currents to minimise the atom cloud



(a) (b)

Figure 4.17: (a) 3D CAD design showing the position of each pair of bias coils. (b) 3D CAD design showing the position of the flux-gate magnetometers used to estimate the background magnetic field at the atom position.

Coil	**Colour in figure 4.17a**	**Dimensions (mm × mm)**	**Axial distance from atoms (mm)**
X	Red	450 x 158	100
Y	Green	420 x 162	100
Z	Blue	158 x 162	225

Table 4.2: Size and distance of each pair of bias coils used in the experiment from the atom position.

temperature. These "static compensation fields" cancel out any background magnetic fields, for example due to the Earth's field. However, when the experiment moves, the atoms will experience a time-varying magnetic field which will no longer be cancelled by the static compensation fields.

Figure 4.17b shows pairs of flux-gate magnetometers corresponding to each set of bias coils. Two sensors are placed outside of the science chamber, along each axis, and by averaging the two magnetic field values, the magnetic field at the atom position can be estimated. This makes the assumption that the magnetic field between the two sensors is approximately linear, as shown by the red line in figure 4.18. However, if the field curves between the the two sensors, an error in the predicted magnetic field will occur, as seen by the blue line in figure 4.18. During field trials, it is assumed that the experiment should be far from any magnetic dipoles, so any background fields should be fairly uniform, and this compensation error should be small. However, to test if this assumption is valid, multiple magnetometers would need to be placed along each experimental axis, to increase the complexity of the shape of magnetic field which could be detected using this system. To

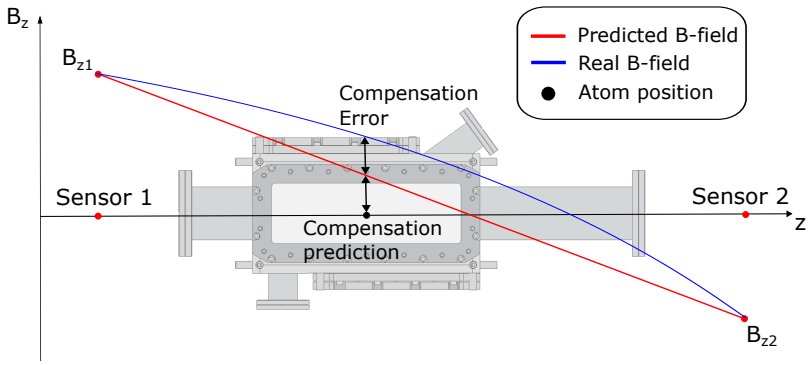


Figure 4.18: Description of how magnetic field curvature in the experiment will cause errors in the compensation system. This could be solved by adding more flux gates along each axis of the experiment.

compensate for time varying magnetic fields, the compensation system functions in a "sample and hold" configuration, where the flux gates record the magnetic field for 100 ms before each experimental sequence. The readings are fed into a microprocessor, which estimates the magnetic field strength at the centre of the science chamber, and calculates the current required to cancel the field. The coil current is then held at a constant value throughout the experimental sequence. This system works on the assumption that background magnetic fields will vary more slowly than the repetition rate of the experiment, around 1 Hz. In the future, the system will be upgraded to repeatedly cancel the background magnetic fields throughout the sequence and give higher bandwidth magnetic field compensation. The details of this system, as well as the magnetic field shape during field trials, will be discussed in more detail in a future PhD thesis.

4.7.3 Microwave Horn

Figure 4.19 shows the position of the microwave horn waveguide used to deliver microwaves into the science chamber during state preparation. The horn is mounted on 6 cm cage mounts, which allow the horn to be moved towards and away from the science chamber, to maximise the microwave transfer efficiency. To align the atoms' magnetic dipole during the microwave transition, the bias coils along the y direction are used to apply a magnetic field perpendicular to the microwave magnetic field.

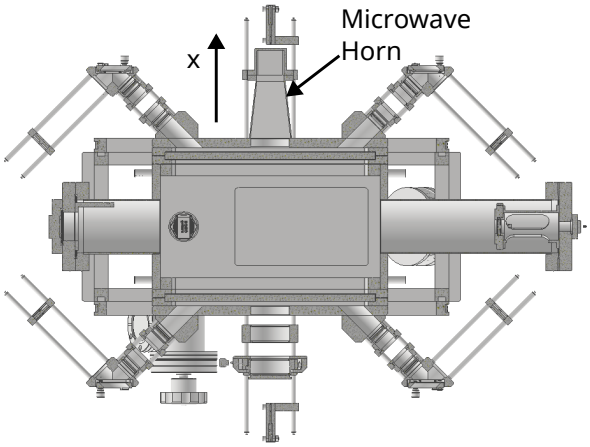
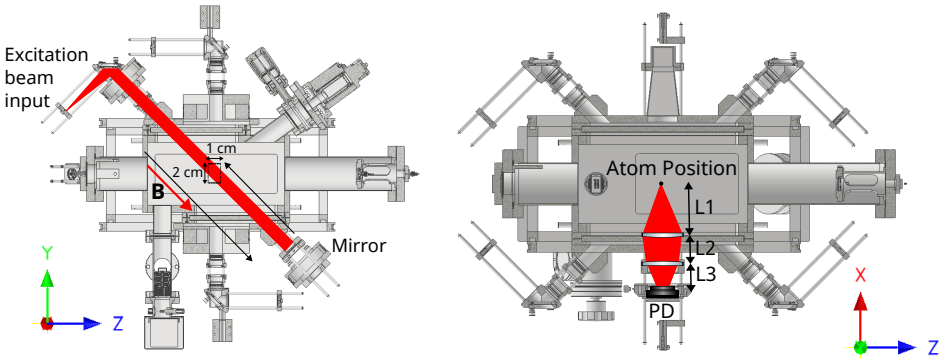


Figure 4.19: CAD design of the vacuum chamber showing the microwave horn position. The horn can be moved along the x direction on cage rods to maximise the microwave transfer efficiency.

4.7.4 State Sensitive Detection

4.7.4.1 Detection Apparatus



(a) (b)

Figure 4.20: (a) Side cut-through of the science chamber showing the excitation beam path (red) as well as the imaging region where the photodiode is positioned. (b) Top-down cut-through of the science chamber showing the path of the scattered detection beam light through two imaging lenses and into the photodiode.

After the interferometry sequence, the read-out of the atomic energy states is performed using fluorescence detection [70]. Light for fluorescence detection, known as the excitation beam, is delivered into the science chamber using a collimator identical to the 3D MOT collimators described in section 4.7.1.2, angled at 45 ° to the horizontal. Figure 4.20a shows the path of the

excitation beam through the science chamber, before being retro-reflected back towards the detection region, which is also pictured. The result of this retro-reflection is two counter-propagating beams, with opposite-handed circular polarisations. After the atoms are excited, they fluoresce light over 4π sr. Figure 4.20b shows the position of a 50 mm diameter lens which collects around 1.5% of the emitted light from the atoms. The distance from the science chamber centre to the collection lens is 100 mm. A second 50 mm diameter lens is placed 25 mm away, which focuses the light down onto a photodiode positioned another 30 mm away from the chamber. The photodiode has an active area of 1 cm × 2 cm, and is mounted on a translation stage which allows movement up to 2 mm along both the y and z directions.

4.7.4.2 Photodiode Signal to Atom Number

Fluorescence detection involves exciting atoms in a particular state before detecting the number of spontaneously emitted photons with a photodiode. By converting the photodiode signal to an atom number, the number of atoms in a given state can be determined. For light of intensity I, with detuning δ from a detection transition with natural linewidth Γ and saturation intensity I_{sat}, the photon emission rate is given by

$$\begin{aligned} R_{\text{em}} &= \frac{\Gamma}{2} \frac{\frac{I}{I_{\text{sat}}}}{1 + 4\left(\frac{\omega_{\text{L}} - \omega_0}{\Gamma}\right)^2 + \frac{I}{I_{\text{sat}}}} \\ &= \frac{\Gamma}{2} \frac{s_0}{1 + 4\left(\frac{\omega_{\text{L}} - \omega_0}{\Gamma}\right)^2 + s_0}, \end{aligned} \tag{4.2}$$

where s_0 is the "saturation parameter". For the $|F = 2\rangle \rightarrow |F' = 3\rangle$ transition in ^{87}Rb, which is used in this experiment, $\Gamma = 2\pi \times 6.065\,\text{MHz}$, and $I_{sat} = 1.669\,\text{mW/cm}^2$ [58]. For each photon detected by a photodiode, the voltage signal will be

$$\begin{aligned} V_{\text{photon}} &= E A_{\text{PD}} \\ &= E R_{\text{PD}} A_{\text{VA}}, \end{aligned} \tag{4.3}$$

where $E = hc/\lambda$ is the energy of each photon, R_{PD} is the responsivity of the photodiode with units of A W^{-1} ($0.58\,\text{A W}^{-1}$ for a silicon detector and 780 nm light), A_{VA} is the photodiode gain in V A^{-1}, and A_{PD} is the overall photodiode gain in units of V W^{-1}. For a collection efficiency, $\eta = 0.015$, the total atom number is then

$$N_{\text{atom}} = \frac{V_{\text{PD}}}{\eta E A_{\text{PD}} R_{\text{em}}}. \tag{4.4}$$

For the detection system used in this experiment, this gives an atom number of $3.16 \times 10^8\,\text{V}^{-1}$.

4.7.4.3 Detection Sequence

The first stage of detection uses a 400 µs light pulse, which is −1 MHz detuned from the $|F = 2\rangle \rightarrow |F' = 3\rangle$ transition. Initially, the detection scheme used light resonant with the detection transition, as this gave the largest number of emitted photons, and therefore the lowest detection noise. However, as this system is subject to vibrations during moving field trials, it was empirically found that, over time, the excitation beam would become slightly misaligned. When the detection light was resonant, any misalignment or power imbalance in the excitation beam caused the atoms to be blown out of the detection region, giving a decaying detection signal. By slightly red detuning the beams, it was found that the effect of beam misalignment was reduced to a negligible level for small excitation beam misalignment. The reduction in photon emission rate due to the detuning was considered acceptable in order to prevent atoms being blown away during detection. During the detection sequence, the z and y bias coil pairs apply a magnetic field along the excitation beam axis. The polarisations of the incoming and retro-reflected beams are set such that, in the presence of this uniform magnetic field, both beams drive σ^+ transitions. After the interferometer pulses, atoms will be in either of the $|F = 2, m_F = 0\rangle$ or $|F = 1, m_F = 0\rangle$ states. For now, just consider those in $|F = 2, m_F = 0\rangle$. When the excitation beam is turned on, atoms will absorb a photon and be excited to $|F' = 3\rangle$. They will then spontaneously emit a photon and decay back to $|F = 2\rangle$. The emitted photons can be collected with a photodiode, and the output voltage V_{PD} can be converted into an atom number using equation (4.4). This allows N_2, the number of atoms in $|F = 2\rangle$, to be measured[3]. After measuring N_2, a 200 µs pause is followed by a second pulse of 400 µs from the excitation beam. The second pulse contains both excitation light and a second "repumper" beam, which is resonant with the $|F = 1\rangle \rightarrow |F' = 2\rangle$ transition. The repumper light drives any atoms in $|F = 1\rangle$ into $|F = 2\rangle$ where the excitation light causes them to fluoresce, just as in the N_2 measurement. This gives a measure of the total number of atoms in the system, N_{Tot}. By subtracting N_2 from N_{Tot}, the number of atoms which were in $|F = 1\rangle$, N_1, can be calculated. After these two measurements, one vertical and one horizontal MOT beam, blue-detuned from

[3] N_2 is not to be confused with diatomic Nitrogen, and during this thesis always refers to the atom number measured in the $|F = 2\rangle$ energy level.

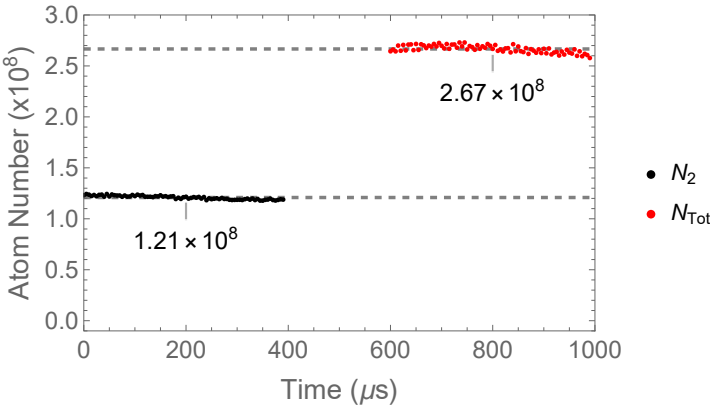


Figure 4.21: A typical measurement of atom number using the fluorescence detection scheme. The two stages measure, N_2 (black), the number of atoms in the $|F = 2\rangle$ ground state and N_{Tot} (red), the total number of atoms. The grid lines and markers show the mean atom number of the black and red data.

the $|F = 2\rangle \rightarrow |F' = 3\rangle$ transition, are used to push all of the atoms out of the field of view of the detection apparatus. The two detection pulses are then repeated, to give measurements of the background light during detection, B_2 and B_{Tot}. These are then subtracted from N_2 and N_{Tot} to give a ratio of atoms in $|F = 2\rangle$ to the total number of atoms,

$$P_2 = \frac{N_2 - B_2}{N_{Tot} - B_{Tot}}. \tag{4.5}$$

Figure 4.21 shows a typical photodiode signal, converted to atom number, taken during a detection sequence. The black data shows the N_2 measurement, while the red data shows the N_{Tot} measurement. The choice of excitation beam polarisation is made to prevent atoms from leaving the $|F = 2\rangle \rightarrow |F' = 3\rangle$ cycling transition. Figure 4.22a shows the effect of using the two vertical MOT beams, instead of the excitation beam, during detection. In the presence of a uniform magnetic field, the MOT beams drive both σ^+ and σ^- transitions. During the N_2 measurement, there is significant decay of the $|F' = 2\rangle$ population. This decay makes the N_2 value difficult to calculate. The decay is due to off-resonant scattering of the detection light driving atoms into $|F' = 2\rangle$, where they can decay into $|F = 1\rangle$. To describe why this effect is not seen for the σ^+/σ^+ transitions in the excitation beam, consider an atom in the $|F = 2, m_F = 0\rangle$ energy level. After making a σ^+ transition, it will be excited to $|F' = 3, m_F = +1\rangle$, and can decay to $|F = 2, m_F = (0, +1, +2)\rangle$. Over a number of absorption/spontaneous emission cycles, the atom will be driven towards the higher m_F states, due to always being excited in a σ^+ transition. Eventually, all atoms will be driven

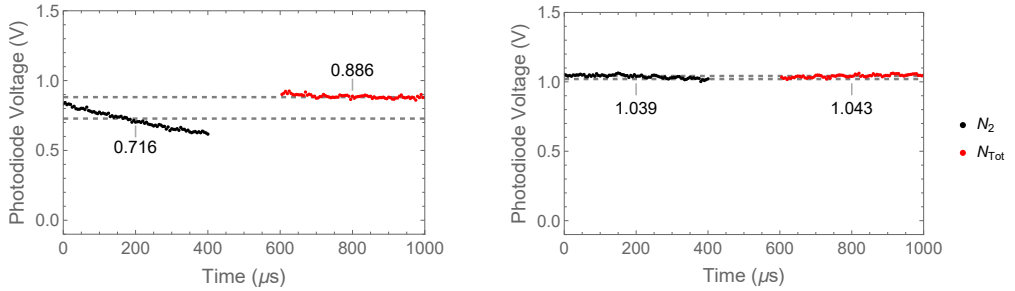


Figure 4.22: Photodiode signal used to measure atom number during fluorescence detection using (a) two vertical MOT beams, and (b) the excitation beam. Both MOT beams and excitation beam were -1 MHz detuned from the $|F = 2\rangle \rightarrow |F' = 3\rangle$ transition. The total MOT beam power was 50 mW and the total excitation beam power was 30 mW. For each dataset the 3D MOT atom number was the same to within 2%. The grid lines show the mean photodiode voltages of the black and red data.

into the $|F = 2, m_F = +2\rangle$ level. When absorbing a photon and being excited to $|F' = 3, m_F = 3\rangle$, an atom can only decay back into $|F = 2, m_F = 2\rangle$, meaning atoms are trapped in this cycle. Because atoms in $|F = 2, m_F = 2\rangle$ cannot absorb a σ^+ photon and be excited to $|F' = 2\rangle$, there is no longer any off-resonant scattering, and atoms cannot decay to $|F = 1\rangle$. This removes the decay during the N_2 measurement, and makes the $|F = 2\rangle$ population much easier to calculate. Figure 4.22b shows an equivalent detection signal to figure 4.22a taken with the excitation beam. This shows no decay in population during the N_2 measurement.

Another benefit of using the excitation beam over the MOT beams is seen in the photodiode voltages in figure 4.22. The two datasets were taken within a few minutes of each other, and the total atom number in the 3D MOT was constant to within 2%. This suggests that for both figures, the atom number during detection should be roughly the same. Despite this, there is a 15% increase in the N_{Tot} photodiode voltage for the excitation beam compared to the MOT beams. From figure 4.23, it can be seen that the $|F = 2, m_F = 2\rangle \rightarrow |F' = 3, m_{F'} = 3\rangle$ transition has the largest transition strength. For the MOT beams, all possible transitions can take place, reducing the average transition strength compared to the cycling transition. For a transition of Rabi frequency Ω and natural linewidth Γ, the saturation parameter s_0 can be written as [71]

$$s_0 = \frac{I}{I_{sat}} = 2\frac{|\Omega|^2}{\Gamma^2}. \tag{4.6}$$

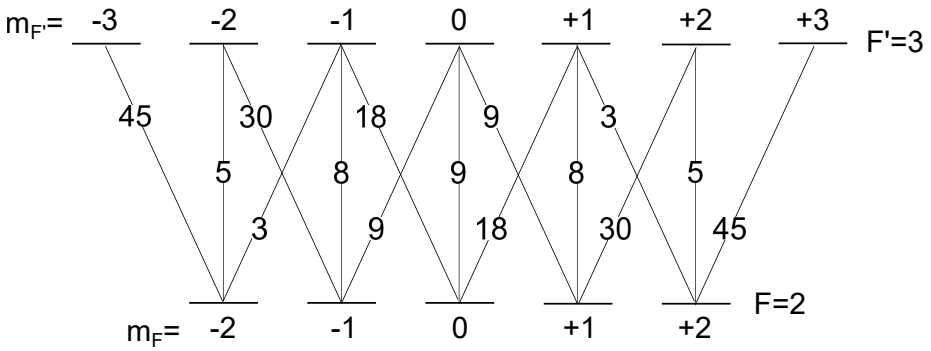


Figure 4.23: Transition strengths for all possible transitions between $|F = 2\rangle$ and $|F' = 3\rangle$. Each strength is normalised such that the weakest transition is an integer. (Figure based on [71]).

As the Rabi frequency is proportional to the transition strength, it can be seen from equation (4.2) that the larger the transition strength, the larger the photon emission rate. This in turn means that atoms in the cycling transition will emit the most photons and will give the largest signal to noise ratio during detection. So the excitation beam both prevents atom loss to $|F = 1\rangle$ during the N_2 measurement, and maximises the number of photons emitted during detection, minimising detection noise.

4.8 In-vacuo Hardware

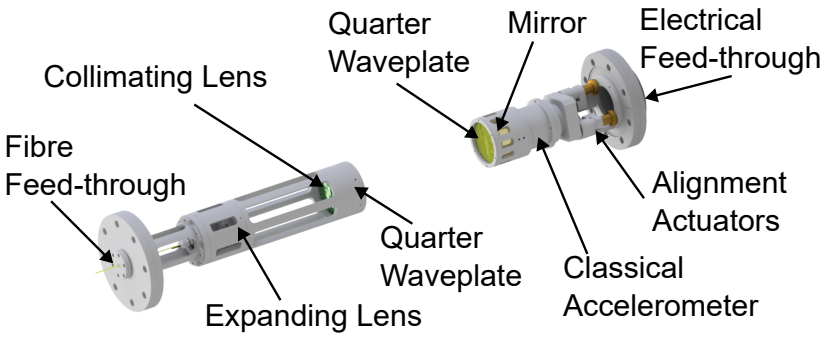


Figure 4.24: 3D CAD drawing of the in-vacuo Raman telescope and mirror with labelled parts.

Inhomogeneities in the Raman beam phase will be imprinted onto the atomic wavepacket as the cloud falls through the Raman beam under gravity [72, 73, 74]. To prevent the curvature of vacuum-sealed windows from inducing phase changes across the Raman beam, both the Raman telescope and mirror are

sealed inside the vacuum chamber. Figure 4.24 shows a labelled 3D CAD design of both the telescope and mirror, including a fibre feed-through for delivering Raman light into the science chamber, and an electrical feed-through to power and acquire signals from a classical accelerometer mounted to the back of the mirror. By delivering light into the science chamber in a feed-through, the optical fibre acts as a spatial filter for the light, reducing phase aberrations of the Raman beam. Both Master and Apprentice beams enter the science chamber in the same optical fibre, with orthogonal polarisations.

4.8.1 Raman Telescope

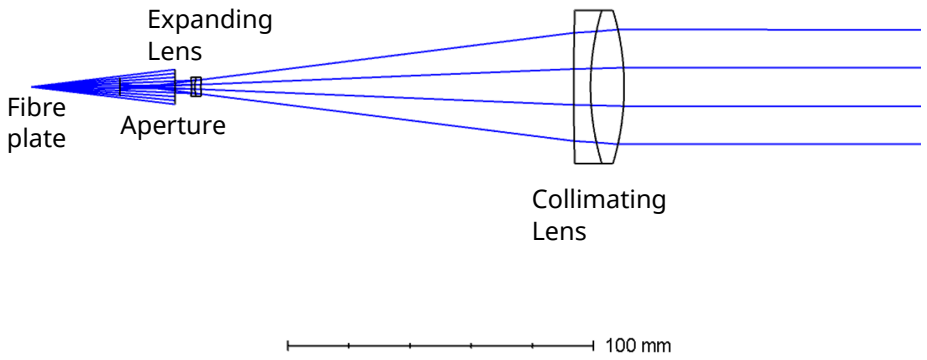


Figure 4.25: Ray tracing diagram showing the beam paths through the Raman telescope.

Figure 4.25 shows a ray tracing diagram of the path of the light through the Raman telescope. Light is delivered to the telescope in a polarisation maintaining (PM) fibre, before expanding up towards an aperture. The aperture truncates the beam, to remove the tails of the Gaussian intensity distribution. As only the central region of the beam will interact with the atoms, the edges of the beam could reflect inside the science chamber, and form "hotspots" of intensity in the Raman beam, as described in [42]. Truncation slightly alters the intensity distribution of the central region of the beam, but it can be well approximated with a parabolic beam shape [75]. Afterwards, the truncated beam propagates towards a 5 mm diameter lens, which further expands the beam. A 50 mm lens then collimates the beam. Without truncation, the Raman telescope beam would have a $1/e^2$ width of 6 cm. The light then passes through a quarter waveplate, which converts linearly polarised light to circularly polarised light. Beneath both the fibre input plate and the 50 mm collimating lens are several "spacer rings" which are used to very finely adjust the distances between each of the lenses. By adjusting the lens

distances, the divergence angle of the Raman beam is changed, in order to collimate the telescope.

4.8.2 Raman Mirror and Classical Accelerometer

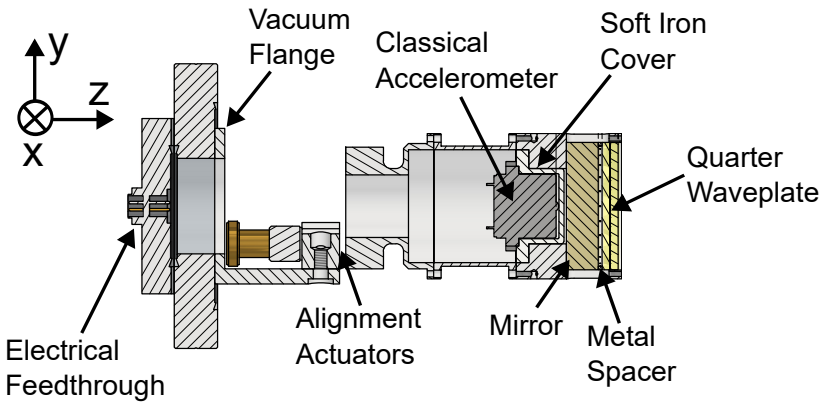


Figure 4.26: CAD design of the Raman mirror with each part labelled.

Figure 4.26 shows a diagram of the in-vacuum mirror mount for the Raman beam retro-reflecting mirror. Mounted to the back of the mirror is a classical accelerometer. This will later be used to track the vibrations of the Raman mirror to cancel out their effects. The accelerometer contains a magnet, so is encased by a soft-iron cover, to redirect magnetic field lines away from the

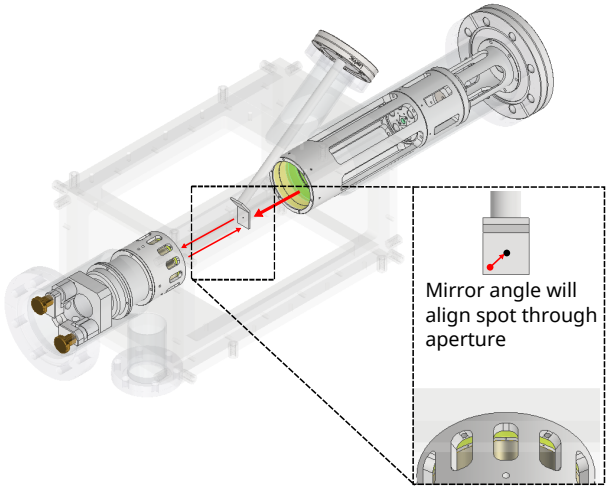
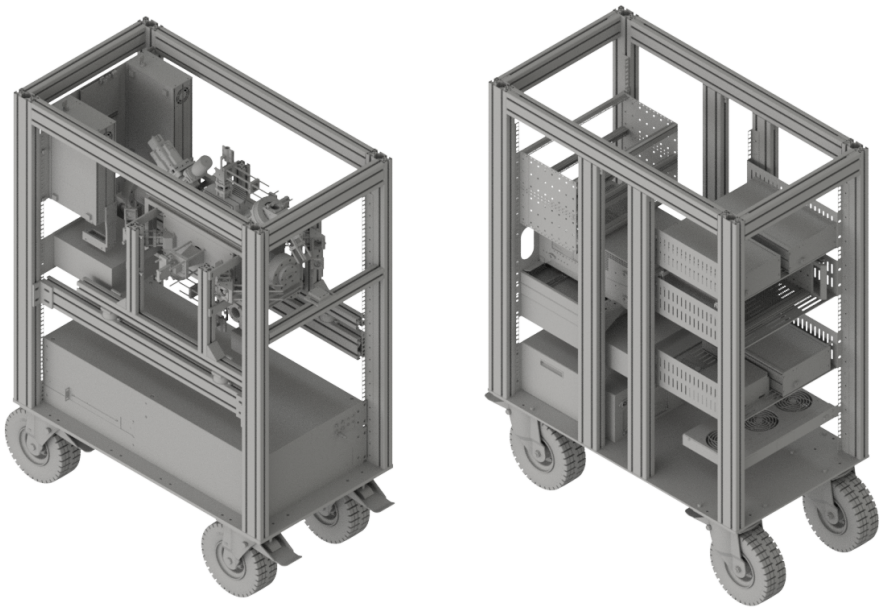


Figure 4.27: The method used to align the Raman mirror. An aperture was placed in the Raman beam and the mirror actuators were used to align the spot back through the aperture to give a limit on the angular deviation of the mirror.

atom position. The mount for the optics and accelerometer is attached to an actuator-controlled tilting mirror mount. The mount can be rotated in both x and y, with finger screws as well as two piezoelectric actuators. The back section of the mirror mount is attached to a flange, which is used to seal the mount inside the vacuum chamber. The flange contains an electrical feed-through with connections for the actuator control cables, as well as power, temperature output and acceleration output signals from the accelerometer.

The method of Raman mirror alignment is shown in figure 4.27. A metal plate with a 1 mm diameter aperture was placed into the science chamber such that the aperture was in the centre of the Raman beam, 8.8 cm away from the Raman mirror. As light was shone through the Raman telescope, light which passed through the aperture was reflected back onto the metal plate containing the aperture. By moving the thumb screws on the Raman mirror, the spot was aligned back through the aperture. This limited the mirror misalignment to a maximum angle of 0.3 °, or 5.2 mrad. This gives a measurement accuracy $\Delta a/a \approx 3 \times 10^{-5}$.



(a) (b)

Figure 4.28: CAD designs showing the racks and mounting of the science chamber and laser system (a), and the system electronics (b). The two boxes are connected by a large "umbilical cord" which transfers electrical and optical signals between the two boxes (not pictured).

4.9 System Mounting and Transportability

To ease transportability, all system electronics, laser system and optics, and the science chamber are housed inside two 19-inch racking systems with wheels, as shown in figure 4.28. The boxes will be referred to as the "electronics box" and the "optical box". The electronics box, including all mounted components, weighs 238 kg and the optical box weighs 277 kg. An "umbilical cable" connects the two boxes to each other to pass electrical and optical signals between the two sides of the experiment. During transport, the umbilical can be removed and each box can be positioned separately. Previous designs had housed the entire experiment in a single racking system. However, this made the box weigh around 500 kg and was over 2 m tall. Despite the wheels, this became very difficult to transport, especially over rough terrain. Another reason for separating the experiment into two parts was to prevent vibrations from the system electronics from causing oscillations of the laser cavity actuators, which would cause the laser to unlock. During operation, the two sides of the experiment are not in physical contact with each other, except via the umbilical, so that vibrations passing from one box to the other are heavily damped and have little effect on the laser lock stability.

Chapter 5

Results

Here I present data taken during characterisation of each stage of the experiment in the laboratory. All data and analysis from field trials will be presented in chapter 6.

5.1 Atom Trapping and Cooling

5.1.1 2D+ MOT

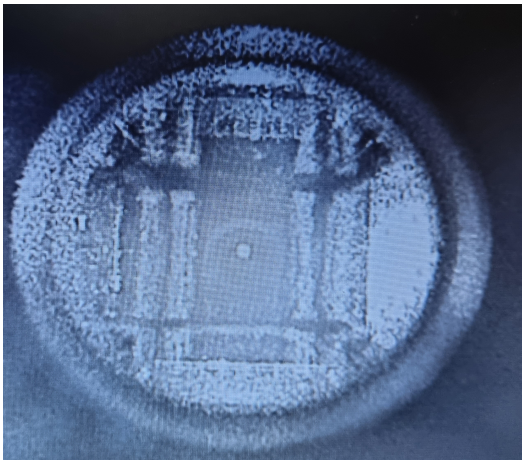
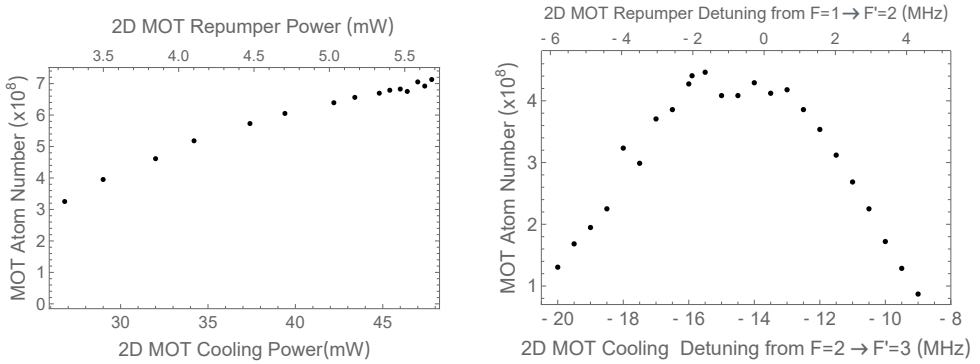


Figure 5.1: A camera image taken down the axis of the PICAS during 2D MOT alignment. The white spot in the centre is fluorescence from the rubidium atoms in the 2D MOT, which were aligned to the cell aperture (not visible) to direct the atomic beam into the main chamber.

When first setting up the 2D MOT system, the atomic beam was not aligned to the CASC aperture, and so no atoms entered the main science chamber. To align the 2D MOT, the plate at the back of the PICAS, which secures

the push beam input, was removed and a camera was directed down the axis of the CASC. By moving the PICAS translation stage, the 2D MOT was aligned to the aperture. Figure 5.1 shows a camera image of the 2D MOT taken after alignment. The white spot in the centre shows the axis of the atomic beam, which was aligned to the aperture, which is not seen in the image. After aligning the atomic beam, atoms were detected in the 3D MOT, and the atom number was used to optimise the 2D+ MOT parameters.



(a) (b)

Figure 5.2: (a) 3D MOT atom number, after 400 ms of loading, with changing 2D MOT beam power. The 3D MOT beam settings were kept constant throughout, but both the cooling and repumper power of the 2D MOT were altered as the rf amplitude to the 2D MOT fibre AOM was changed. (b) 3D MOT atom number, after 400 ms of loading, with changing 2D MOT beam frequency. As for (a), both cooling and repumper light frequencies were changed as the AOM frequency was varied. While varying the AOM frequency, the rf power was changed to maintain a constant optical power throughout the measurement.

Figure 5.2a shows the 3D MOT atom number for varying 2D MOT power. For this data, constant push beam detuning and power of -7.7 MHz and 1.9 mW, constant 2D MOT detuning of -15 MHz and resonant repumper light were used. The 3D MOT atom number does not reach a turning point within this power range, so more 2D MOT cooling power would increase the atom number further. Figure 5.2b shows a plot of 3D MOT atom number against 2D MOT detuning at a constant 2D MOT cooling beam power of 30 mW. The power was reduced to this level, despite it not being the optimal available power, so that the rf amplitude could be changed to account for the drop in optical power as the frequency was moved away from the AOM central frequency. The peak of the data shows that the optimal detuning of the cooling light is around -15 MHz.

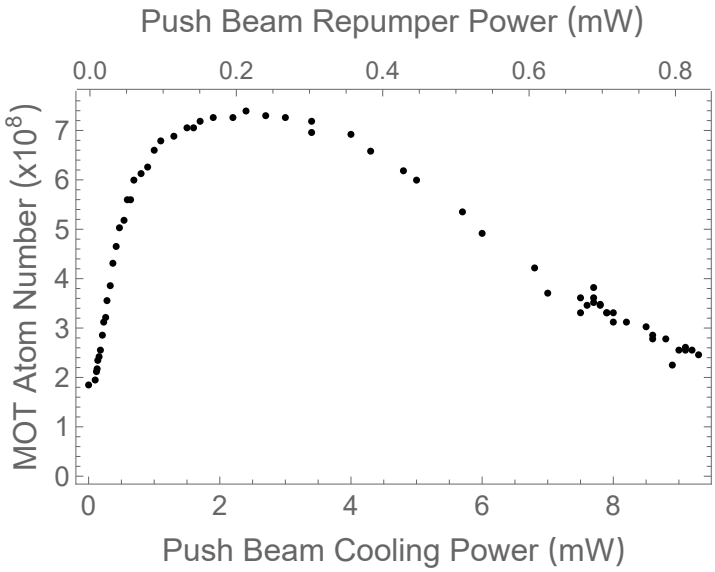


Figure 5.3: 3D MOT atom number, after 400 ms of loading, for varying 2D MOT push beam powers. This data was taken with a push beam that was −7.7 MHz detuned from the $|F = 2\rangle \rightarrow |F' = 3\rangle$ transition.

Figure 5.3 shows the 3D MOT atom number after 400 ms of loading, for varying push beam powers at a constant push beam frequency, −7.7 MHz detuned from the $|F = 2\rangle \rightarrow |F' = 3\rangle$ transition. The power was altered by changing the rf amplitude applied to the push beam fibre AOM. A clear peak in atom number of around 7×10^8 is observed for a push beam containing 2.5 mW of cooling light and 0.2 mW of repump light. The decrease in atom number for high push beam cooling powers is likely to be caused by the high push beam powers causing atoms to spend less time in the CASC, and therefore being cooled for a shoter period of time. This means fewer atoms are trapped in the 2D MOT, and those that are have larger transverse velocities. This reduces the atom flux towards the 3D MOT for large push beam powers. Further details of this effect can be found in [55]. Because the push beam cooling and repump light both pass through the same fibre AOM, there is a concomitant change in the repump power with cooling power. This may explain the sharp drop in 3D MOT atom number at low push beam cooling powers, with atoms decaying into a dark state after only a few absorption/spontaneous emission cycles.

Figure 5.4 shows the 3D MOT atom number as the push beam frequency is changed, for three different push beam powers. As the push beam power is decreased, the reduction in scattering rate could be counteracted by moving

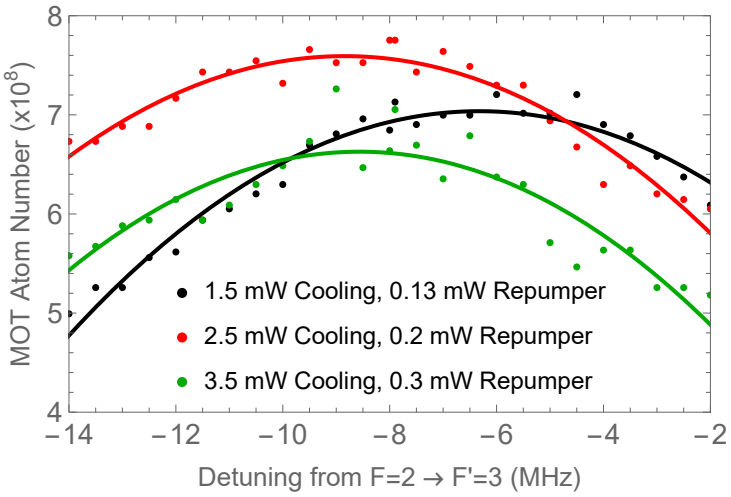


Figure 5.4: 3D MOT atom number, after 400 ms of loading, for varying push beam frequencies at three different, constant powers. As the AOM frequency was changed, the input rf amplitude was also changed, in order to keep the optical output power the same. However, as both repumper and cooling light were in the same fibre AOM, the repumper power was increased along with the cooling power for each dataset. The fits are parabolic and are meant to guide the reader's eye in order to easily see where each dataset peaks in frequency.

the frequency closer to resonance, as seen by the black data peaking closer to resonance than the red data. However, the peak atom number for the red data is higher than for the black. This shows that it is preferable to have a larger detuning and higher push beam power. As the push beam is further detuned, more faster moving atoms moving away from the main chamber are addressed by the push beam. As there are few atoms with very low velocities, moving to a larger detuning addresses more atoms, causing an increased atom number entering the main science chamber. The green data shows that this trend does not continue indefinitely however. In the same way as shown in figure 5.3, as the push beam power increases, atoms spend less time in the 2D MOT cooling region, and the atom flux towards the 3D MOT is reduced, causing the decrease in peak 3D MOT atom number.

5.1.2 3D MOT

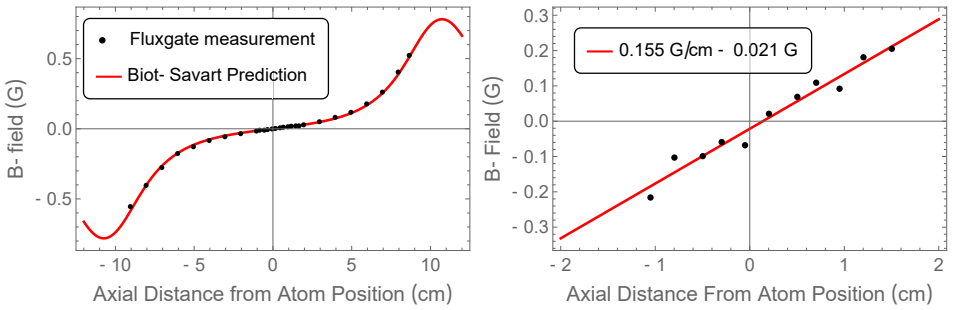
Section 4.7.1.1 described the MOT coils used to create the quadrupole magnetic field for the 3D MOT. After winding the coils with 34 radial and 27 axial turns of wire, the magnetic field from the coils was compared to theory. The Biot-Savart Law,

$$\mathbf{B}(\mathbf{r}) = \frac{\mu_0}{4\pi} \int_C \frac{I d\mathbf{l} \times \mathbf{r}}{|\mathbf{r}|^3}, \tag{5.1}$$

can be used to calculate the axial magnetic field of a current loop of radius $|\mathbf{r}|$,

$$\mathbf{B}(z\hat{\mathbf{z}}) = \frac{\mu_0 I}{2} \frac{r^2}{(z^2 + r^2)^{\frac{3}{2}}} \hat{\mathbf{z}}. \tag{5.2}$$

Here, μ_0 is the magnetic constant [1], I is the current through a current carrying element of length $d\mathbf{l}$, which is along path C. Considering each turn of the coil as a separate loop of current carrying wire and summing over all loops, the overall axial magnetic field from the coils can be calculated.



(a) (b)

Figure 5.5: (a) Axial magnetic field for the 3D MOT coils, with a 50 mA driving current. The red line shows theory, and the black points are measurements using a flux-gate magnetometer. (b) Graph showing the central region of (a). A linear fit (red) was made to this central region data and used to calculate the MOT field gradient per unit current.

Figure 5.5a shows the axial magnetic field measured using a flux gate sensor, compared to theory, for a 50 mA driving current, or 25 mA per coil due to the coils being connected in parallel. Figure 5.5b shows the central region of figure 5.5a, with a linear fit made to the data, shown in red. The gradient of the linear fit is $0.155\,\mathrm{G\,cm^{-1}}$, giving a magnetic field gradient of the MOT coils of $6.2\,\mathrm{G\,cm^{-1}\,A^{-1}}$. The offset from zero at the centre of the MOT coils indicates imperfect cancellation of background magnetic fields. This background is removed using the bias coils during usual operation. After setting up the 3D MOT, the on-axis magnetic field gradient which maximised the atom number was initially found to be around $15.5\,\mathrm{G\,cm^{-1}}$, although this value was highly dependent on other trap parameters, so was regularly changed. This field gradient required 2.5 A.

Immediately after 3D MOT trapping, sub-Doppler cooling takes place, which requires zero magnetic field. To achieve this, the magnetic field from the

[1] μ_0 is formerly known as the permeability of free space

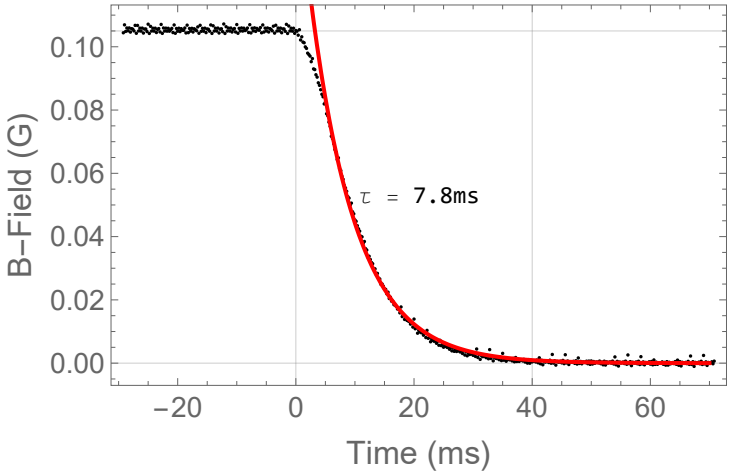


Figure 5.6: Measured magnetic field 30 cm from the longitudinal axis of the MOT coils as they were switched off using a relay. An exponential fit (red) was used to find the time constant for the coil switch off of 7.8 ms, much larger than expected based on the MOT coil inductance and resistance.

MOT coils needs to be switched off very quickly, to prevent atoms from being lost from the trap before cooling can take place. When initially using a relay to switch off the MOT coils, atom cloud temperatures were higher than anticipated. After some investigation, this was found to be due to the slow switch off of the magnetic field from the MOT coils. From the coil resistance of 4 Ω, and inductance of 9.44 mH it was expected that the time constant, τ, of the current switch off should be

$$\tau = \frac{L}{R} = \frac{9.44\,\text{mH}}{4\,\Omega} = 2.36\,\text{ms}. \tag{5.3}$$

Figure 5.6 shows the real switch off of the MOT coil, measured with a flux gate placed on the central axis of one of the MOT coils, 30 cm from the coil centre. An exponential fit to the field decay shows a significantly longer switch-off than expected, with the field not reducing to zero until 40 ms after the relay was disengaged. It is likely that this was caused by the back-EMF as the coil discharged not being able to dissipate efficiently through the current driver circuit. After discovering this, a new bipolar current driver was made, which could drive a large, reverse current through the MOT coils, and allow the field to switch off much more quickly.

Figure 5.7 shows the magnetic field measured 30 cm from the MOT coils along their longitudinal axis for several different reverse currents applied to the coils during switch off. In each case, the reverse current was applied for 5 ms. It is clear from this figure that the switch off is significantly shortened,

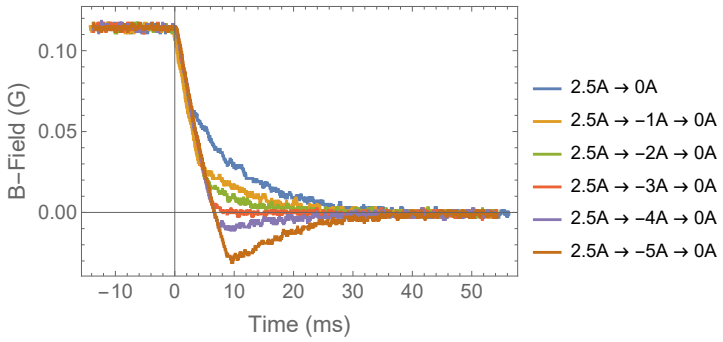


Figure 5.7: Measured magnetic field 30 cm along the longitudinal axis of the MOT coils as they were switched off using a bipolar current driver with different reverse currents. The reverse current was applied for 5 ms in each case before being switched to 0 A.

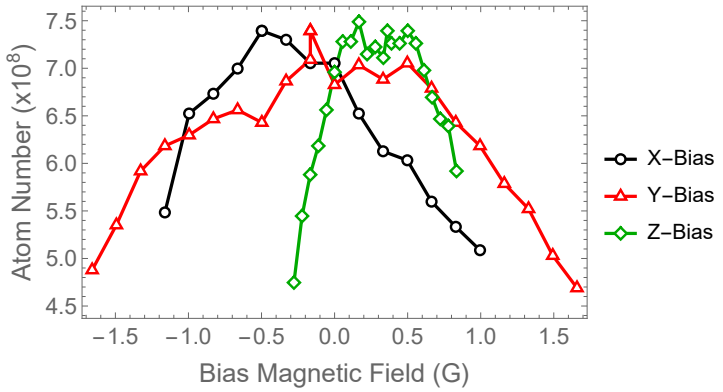


Figure 5.8: Atom number in the 3D MOT, after 400 ms of loading, as the bias coil magnetic field along each three directions was varied. The MOT beam cooling power was 28 mW and the repumper was 1.5 mW per beam. When not being scanned, the bias coil currents were set as follows: $B_x = -0.5$ G, $B_y = -0.2$ G, $B_z = 0.4$ G.

and a reverse current of 3 A gives the best switch off time of around 6 ms. After this, a 10 ms delay between MOT cooling and the molasses ramps was introduced, which allowed the MOT coil field to completely dissipate before Sisyphus cooling. After removing the residual magnetic field due to the MOT coils, the background magnetic field was removed during MOT loading by using the bias coils. Figure 5.8 shows the 3D MOT atom number after 400 ms of loading, while varying the current through each of the bias coils. In each direction, there is a field strength which gives a maximum atom number, which will be at the magnetic field value which cancels out the background field. These were set as the initial magnetic field compensation offset fields.

To optimise the 3D MOT beams, the cooling AOM was used to vary the cooling beam power in all of the MOT beams. Figure 5.9 shows the MOT

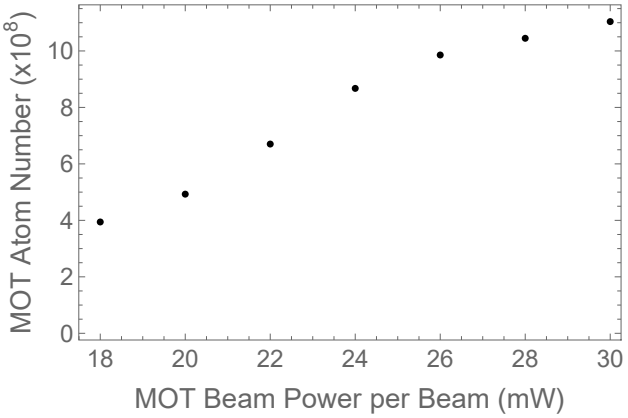


Figure 5.9: Atom number in the 3D MOT, after 400 ms of loading, as the cooling power in each MOT beam was increased. The repumper power was maintained at 1 mW per beam and the 2D+ MOT settings were optimised for atom number at each MOT beam power setting.

atom number, after 400 ms of loading, while varying the MOT beam cooling power. Throughout this measurement, the MOT cooling detuning remained at -15 MHz, the repumper light was kept at a constant power and frequency, and for each data point, the 2D MOT settings were varied to maximise the atom number. The maximum available cooling power was 30 mW per MOT beam, but no turning point in the atom number is observed up to this power. This means that more cooling power in the 3D MOT beams would increase the 3D MOT atom number. After optimisation of each of the 2D+ and 3D MOT parameters, the final 3D MOT loading rate was calculated. Figure 5.10 shows a plot of atom number against MOT loading time. The number of atoms in a 3D MOT is determined by the balance between the atom capture rate, R, and the loss rate due to collisions with background gases, Γ. There will also be some loss due to atom-atom collisions within the trap but this is assumed to by small compared to the background gas collision rate, as stated in [76]. The atom number can be well approximated as

$$N(t) = N_\infty \left(1 - e^{-\Gamma t}\right), \tag{5.4}$$

where $N_\infty = R/\Gamma$ is the steady state atom number, and t is the loading time. From the fit in 5.10, the steady state atom number is 2.0×10^9 and the loading rate is $7.8 \times 10^9\,\mathrm{s}^{-1}$. While up to 2.0×10^9 atoms could be trapped using the optimised 3D MOT settings, this would take around 800 ms of loading time. To increase the data rate of the experiment, a shorter loading time of 400 ms was chosen, by which time around 1.7×10^9 atoms are trapped.

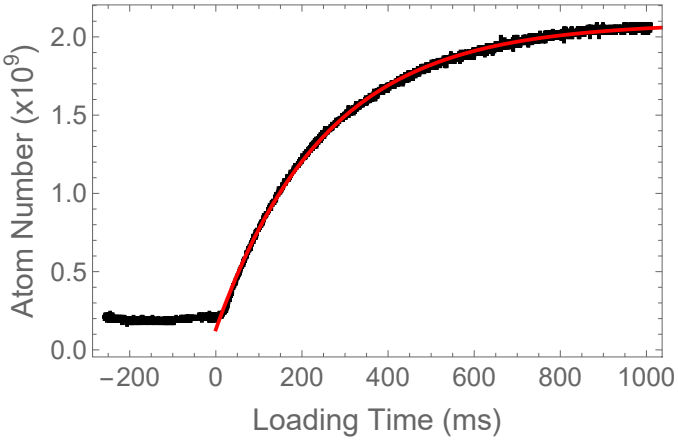


Figure 5.10: Atom number during 3D MOT loading against loading time. The red curve is an exponential fit with functional form given by equation (5.4).

5.1.3 Sub-Doppler Cooling

5.1.3.1 Atom Temperature

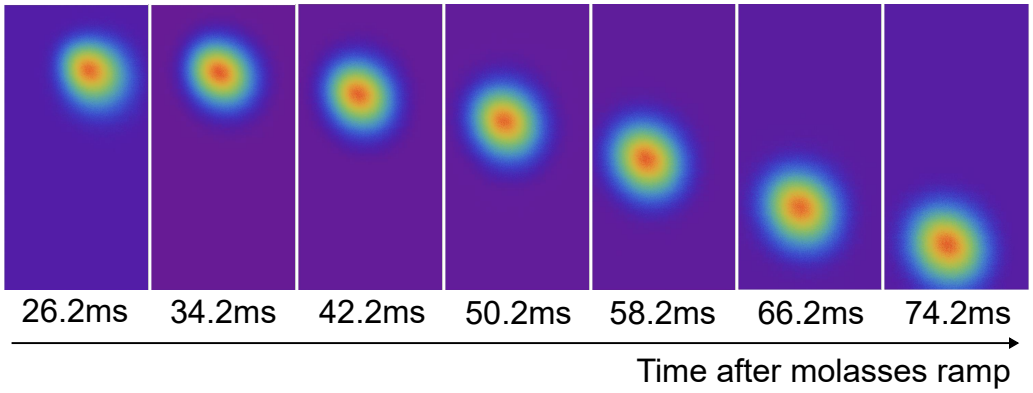


Figure 5.11: Images of the atomic cloud spaced 8 ms apart, showing the cloud falling under gravity. For these images, a $27.3\,\mathrm{cm\,s^{-1}}$ vertical launch was applied. These images were used to measure the atom cloud temperature.

To measure the atom cloud temperature, the "ballistic expansion" method was used. At variable times after the molasses ramps, cooling light from the two vertical MOT beams was triggered to turn on, causing the atom cloud to fluoresce. At the same time, a CCD camera was used to take images of the atom cloud. Example images can be seen in figure 5.11. The MOT beams were set to be resonant with the $|F = 2\rangle \rightarrow |F' = 3\rangle$ transition, with 30 mW of light in each of the beams. Afterwards, a pulse of 1 MHz detuned light

from one horizontal and one vertical MOT beam was used to blow all of the atoms away from the camera detection region, before the same vertical MOT beams were used to take a background image. After subtracting the background, the image was integrated along each of its pixel axes separately, giving two approximately Gaussian profiles. A 1D Gaussian was fitted to each of the integrated profiles and a width was determined. Assuming a perfect Gaussian distribution of atoms, the width at time t_0, the end of the molasses, is σ_0. After some time, t, the root mean square width, $\sigma(t)$ of the cloud is [77]

$$\sigma(t) = \left(\sigma_0^2 + v^2(t - t_0)^2\right)^{1/2}, \tag{5.5}$$

where v is the velocity of the increasing cloud width. From the one dimensional thermal energy, $k_B T/2$, equation (5.5) can be related to the temperature of the cloud, T,

$$\begin{aligned} T &= \frac{mv^2}{k_B} \\ \sigma(t) &= \left(\sigma_0^2 + \frac{k_B T(t - t_0)^2}{m}\right)^{1/2}, \end{aligned} \tag{5.6}$$

where m is the ^{87}Rb atomic mass. The square of the widths along each image axis were plotted against the square of the image times after cooling. From equation (5.6), the equation of a linear fit is

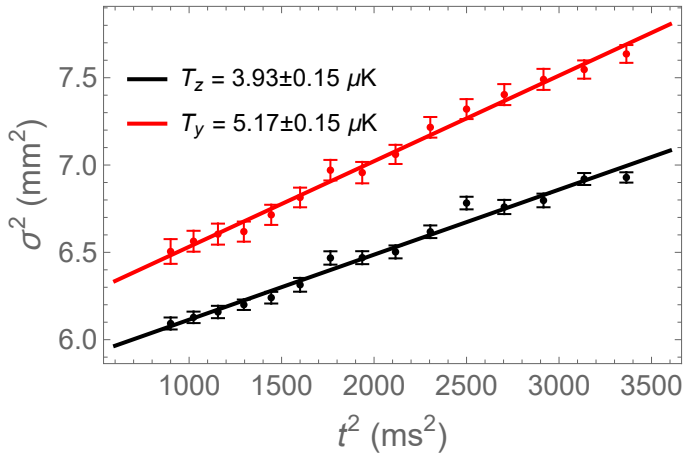


Figure 5.12: Squared cloud widths along the horizontal (black) and vertical (red) directions against the squared time after the molasses ramps. The linear fits were used to calculate the temperatures along each of these directions.

$$\sigma^2(t) = \sigma_0^2 + \frac{k_B T}{m}(t - t_0)^2. \tag{5.7}$$

The gradient of the linear fit was then used to determine the temperature of the atom cloud. Figure 5.12 shows an example of this temperature measurement, taken in the laboratory. The temperatures shown in figure 5.12 give an example of what was commonly achievable while the experiment was in the laboratory. However, due to the transportable nature of the experiment, optimal values for the MOT parameters, such as the beam alignment, the compensation magnetic field and the 3D MOT field gradient often changed. This meant that during operation, the atom cloud temperature was more often in the range of 6-8 µK.

The most common variable which needed to be optimised, was the compensation magnetic field. As the magnetic field compensation system only detects changes from an initial, minimised magnetic field, each time the experiment was moved, the bias coils were used to minimise the cloud temperature. Figure 5.13 shows how the atom cloud temperature was minimised by scanning the magnetic field from the bias coils. Before finely scanning the currents, a rough optimisation was performed by taking a CCD image of the atom cloud at a constant time after the molasses ramps. The coil current was coarsely varied, and the total number of pixel counts on the camera was maximised. While finely scanning the coil current along one direction, the other two currents were set to their coarsely optimised values. In each coil direction of figure 5.13, there is a clear minimum of temperature, which is the same for both the vertical and horizontal directions. In all three directions, the temperature is between 4 µK and 7 µK at the optimised magnetic field value. Quadratic fits have been made to each dataset, of the form $a(B_i - b)^2 + c$, where a is a scaling term describing the cloud temperature response to a change in the magnetic field, B_i, along direction i, b gives the applied magnetic field needed to minimise the temperature, and c gives the minimum achievable cloud temperature. The equations of these fits will be used as references when measuring temperatures during field trials as they give an indication of the effectiveness of the magnetic compensation system while on a moving platform.

5.1.3.2 Moving Molasses

The atom trajectories after a moving molasses, as measured using the ballistic expansion technique, are shown in figure 5.14. The black points show the atom positions with a launch detuning of 120 kHz (figure 5.14a) per horizontal beam and 300 kHz (figure 5.14b) per vertical beam. The red points

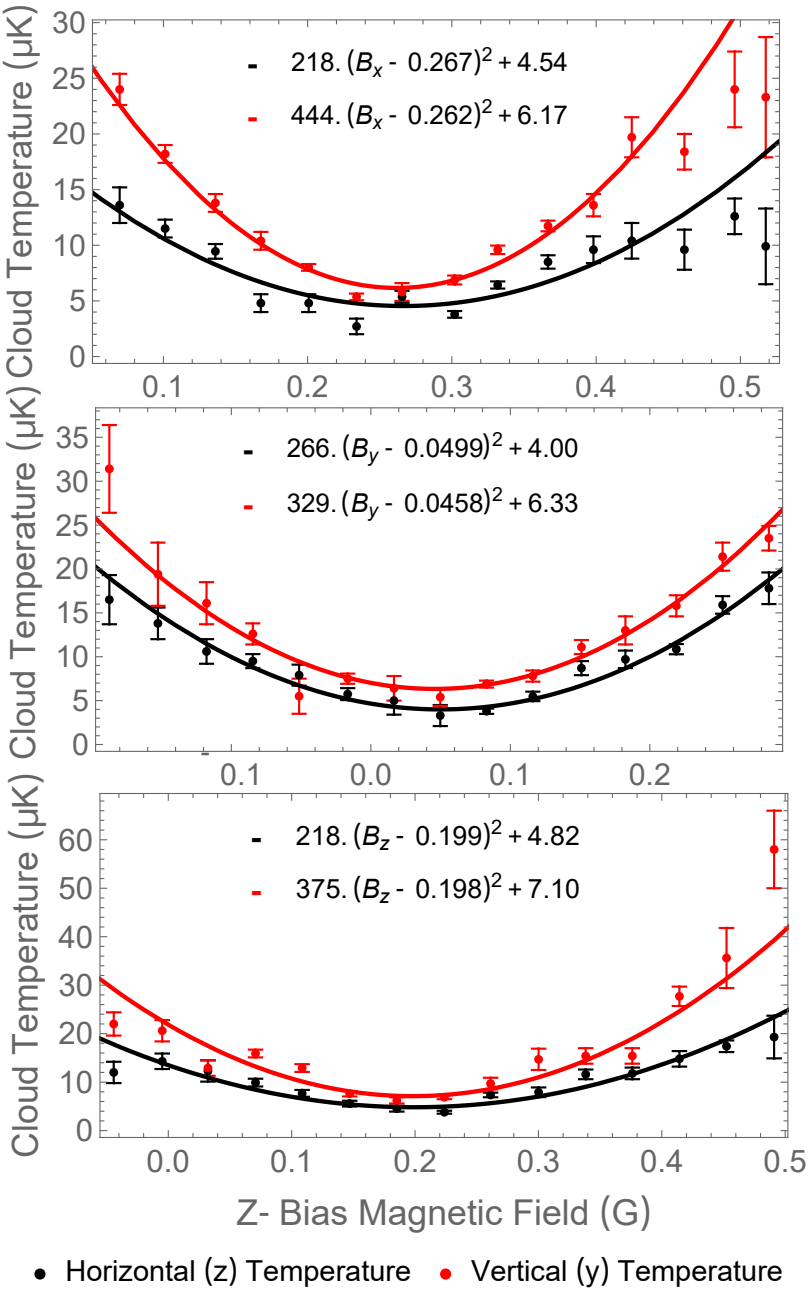
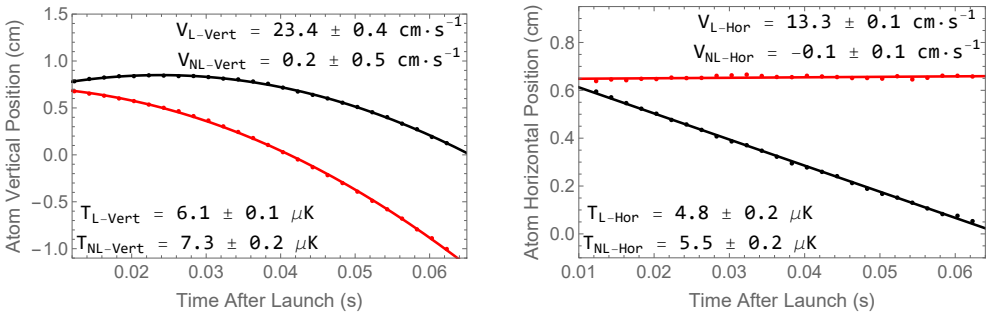


Figure 5.13: Atomic cloud temperatures in the horizontal (black) and vertical (red) directions measured using ballistic expansion, as the applied magnetic field along x (top), y (middle), and z (bottom) directions was varied. When not being scanned, the bias coil fields were set as follows: $B_x = 0.25\,G$, $B_y = -0.05\,G$, $B_z = -0.15\,G$. Quadratic fits were made to each dataset with equations shown inset.



(a) (b)

Figure 5.14: (a) Horizontal position of the atom cloud during a horizontal launch (black points) and no launch (red points). The detuning was 120 kHz on each horizontal beam. (b) Vertical position of the atom cloud during a vertical launch (black points) and no launch (red points). The detuning was 300 kHz on each vertical beam. Both sets of black and red points are from the same dataset. The legends show the velocities (V) and temperatures (T) with subscripts L and NL for launched and non-launched data respectively, and Hor and Vert for horizontal and vertical respectively.

show the trajectories for an atom cloud with no applied launch. The black and red lines are fits of the launched and non-launched data respectively, from which the vertical and horizontal velocities were calculated. In both the vertical and horizontal directions, the velocities were consistent with the expected values, to within errors, for both launched and non-launched clouds.

As well as the launch velocities, it was important to check that the launch did not increase the atom cloud temperature significantly. Figure 5.14 shows that for the launched cloud, the temperatures in both horizontal and vertical directions were lower than for the non-launched cloud. For both sets of data, the magnetic fields were kept constant, and there was no significant change in the background field between the two measurements. This suggests that for different launches, slightly different magnetic fields are required to minimise the cloud temperature. This is likely to be due to some curvature of the applied magnetic field from the bias coils. Simulations of the magnetic field produced by the bias coils show that for a 5 mm change in position of the atom cloud from the centre of the coils, and a 1 A applied current, the magnetic field differs by around 5 mG. Based on the data shown in figure 5.13, a 5 mG change would cause a temperature increase of around 0.3 µK. If this effect is multiplied due to atomic motion along multiple directions, it is possible that this curvature could be the cause of the increased temperature. While a 1 µK temperature increase will have a small effect on the interferometer overall, the fact that different applied magnetic fields are required for different launches could potentially cause larger problems on a moving platform. For

example, if the magnetic compensation system error is 50 mG, the increase in temperature due to a 5 mm cloud position change, in one direction only, increases by an extra 2 µK, on top of the 4 µK due to the compensation error itself. To improve the magnetic field curvature, the bias coils could be made circular and their separation could be changed to equal the coil radius. In the future, it would be useful to investigate how the atom cloud temperature changes for different launches in a more rigorous, systematic way. However for this thesis, it is accepted that the launch applies the desired velocity, with no heating of the cloud, as long as the magnetic field is optimised for the specific launch applied.

5.2 Hyperfine Spectra

Before discussing the state preparation stages in detail, two methods of measuring the hyperfine spectrum of ^{87}Rb will be introduced. These methods will be used to show the population in each of the different hyperfine states during and after state preparation, as well as different Zeeman sub-levels, and highlight the effects of co-propagating and counter-propagating Raman transitions.

5.2.1 Raman Spectrum

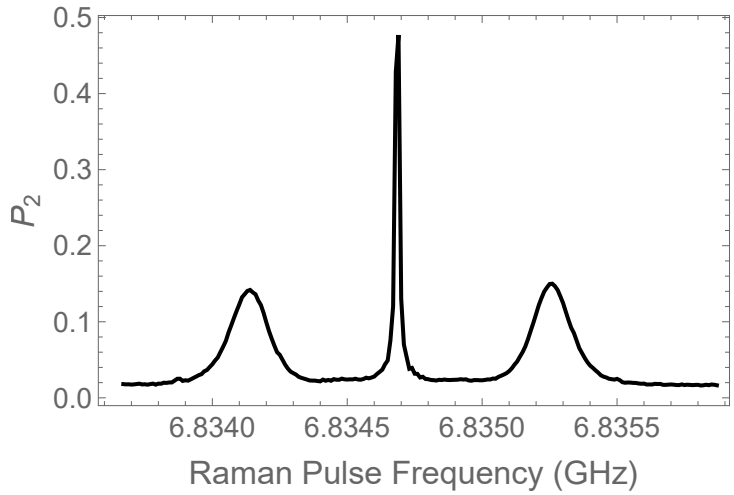


Figure 5.15: Example of a Raman spectrum taken by scanning the Raman beam frequency and measuring the $|F = 2\rangle$ population. The two, broadened peaks on either side are due to counter-propagating Raman transitions, and the thin, central peak is due to co-propagating transitions. The Raman pulse duration was 48 µs.

When optimising the interferometer, it is necessary to precisely know the frequencies at which stimulated Raman transitions will occur. If all atoms are initially prepared in one of the hyperfine states, in this case $|F = 1\rangle$, the frequency of a single Raman pulse can be scanned, and the proportion of atoms transferred to $|F = 2\rangle$ can be recorded. This is done by scanning the frequency of the local oscillator in the phase lock over a number of different experimental shots. Figure 5.15 shows an example of such a scan, using a 48 µs Raman pulse. The thin, central peak, centred at ν_{hf}, is due to the co-propagating beams driving Raman transitions, indicating a polarisation imperfection in the Raman beam. For co-propagating transitions, both photons are travelling in the same direction, and so any Doppler shift due to atomic motion will be equivalent for each. This means that the overall frequency difference between the two photons is Doppler insensitive, and the transition only happens close to ν_{hf}. The width of this peak is dominated by the Fourier width of the applied Raman pulse. The two broader peaks situated either side of the co-propagating peak are due to the two counter-propagating Raman transitions. Before the Raman pulse was applied, the atoms were launched at $22\,\mathrm{cm\,s^{-1}}$ along the Raman beam. As the counter-propagating transitions are Doppler sensitive, this atomic velocity causes a shift in the the peak position of around 580 kHz with each peak being shifted in the opposite direction. The counter-propagating peaks are also broadened due to thermal motion of the atoms along the Raman beam. Whenever a stimulated Raman transition is performed during the experiment, or during Raman scans, a uniform magnetic field of 500 mG is applied using the z compensation coils along the Raman beam direction. This ensures that only the $|F = 1, m_F = 0\rangle \rightarrow |F = 2, m_F = 0\rangle$ transition can be driven. This magnetic field is referred to as the "Raman bias magnetic field".

5.2.2 Microwave Spectrum

To ensure atoms are only prepared in the desired hyperfine energy level, it is necessary to show the atomic states of all atoms at each stage of the experiment. Microwave pulses are velocity insensitive, so can be used to show the atom populations in each Zeeman sub-level, regardless of their velocity, unlike the Raman spectrum, which will only interact with slower moving atoms. Figure 5.16 shows a microwave spectrum including all of the possible microwave transitions from $|F = 1\rangle$ to $|F = 2\rangle$. The specific transitions for these peaks are shown in figure 5.17.

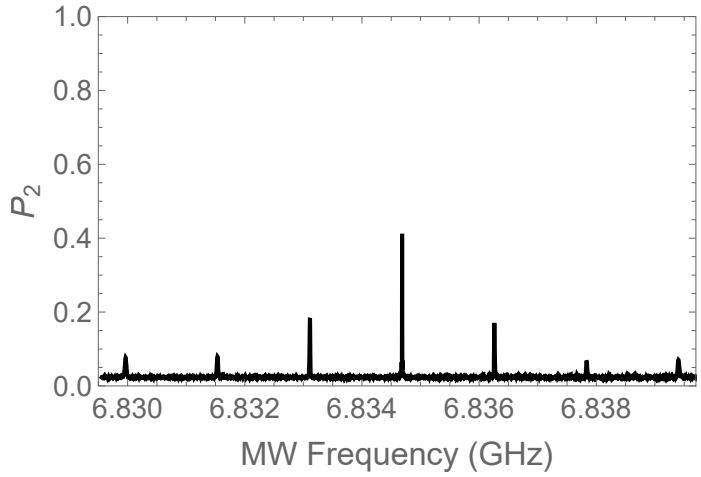


Figure 5.16: Microwave spectrum, using a 120 µs pulse, taken after pumping all atoms into the $|F = 1\rangle$ groundstate, with atoms distributed amongst each of the different Zeeman sub-levels. A uniform magnetic field of 2.3 G was applied along the y direction, perpendicular to the microwave propagation direction. This field separated the m_F states such that they were clearly resolvable. This was the field strength used during the microwave pulses in the experiement.

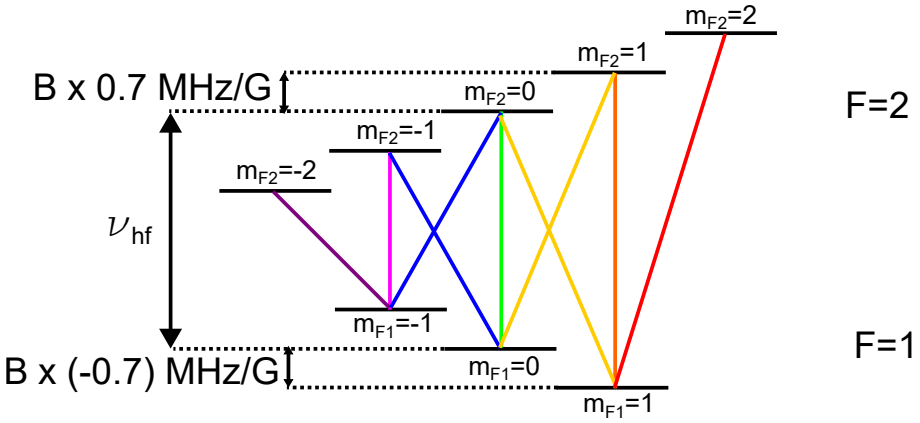
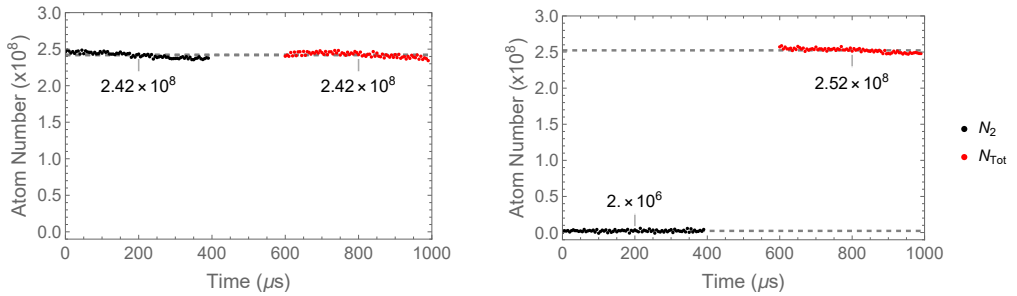


Figure 5.17: All possible microwave transitions between the different m_F levels of $|F = 1\rangle$ and $|F = 2\rangle$, in a magnetic field of strength B. There are nine transitions in total, with transitions of the same energy highlighted in the same colour. Overall there are seven different transition energies which been seen as seven peaks in a microwave spectrum if all $|F = 1\rangle$ magnetic sub-levels are populated. In this diagram, the subscripts of each m_F level correspond to the associated F quantum number for that hyperfine energy level.

5.3 State Selection

During sub-Doppler cooling, due to the presence of the repumper beam, atoms are pumped to the $|F = 2\rangle$ state. Figure 5.18a shows an atom number



(a) (b)

Figure 5.18: (a) A typical measurement of atom number using the fluorescence detection scheme taken after optical molasses but with no state selection stages applied. (b) Typical atom number measurement after atoms were pumped into $|F = 1\rangle$ during state selection stage one. No other state selection stages were applied. The applied state selection stage one pulse used two vertical MOT beams of 6 mW each for 140 µs. Around 99% of atoms have been pumped into $|F = 1\rangle$. The grid lines and markers show the mean atom number of the black and red data.

measurement, using fluorescence detection, taken after Sisyphus cooling. All of the atoms are found in $|F = 2\rangle$.

5.3.1 State Selection Stage 1

During the first stage of state selection, the two vertical MOT beams drive atoms from $|F = 2\rangle$ into $|F = 1\rangle$, via the intermediate state $|F' = 2\rangle$. Figure 5.18b shows the atom number from the fluorescence detection of the atomic cloud after state selection stage one is applied. A magnetic field of 0.5 G is applied along the y axis to destabilise a static dark state in $|F = 2\rangle$, and a 140 µs, 6 mW per beam pulse is applied with the two vertical MOT beams. Figure 5.18b shows the $|F = 2\rangle$ population is around 2×10^6 after stage one, giving an efficiency of greater than 99%.

5.3.2 State Selection Stage 2

After stage one of state selection, the atoms are distributed among all of the different Zeeman sub-levels of $|F = 1\rangle$. The top graph in figure 5.19 is the same as figure 5.16, and shows a microwave spectrum taken after state selection stage one. Seven peaks are visible, which correspond to the nine possible transitions from $|F = 1\rangle \rightarrow |F = 2\rangle$. This shows that all three of the magnetic sub-levels of $|F = 1\rangle$ are populated. Using the same vertical MOT beams but with light from the Apprentice laser resonant with the $|F = 1\rangle \rightarrow |F' = 0\rangle$ transition, as well as a 0.5 G magnetic field along

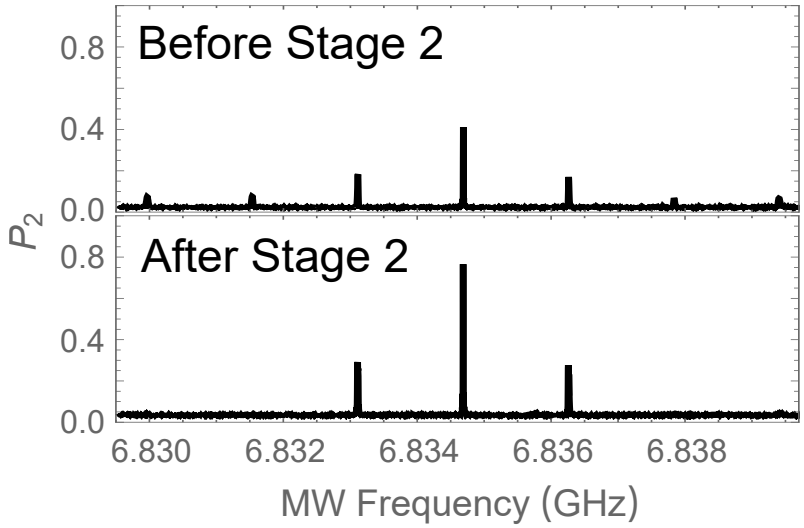


Figure 5.19: Microwave spectrum, using a 120 µs pulse, taken before (top) and after (bottom) pumping into $|F = 1, m_F = 0\rangle$ during state selection stage two. A uniform magnetic field of 2.3 G is applied, perpendicular to the microwave propagation direction. The three visible transitions after stage two, are from the $|F = 1, m_F = 0\rangle \rightarrow |F = 2, m_F = 0, \pm 1\rangle$ transitions.

the y-axis, atoms in $|F = 1, m_F = \pm 1\rangle$ are driven into $|F' = 0, m_{F'} = 0\rangle$ with σ^+ and σ^- transitions. The atoms then spontaneously decay into $|F = 1, m_F = 0\rangle$ where they become dark to the incident light. The bottom graph of figure 5.19 shows a microwave spectrum taken after state selection stage two. Comparing the two spectra in figure 5.19, the four peaks corresponding to the six transitions from $|F = 1, m_F = \pm 1\rangle$ are no longer visible, and the three visible peaks have all increased in height. These three peaks are due to the transitions from $|F = 1, m_F = 0\rangle$, showing that this is the only populated state after state selection stage two. Figure 5.20 shows an atom number measurement, using fluorescence detection, taken after state selection stages one and two are applied. In the absence of off-resonant scattering, this would look identical to figure 5.18b, as no atoms would have been removed from $|F = 1\rangle$. However, there is a small amount of pumping into $|F' = 1\rangle$ by the state selection light. Figure 5.20 shows that around 2% of the atoms end up in $|F = 2\rangle$ after stage two. These atoms are removed later in the state selection sequence with blowaway pulses.

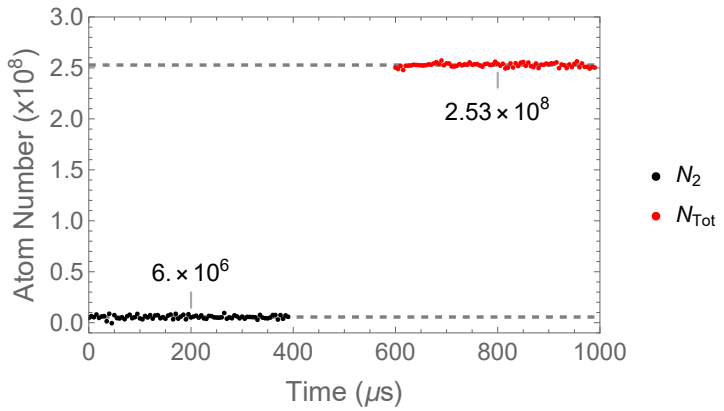


Figure 5.20: Typical atom number measurement using the fluorescence detection scheme after state selection stages one and two. Both state selection stages are 140 µs long, with the state selection one pulse of 6 mW per vertical MOT beam and the state selection 2 pulse of 55 µW per vertical MOT beam. Around 98% of atoms are in $|F = 1\rangle$, showing around 1% of atoms are pumped into $|F = 2\rangle$ during state selection stage two.

5.3.3 State Selection Stage 3

After preparing atoms in the $|F = 1, m_F = 0\rangle$ energy level, atoms are driven into $|F = 2, m_F = 0\rangle$ with a resonant microwave pulse. Figure 5.21 shows P_2 during a scan of the microwave pulse duration taken during state selection

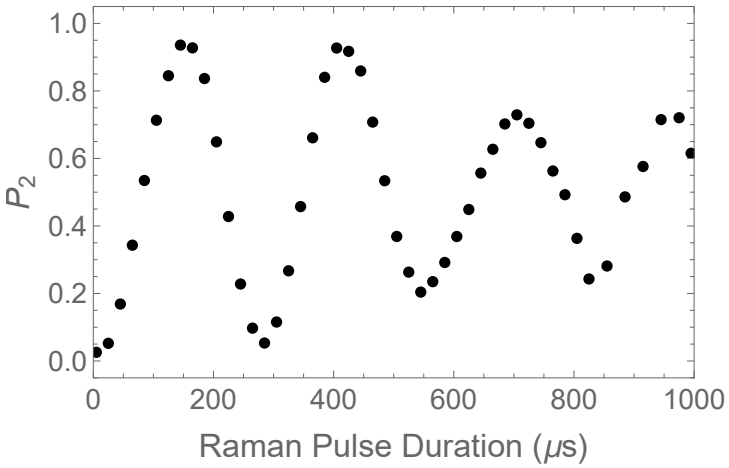
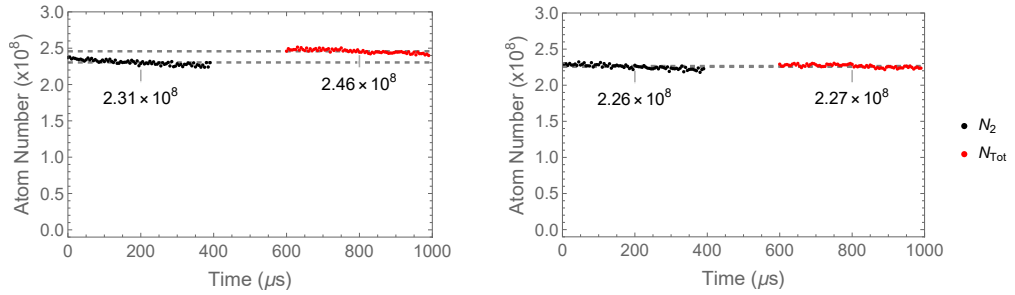


Figure 5.21: Scan of the microwave pulse duration for the $|F = 1, m_F = 0\rangle \rightarrow |F = 2, m_F = 0\rangle$ transition after state selection stages one and two. Clear Rabi oscillations persisting for longer than 1000 µs can be observed. The peak of the first oscillation was used to determine the microwave π-time of 145 µs, which was used in state selection stage three.

stage three. The scan shows Rabi oscillations of the atoms. The duration corresponding to the first peak in this oscillation was used to transfer the maximum number of atoms into $|F = 2, m_F = 0\rangle$. As the microwave transfer is a magnetic dipole transition, a magnetic field of 0.5 G was applied along the y direction to align the atomic dipole moment with the magnetic field of the microwaves. Figure 5.21 shows more than 93% of atoms are transferred into $|F = 2, m_F = 0\rangle$ using a 145 µs pulse.

5.3.4 State Selection Stage 4



(a) (b)

Figure 5.22: (a) Atom number data taken after state selection stages one, two and an $|F = 1, m_F = 0\rangle \rightarrow |F = 2, m_F = 0\rangle$ microwave pulse. The difference between the N_2 and N_{Tot} values is due to imperfect microwave transfer efficiency. (b) Atom number data taken after state selection stages one, two, $|F = 1, m_F = 0\rangle \rightarrow |F = 2, m_F = 0\rangle$ microwave pulse and an $|F = 1\rangle$ blowaway pulse. Atoms not transferred by the microwave pulse have been removed, and close to 100% of all remaining atoms are in the $|F = 2, m_F = 0\rangle$ state.

After the microwave pulse, around 7% of the atoms remain in $|F = 1\rangle$. Apprentice light from one horizontal and one vertical MOT beam resonant with the $|F = 1\rangle \rightarrow |F' = 0\rangle$ transition are used to blow these atoms out of the system. Each beam contains 1 mW of power. Figure 5.22 shows atom number measurements both before and after the $|F = 1\rangle$ blowaway pulse. After the blowaway pulse, around 99.5% of the remaining atoms are in $|F = 2, m_F = 0\rangle$, showing that around 71% of the atoms untransferred by the microwave pulse were blown away. The imperfect efficiency is due to off-resonant scattering from the blowaway pulse into $|F' = 1\rangle$.

5.3.5 State Selection Stage 5

After transferring all of the atoms into $|F = 2, m_F = 0\rangle$, a narrow velocity class of atoms is transferred back into $|F = 1, m_F = 0\rangle$ using a velocity selective Raman pulse. To show the effect of the velocity selection pulse, two

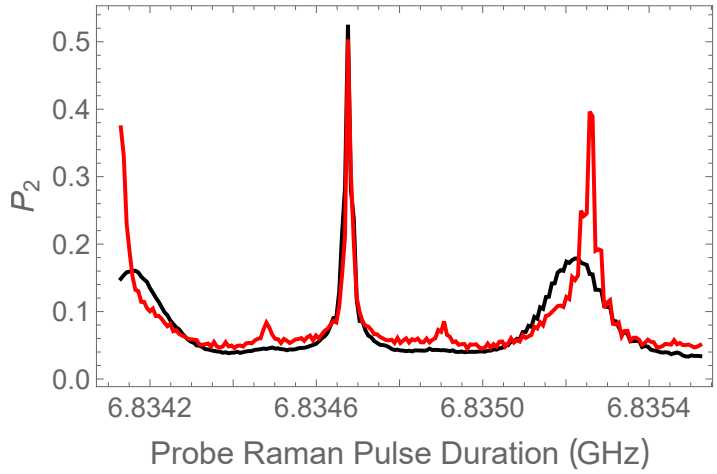
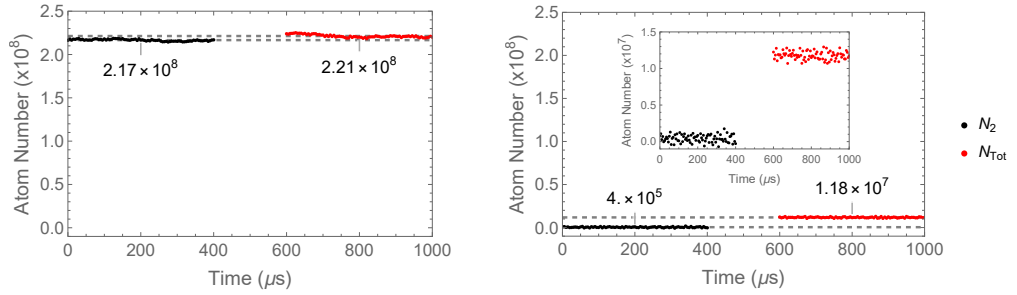


Figure 5.23: Raman spectra showing P_2, the population ratio of atoms detected in the $|F = 2\rangle$ energy level after the probe Raman pulse. For each dataset a full state selection sequence was performed, with a 135 µs velocity selection pulse for the red data, and a 145 µs microwave pulse replacing the velocity selective pulse for the black data. The probe pulse duration was 36 µs for both spectra. The small peaks seen on the velocity selected data are due to the Raman beam driving atoms into the wrong Zeeman sub-level. In each case the atom cloud temperature along the Raman beam direction was around 6 µK

Raman spectra are shown in figure 5.23. The black spectrum has no velocity selection, and the red spectrum has a 135 µs velocity selective pulse. In both cases, the initial atom cloud temperature is around 6 µK. For the black data, the velocity selection pulse was replaced with a velocity insensitive microwave pulse. Other than this, the same state selection sequence was applied for both spectra. In both cases the probing Raman pulse which was scanned in frequency was 36 µs long. For the velocity selected case, the counter-propagating peaks have narrowed and increased in height, as expected for a reduced effective cloud temperature. The velocity selected data also shows the appearance of two small peaks either side of the central co-propagating peak. Upon investigation, it was found that these peaks could be moved by varying the Raman bias field magnitude. As these peaks do not appear in the non-velocity selected case, it was concluded that the velocity selection pulse must be driving atoms into some of the magnetically sensitive Zeeman sub-levels. These atoms will not take part in the interferometer, but will still contribute to the detection signal, so will reduce the interferometer signal to noise. In the future of this experiment, it would be useful to determine why transitions into these levels can be driven, and improve the Raman beam to prevent this, however this is beyond the scope of this thesis.



(a) (b)

Figure 5.24: (a) Atom number detection data taken after state selection stages one to four were performed. This is equivalent to figure 5.22b but taken on a different day. (b) Atom number data taken after state selection stages one to four, a 135 µs velocity selection pulse, and an $|F = 2\rangle$ blowaway were performed. The data are shown inset on a smaller scale. In each case the atom cloud temperature along the Raman beam direction was around 5 µK.

5.3.6 State Selection Stage 6

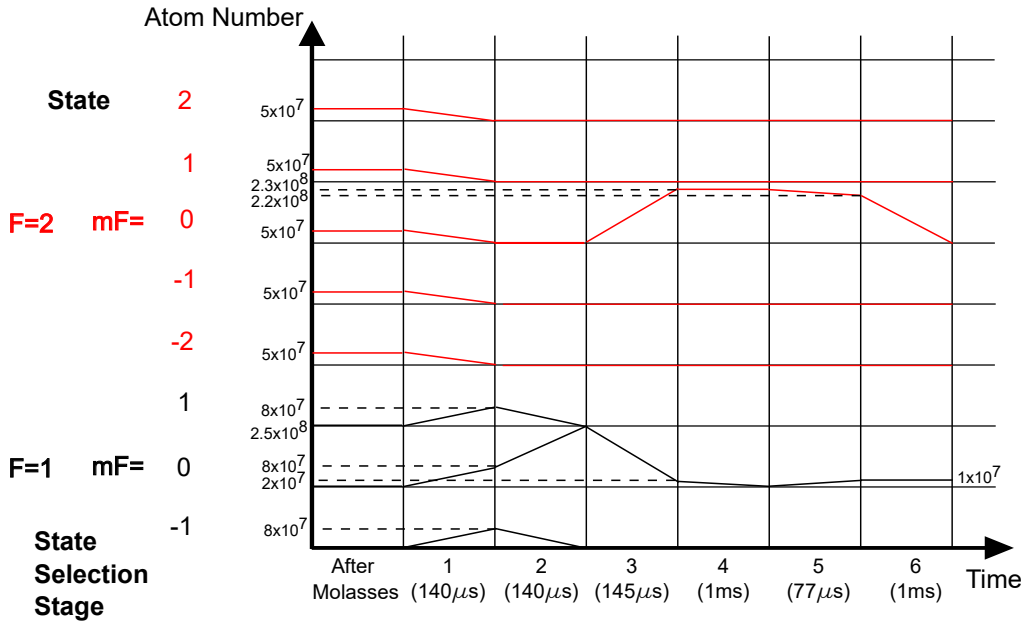


Figure 5.25: Measured populations of each Zeeman sub-level of the $|F = 1\rangle$ and $|F = 2\rangle$ states during each stage of state selection. Atom populations after molasses cooling and after state selection stage one are shown to be evenly distributed amongst the Zeeman sub-levels of $|F = 2\rangle$ and $|F = 1\rangle$ respectively. This distribution will change during different experimental shots and is unlikely to be completely uniform. This does not affect state selection efficiency.

After applying the velocity selective pulse, unselected atoms are removed by a blowaway pulse. A 1 ms, 25 mW pulse, 1 MHz detuned from the $|F = 2\rangle \rightarrow |F' = 3\rangle$ transition is used to blow all atoms in $|F = 2\rangle$ away. Figure 5.24 shows the fluorescence detection signals before and after a velocity selective pulse of 135 µs and an $|F = 2\rangle$ blowaway. Around 5% of the atoms are selected by the velocity selective pulse, giving a total atom number of 1.18×10^7 which are used in the interferometer. 4×10^5 atoms remain after the blowaway, giving an efficiency of 99.8%.

Figure 5.25 shows measured populations of each Zeeman sub-level of the $|F = 1\rangle$ and $|F = 2\rangle$ states during each stage of state selection. Changes in atom number are shown to be linear when this is not likely to be the case in reality. It is also assumed that atoms are equally split between each Zeeman sub-level after sub-Doppler cooling, and after stage one. In general, the distribution will not be uniform, but this does not impact state selection efficiency.

5.4 Stimulated Raman Interactions

5.4.1 The Raman Beam

5.4.1.1 Collimation

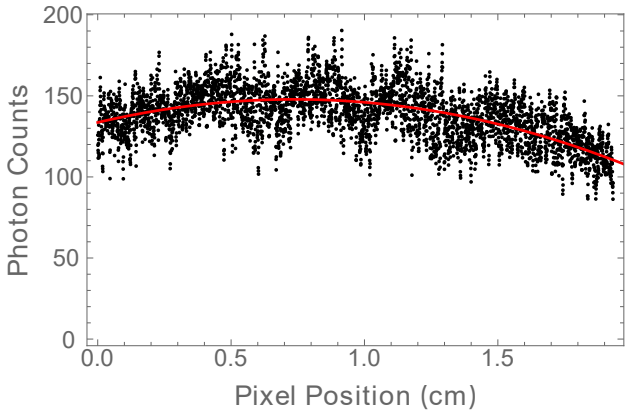


Figure 5.26: Slice from a CCD image image of the Raman beam used to measure the beam collimation. A parabolic fit (red) was made to each slice, and the widths of the parabolas were used to determine the beam width at a number of positions away from the telescope.

To achieve a Raman telescope divergence angle of less than 60 µrad, thin spacer rings were placed between the fibre input plate and the 50 mm colli-

mating lens. The required tolerance on the lens and fibre plate position was around 0.3 mm, so rings with thickness down to 0.2 mm were used. The beam divergence angle for each configuration of spacer rings was measured using a camera with a large (36 mm × 24 mm) CCD. The camera was used to image the light from the Raman telescope at different distances from the telescope output. The data from the camera images at each position were split into slices along x and y, and a parabola with the form $A\left(1-\frac{(x-x_0)^2}{2\sigma^2}\right)$ was fitted to each dataset. Figure 5.26 shows an example slice of data from a camera image of the Raman beam. The fluctuations in each slice are dominated by noise in the camera. The oscillation seen in the central region of the slice is due to an etalon created by different layers within the CCD. The fitting parameters A, x_0, and σ come from the Taylor expansion of a Gaussian about its centre. By averaging over the slices from each image, a beam width, σ, for each camera position was plotted against distance from the telescope. Figure 5.27 shows how the gradient of a linear fit to this graph was used to determine a divergence angle for the beam. The divergence angle achieved was -33 ± 58 µrad. This is consistent with a perfectly collimated beam. For a collimation angle of 91 µrad, one standard deviation from the measured collimation angle, the acceleration error can be calculated to be 260 ng for a 50 ms 2T-time interferometer (see figure 2.9).

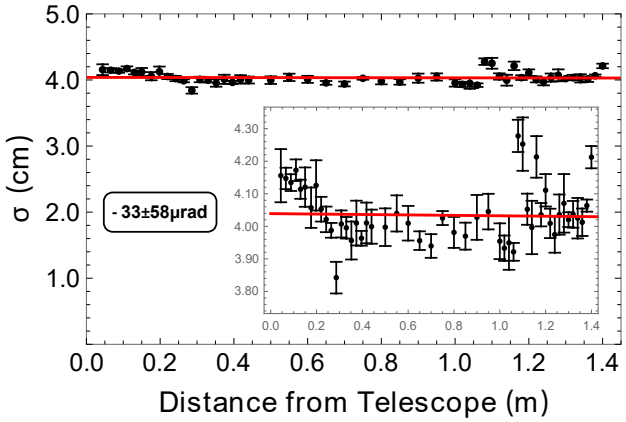


Figure 5.27: Measured Raman beam widths against distance from the Raman telescope. A linear fit (red) is used to determine a divergence angle of the beam. The divergence angle measured is consistent with being perfectly collimated.

5.4.1.2 Polarisation

Figure 5.28 shows the optical setup used to measure the polarisation of the Raman beam. A polarising beamsplitter removed any polarisation ellipticity

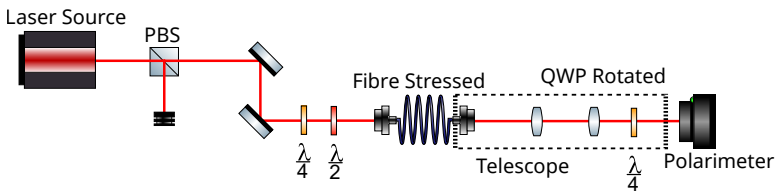


Figure 5.28: The setup of optics used to measure the polarisation of the Raman telescope light.

from the laser source, and a quarter and a half waveplate were used to rotate the input light polarisation to the fast axis of the PM fibre of the telescope. To test the polarisation drift, it was necessary to mechanically stress the PM fibre during measurements with the polarimeter. This is because mechanical stress induces a phase shift of the light along the slow axis of the fibre, which alters the interference between the fast and slow axes [78]. In practice this means that if incident light is not perfectly aligned to the fast or slow axis, there will be some light propagating along each of them. The stress changes how much light propagates along each axis and changes the output polarisation. In a perfectly aligned fibre, all light will be travelling along one of the fibre axes, and the mechanical stress will have no impact on the

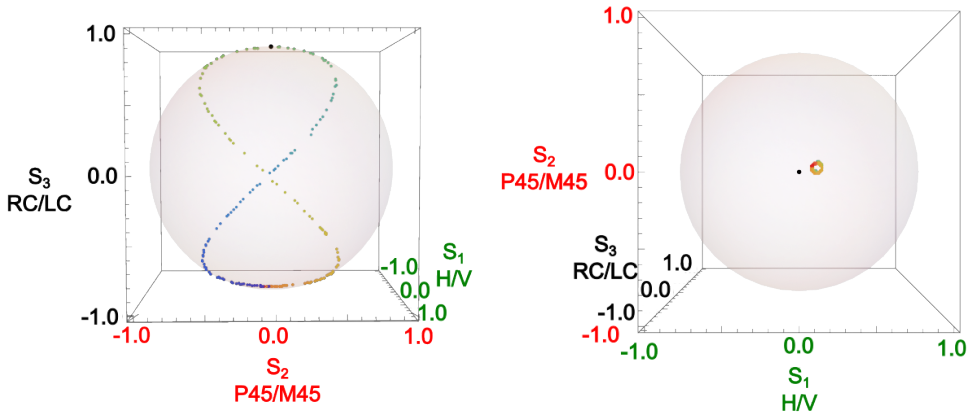


Figure 5.29: Poincaré spheres showing the polarisation of light out of the Raman telescope as the quarter waveplate is rotated through 360° (a) and after the quarter waveplate angle was optimised and the fibre feedthrough was stressed by heating along its length (b). The black spot in the centre of the sphere shows perfect circular polarisation. The axes are the three Stokes parameters, with labels describing their phyical meaning. H/V describes whether the light has horizontal or vertical polarisation, P45/M45 describes the angle of polarisation, and RC/LC describes whether the light is right or left hand circularly polarised.

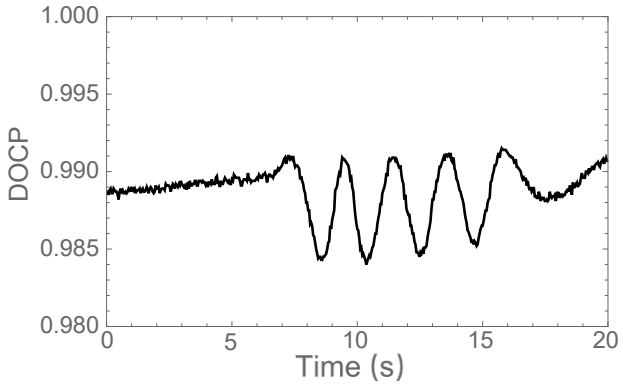


Figure 5.30: Degree of circular polarisation (DOCP) of light from the Raman telescope while the PM fibre was stressed using a heat gun.

output polarisation. To ensure that changes in the polarisation measured on the polarimeter were due to the angle of the telescope quarter waveplate only, the quarter waveplate was initially removed, and the variation in polarisation during mechanical stress of the fibre was minimised by rotating the quarter and half waveplates at the fibre input. After ensuring the PM fibre was well aligned, the quarter waveplate was replaced and the rotated. The impact of rotating the waveplate through 360° can be seen in figure 5.29a. After turning the quarter waveplate to give as close to circular polarisation as possible, the fibre was stressed by heating it with a heat gun. The Poincaré sphere for this is shown in figure 5.29b, where the black dot shows perfect right-hand circular polarisation. To quantitatively look at this polarisation we can look at the degree of circular polarisation (DOCP) of the beam, which is defined as:

$$\mathrm{DOCP} = \frac{S_3}{S_0}, \tag{5.8}$$

where S_0 and S_3 are the Stokes parameters [79]. This gives the ratio of the power of circularly polarised light to the total light power. For perfectly right-hand circularly polarised light, the DOCP equals one. The DOCP for the data shown in figure 5.29b is shown in figure 5.30. The oscillation seen is due to the fibre being stressed and is therefore due to some misalignment or ellipticity of the beam on the input to the fibre. Despite the oscillation, throughout the stressing, the DOCP was between 98.5% and 99% of light being right hand circularly polarised. This means that, assuming the input light is aligned to the PM fibre as well as during testing, there will be a maximum of 1.5% of Raman light with the wrong polarisation during the experiment.

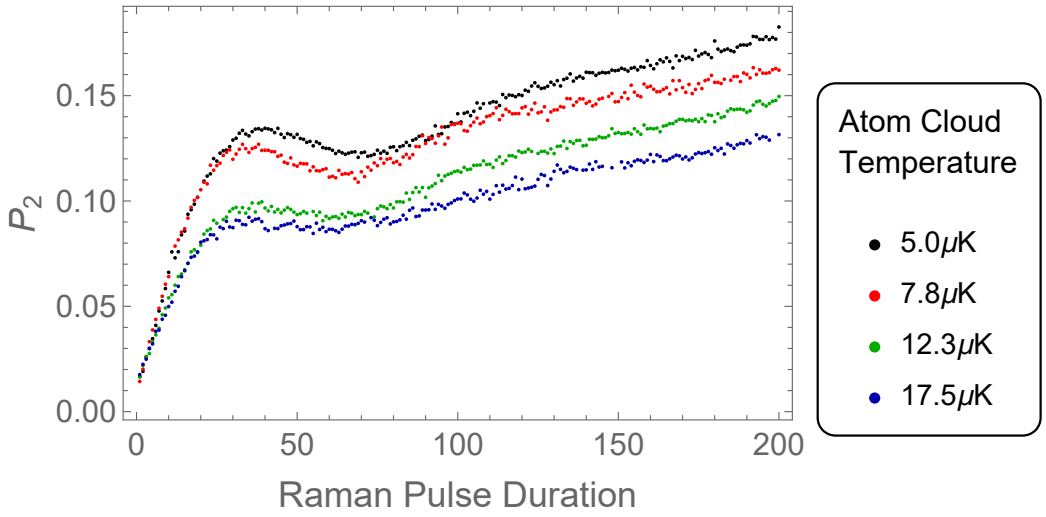


Figure 5.31: Rabi oscillations with varying atom cloud temperatures. In each case, a magnetic field was applied during the molasses cooling stage to increase the cloud temperature. No velocity selection was applied for any of the scans.

5.5 Rabi Ocscillations

The probability of an atom, initially in $|F = 1\rangle$, being excited by a single, resonant pulse of Raman light of duration τ is given by $P_2 = \sin^2(\Omega_{\text{eff}}\tau/2)$. The first peak in this Rabi oscillation occurs at $\Omega_{\text{eff}}\tau = \pi$. A $\pi/2$-pulse is half of this duration. Before performing a full interferometry sequence, the duration of a π-pulse was determined. After a full state preparation sequence, a single pulse of Raman light was applied to the atoms, and the pulse duration was varied.

5.5.1 Effect of Atom Cloud Temperature

Figure 5.31 shows a number of Rabi oscillations for different temperatures of atom cloud. The bias coils were used to apply a background magnetic field during sub-Doppler cooling, to vary the cloud temperature. No velocity selection was applied for any of the scans. The oscillations show increased amplitude for lower cloud temperatures, due to a narrower range of Doppler shifts from thermal motion. This highlights the importance of effective sub-Doppler cooling at the start of the experimental sequence. Despite improvements for lower cloud temperatures, all four flops dephase after only only one or two oscillations. To increase the effective coherence, velocity selection was introduced.

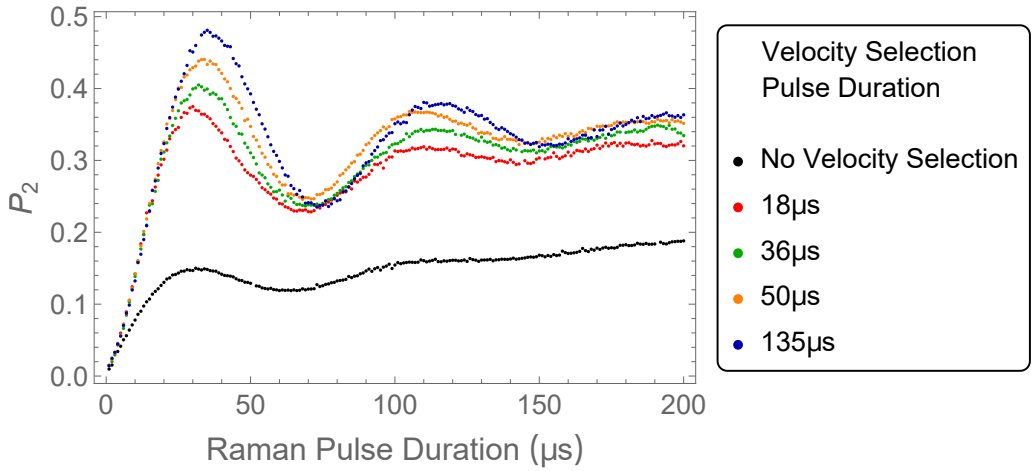


Figure 5.32: Rabi oscillations without (black) and with varying durations of velocity selection pulses. The position of the first peak of these oscillations is used to determine the π-time which is used in the the interferometry sequence. Flops with 18 µs and 36 µs velocity selection used a full power Raman pulse. The Raman beam power was reduced for the 50 µs and 135 µs oscillations, to drive a π-pulse.

5.5.2 Velocity Selection

Figure 5.32 shows several scans of Raman pulse duration for different velocity selection durations. For the data shown in black, the Raman pulse was replaced with a microwave pulse so that all atoms were selected. As the duration of the velocity selection pulse is increased, a narrower velocity class is selected, and the amplitude of the Rabi oscillations increases. This effect increases the system contrast, but at the expense of reduced atom number. Figure 5.33 shows the atom number for increasing velocity selection duration. As a narrower velocity class is selected, the atom number is reduced, which increases measurement noise. Above 64 µs, the atom number does not decrease further. Further work is required to understand why this is observed.

5.6 Three-pulse Interferometry

To realise a full interferometer, three Raman pulses are applied in a $\pi/2-\pi-\pi/2$ sequence. Figure 5.34 shows an example of how the Raman beam powers are varied during an experimental sequence for an interferometer time, T. The duration of a π-pulse is determined from the peak of the first oscillation in figure 5.32, and a $\pi/2$-pulse is half of this duration. The durations and powers shown in figure 5.34 are are typical of those used in the laboratory.

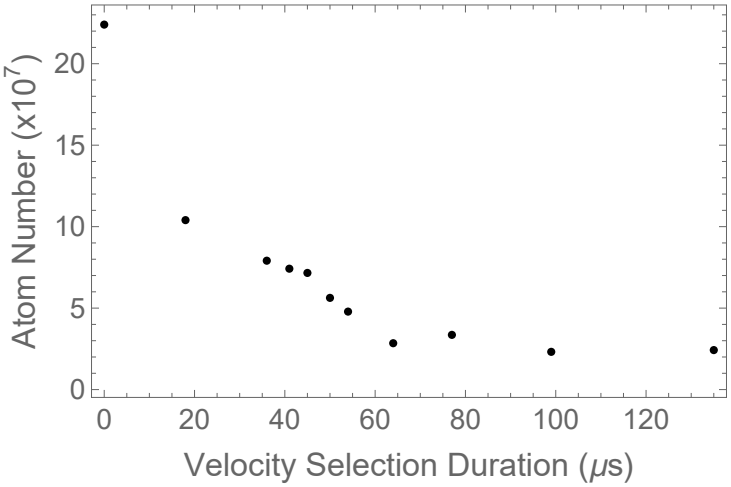


Figure 5.33: Atom number remaining in the interferometry sequence after a velocity selection pulse of varying duration, and a blowaway pulse used to remove unselected atoms.

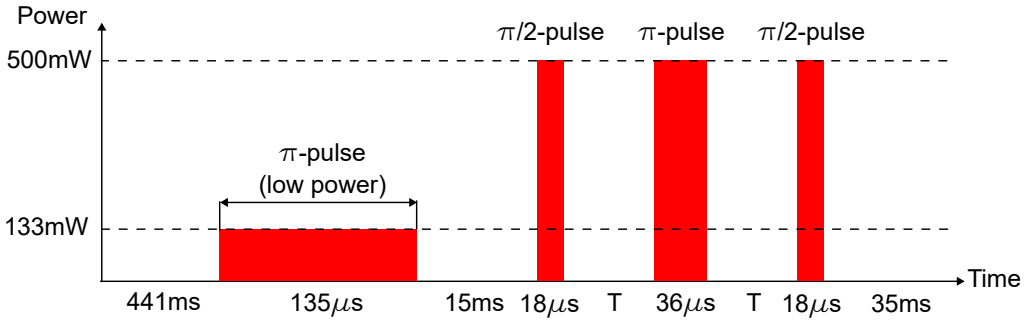


Figure 5.34: Illustration of the power of the Raman beam during a full experimental sequence with interferometer time T. The first, long pulse is during velocity selection, and the three shorter pulses are the $\pi/2 - \pi - \pi/2$ interferometry pulses. Both the powers and durations are changed regularly during testing but the values shown are typical of those used in the laboratory.

5.6.1 Interference Fringes

After the three interferometry pulses, the ratio of atoms in each hyperfine state is measured using fluorescence detection. Figure 5.35 shows an example of an interference fringe, taken by scanning the phase shifter in the phase lock during the interferometer π-pulse. The fringe is fitted using $P_2 = (1 - C\cos(\Delta\Phi))/2$, where $\Delta\Phi$ is the applied Raman beam phase, and C is the fringe contrast. Figure 5.35 was taken with a 2 ms T-time and a velocity selection pulse duration of 77 µs. The fitted function gives a fringe contrast of 0.266 ± 0.007.

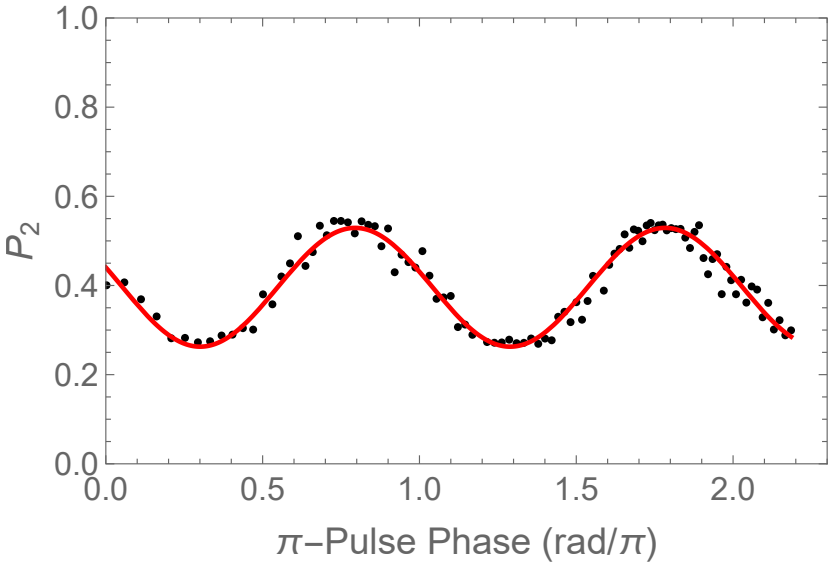
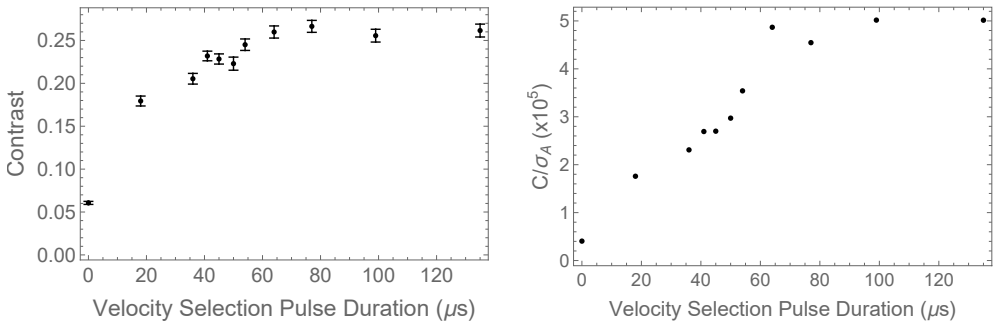


Figure 5.35: An interferometer fringe for a T-time of 2 ms. The fringe was created by scanning the laser phase during the second interferometer pulse. The π-time used was 36 µs and the velocity selection pulse duration was 77 µs. The red line shows a fit using equation (2.30) which was used to find the fringe contrast of 0.266 ± 0.007.



(a) (b)

Figure 5.36: (a) Interferometer fringe contrast against velocity pulse duration. (b) Interferometer fringe contrast divided by atom number error for the same data shown in (a).

Figure 5.36a shows the interferometer fringe contrast as the velocity selection pulse duration is increased, for a 2 ms T-time. Similarly to the atom number data shown in figure 5.33, there is little impact of increasing the velocity selection duration beyond 64 µs. Figure 5.36b shows the interferometer contrast from figure 5.36a divided by the error in the atom numbers from figure 5.33. As expected, above 64 µs, the ratio flattens out, showing that there is no benefit to further increasing the velocity selection duration. The

next stages of the experiment will investigate the reasons behind the reduced effectiveness of longer velocity selection pulses, and the optimal balance between fringe contrast and atom number, to give the best measurement signal to noise ratio.

5.6.1.1 Mirror Vibrations

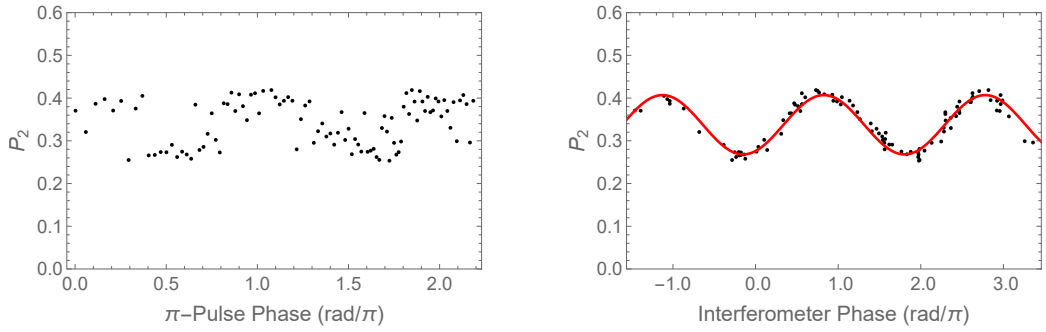


Figure 5.37: (a) A 10 ms T-time interferometer fringe without classical accelerometer correction. As the interferometer time is increased, vibrations of the system cause certain data points to have phase shifts of larger than $\frac{\pi}{2}$, and the fringe gets washed out. (b) The same fringe as in (a) but with phase correction from classical accelerometer applied. The red fit uses equation (2.30) to give a fringe contrast of 0.139 ± 0.004.

In the absence of rotation, the total phase of the atom interferometer is given by $\Delta\Phi = k_{\text{eff}} a T^2 + (\phi_{10} - 2\phi_{20} + \phi_{30})$ (equation (2.29)). For now, we will only consider the applied laser offset phase during the π-pulse, which is scanned to create an interference fringe. This phase difference changes depending on the distance of the atom from the Raman mirror, so the acceleration measured in an atom interferometer is the acceleration of the atom-mirror distance. Previously, it was assumed that the acceleration of this distance was entirely due to the motion of the whole accelerometer. However, vibrations of the Raman mirror during the interferometer will cause the atom mirror distance to change, and extra phase will be imparted onto the atoms. This extra phase will be interpretted as an erroneous acceleration, so the interferometer phase can be rewritten as $\Delta\Phi = k_{\text{eff}}(a + \delta a)T^2 - 2\phi_{20}$, where δa is the extra measured acceleration due to mirror vibration. For longer interferometer times, as the mirror vibrates for longer, the size of δa relative to a will increase, making this erroneous phase more significant. Figure 5.37a shows a scan of the laser offset phase during the interferometer π-pulse, for a 10 ms T-time. When only plotting against the laser offset phase, the fringe becomes washed out and no longer visible. To reconstruct the fringe, δa is measured using

the classical accelerometer attached to the Raman mirror, and is used to calculate the extra interferometer phase. This is added to the scanned laser offset phase, and P_2 is plotted against the overall interferometer phase.

For an atom interferometer, the response in overall interferometer phase to an instantaneous phase change, $\phi(t)$ at a time, t, can be written as

$$\delta(\Delta\Phi) = \int g(t) d\phi(t) = \int g(t) \frac{d\phi(t)}{dt} dt. \tag{5.9}$$

Here $g(t)$ is referred to as the "sensitivity function" [80]. For a three pulse, $\pi/2 - \pi - \pi/2$ interferometer, the senstivity function is given by [81]

$$g(t) = \begin{cases} -\sin(\Omega_{eff} t), & 0 < t < \tau_{\pi/2} \\ -1, & \tau_{\pi/2} < t < \tau_{\pi/2} + T \\ -\sin(\Omega_{eff}(t-T)), & \tau_{\pi/2} + T < t < \tau_{\pi/2} + T + \tau_\pi \\ 1, & \tau_{\pi/2} + T + \tau_\pi < t < \tau_{\pi/2} + 2T + \tau_\pi \\ -\sin(\Omega_{eff}(t-2T)), & \tau_{\pi/2} + 2T + \tau_\pi < t < 2\tau_{\pi/2} + 2T + \tau_\pi \\ 0, & \text{elsewhere,} \end{cases} \tag{5.10}$$

where $\tau_{\pi/2}$ and τ_π are the pulse durations for $\pi/2$ and π-pulses respectively, and T is the interferometer T-time. For short interferometer pulses, where $\tau_{\pi/2} \ll T$, equation (5.10) can be simplified to

$$g(t) = \begin{cases} -1, & 0 < t < T \\ 1, & T < t < 2T \\ 0, & \text{elsewhere.} \end{cases} \tag{5.11}$$

As we are considering a phase change due to motion of the Raman mirror, $d\phi(t)$ in equation (5.9) can be replaced by $2k_2 dx(t)$, where k_2 is the wavenumber of the retro-reflected beam, as this is the beam impacted by mirror motion. Integrating the Raman mirror position

$$\frac{d\phi(t)}{dt} = 2k_2 \frac{dx(t)}{dt} = 2k_2 v(t), \tag{5.12}$$

gives the Raman mirror velocity, $v(t)$. Substituting equation (5.12) into equation (5.9) gives the accumulated interferometer phase due to Raman mirror motion at time t

$$\delta(\Delta\Phi) = 2k_2 \int_{-\infty}^{\infty} g(t)v(t)dt, \tag{5.13}$$

where the integral limits have been extended to $[-\infty, \infty]$ as no phase is accumulated outside of the range $[0, 2T]$. Solving this, as in [81], gives

$$\delta(\Delta\Phi) = -2k_2[f(t)v(t)]_{-\infty}^{\infty} + 2k_2 \int_{-\infty}^{\infty} f(t)a(t)dt. \tag{5.14}$$

The "response function" of the interferometer

$$f(t) = -\int g(t')dt', \tag{5.15}$$

can be approximated as

$$f(t) = \begin{cases} t, & 0 < t < T \\ T - t, & T < t < 2T \\ 0, & \text{elsewhere,} \end{cases} \tag{5.16}$$

which vanishes for $t \to \pm\infty$, meaning the first term of equation (5.14) can be ignored, and the interferometer response to Raman mirror motion can be written as

$$\delta(\Delta\Phi) = 2k_2 \int_{-\infty}^{\infty} f(t)a(t)dt. \tag{5.17}$$

More detailed descriptions of the atom interferometer response to both acceleration and other noise sources can be found in [42, 81]. Since, while in the laboratory, there should be no bulk acceleration of the experiment, the only acceleration in equation (5.17) comes from vibration of the Raman mirror, which we would like to remove. By measuring the mirror vibration with the classical accelerometer attached to the Raman mirror, the additional phase can be calculated using equation (5.17), and subtracted from the values plotted in figure 5.37a. The result of this can be seen in figure 5.37b, which shows the same data as in figure 5.37a, but with correction for the mirror vibration. After correcting for the mirror vibrations, the fringe becomes visible and can be fitted to. This gives a contrast of 0.139 ± 0.004. An important next step for the experiment will be to characterise other sources of noise in detail,

as in [42], to determine the limiting factors of the interferometer, and which areas of the experiment need to be improved.

Chapter 6

Field Trials

To test the transportability of the accelerometer, field trials were undertaken, where the system was tested outside of the laboratory, in both static and mobile environments. Trials were conducted alongside the Royal Navy and QinetiQ, as part of the NavyPODS program, which will be described in section 6.1. During this chapter, I will present the characterisation of the system performance during these field trials. Comparisons with data from the laboratory will be used to highlight the strengths of the experiment, and indicate how improvements can be made for future field trials, and future iterations of the system.

6.1 The Navy POD

QinetiQ have developed a programme of Persistent Operational Deployment Systems (NavyPODS) [82] to provide modularised capability for the Royal Navy. The PODS are modified shipping containers that can be equipped to provide a range of services, including rapid repair sytems, communication centres, and research platforms. NavyX has procured a NavyPOD specifically equipped to support the deployment and testing of quantum sensors in maritime environments. Figure 6.1 shows the quantum NavyPOD, which was made available to us for field trials of our quantum enhanced accelerometer demonstrator. The POD connects to an external electric generator, which is converted into a standard mains supply internally. It also provides air conditioning for precision temperature control, and re-configurable mounting points to secure apparatus inside.



Figure 6.1: The POD aboard the XV Patrick Blackett Royal Navy research vessel (credit: Thomas Angus- Imperial College London Photographer and Image Manager).



(a) (b)

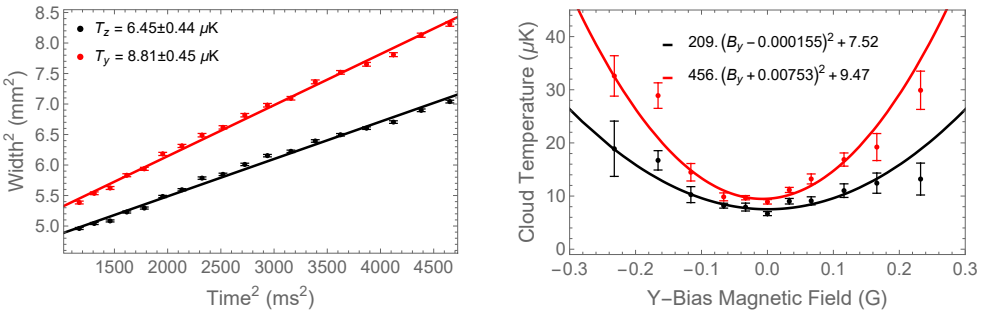
Figure 6.2: Photographs of the experiment mounting during the static field trial (a) and the Navy ship test (b). During the ship test, the wheels were replaced with shock-absorbing legs which were attached to the POD floor. Strapping at the top of each experimental box was also added for extra stability against shear forces.

6.1.1 Mounting

Figure 6.2a shows the Imperial quantum sensor installed inside the Navy POD. During static testing, the apparatus remained on its wheels, secured only using the brakes. For dynamic testing, a more robust mounting was required. Together with QinetiQ, we installed mounting fixtures into the floor of the POD, which enabled the system to be mounted using eight shock-absorbing legs. Ratchet straps fixed the top of the demonstrator to the

superstructure of the POD to provide fail-safe retention of the system in the event of a catastrophic failure of the shock-mounting legs while at sea. The ratchet straps remained slack during normal operation to prevent the transmission of vibrations through them into the quantum sensor.

6.2 Static Field Trial



(a) (b)

Figure 6.3: (a) Atom cloud width measurement taken during the static field trial taken within the first two hours after the laser was switched on. Cloud temperatures based on linear fits are shown inset. Data was taken with the compensation system switched on throughout. (b) Atom cloud temperature versus bias magnetic field along y. In each subfigure, the horizontal (z) temperature is shown in black, and the vertical (y) temperature is shown in red.

To prepare for sea trials, a *dry-run* was performed at the "Battlelab" military research facility in Dorchester. This helped us to understand the robustness of the system after transportation, and assess how quickly it could be set up in the POD.

The umbilical connecting the two demonstrator units was disconnected, with all other connections remaining in place, for transportation. The two sensor units were strapped into a Luton van[1] and driven to Battlelab. After the sensor units were wheeled into the NavyPOD at BattleLab, the laser system was switched on. It took $\sim$ 90 mins to warm up. This is longer than observed in the laboratory because the system had cooled significantly during transport. Once the laser had stabilised, some misalignment of the optical distribution system was observed, compared with the laboratory alignment. After realigning the optical system, a 3D MOT was achieved within 1 hr, and ultra cold atoms were achieved within 2 hr. Figure 6.3a shows an atom

[1] A tail lift is required to load and unload the sensors.

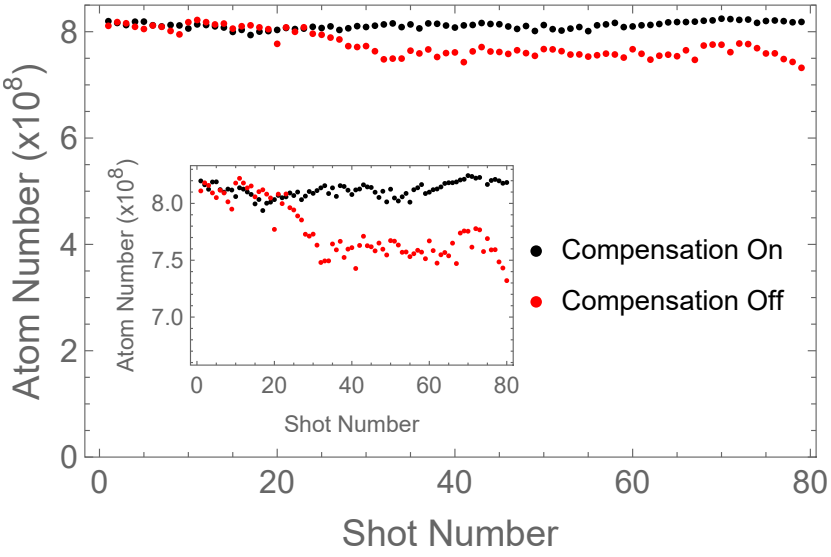
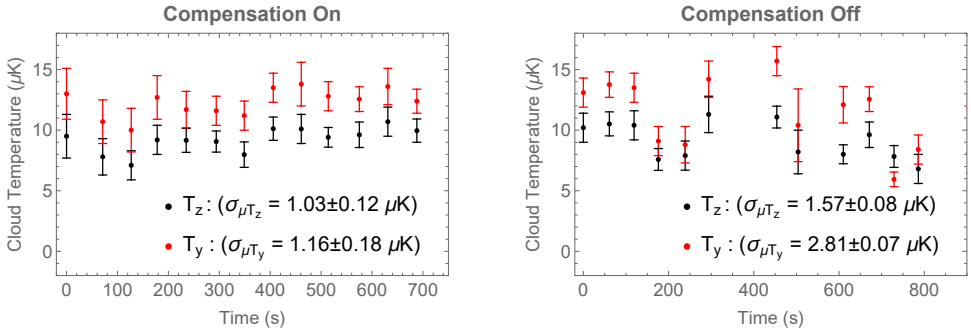


Figure 6.4: Atom number measurement taken 40 ms after sub-Doppler cooling, for 80 experimental shots. Black data was taken with magnetic field compensation engaged, and red data was taken with the compensation system disengaged. No state selection stages were applied. The two datasets were taken within five minutes of each other. The same data is shown inset with a smaller plotting range.

cloud temperature measurement, taken after initial optimisation of the MOT beam powers, alignment and bias magnetic fields. Figure 6.3b shows how the molasses temperature was affected by an external magnetic applied along the y-axis. Figure 6.4 shows the atom number measured with and without the magnetic compensation system engaged, over 80 experimental shots, lasting



(a) (b)

Figure 6.5: Static field trial temperature stability (a) with magnetic field compensation system engaged (b) without magnetic field compensation system engaged. The horizontal and vertical temperatures are shown in black and red respectively. Inset: the standard error of the mean of the temperatures along each direction.

around 120 s. The data without magnetic field compensation shows a slow decrease in atom number of around 10% over the measured time period, whereas the data with compensation engaged shows no significant drift over the same length of time. Figure 6.5 shows the atom cloud temperature after molasses cooling, recorded over $\sim$ 800 s with and without the magnetic compensation system engaged. The times presented on the abscissa refer to the time that the first image in the ballistic expansion was recorded. Each temperature measurement takes around 30 s. The standard error of the mean temperatures are inset. The compensation system reduces fluctuations in the molasses temperature by a factor of 1.52 horizontally and 2.42 vertically.

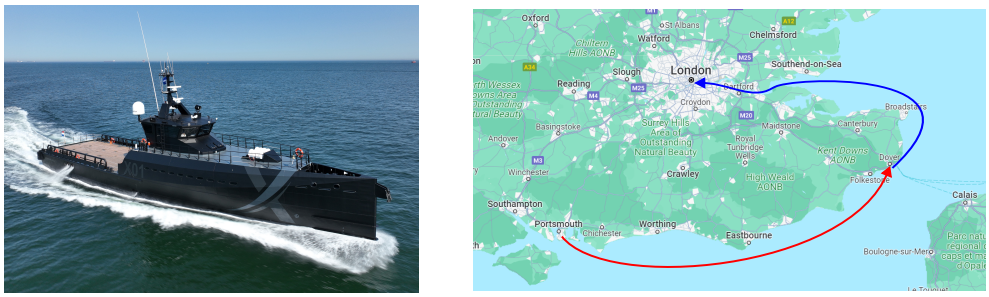
6.3 Sea trials

The early adopters of quantum enhanced inertial navigation systems are expected to be military end-users operating in a maritime environment. To gain experience of working in this environment, we have partnered with the Royal Navy to test our current demonstrator at sea.

6.3.1 XV Patrick Blackett

To facilitate maritime field trials, the Navy provided access to the NavyX research vessel the XV Patrick Blackett[2]. Figure 6.6a shows the XV Patrick

[2]The Physics department at Imperial College London is named after Patrick Blackett, who served as head of department from 1953-1963. NavyX christened their research vessel in honour of the same Patrick Blackett – the only Naval officer to be awarded a Nobel prize.



(a) (b)

Figure 6.6: (a) The XV Patrick Blackett research vessel which was used as the moving platform for two mobile field trials.[83]. (b) Map of the route taken during the Navy ship trials. The routes from Portsmouth to Dover (red) and from Dover to London (blue) each took one day of sailing. On the return journey, the same routes were taken in reverse.

Blackett, a modified Damen FCS 4008 fast crew supplier, which is around 42 m in length and can travel up to 20 kn ($\approx 10.3\,\mathrm{m\,s^{-1}}$) [84]. The experiment was installed into the NavyPOD and brought into operation at QinetiQ's technology centre, 6 km outside of Portsmouth. The system was switched off in preparation for transportation to the ship, to prevent potential damage to the laser in transit. Figure 6.7a shows the POD, containing the quantum sensor, after being craned onto the back of a lorry at the QinetiQ site, before being driven to Her Majesty's Naval Base (HMNB) Portsmouth, 10 km away. Figure 6.7b shows the POD, containing the quantum sensor, being craned onto the back of the XV Patrick Blackett, while alongside at the docks.

During the trials, the experiment was housed inside a POD, which was secured on the rear deck of the ship, while all researchers were situated inside the main body of the ship, running the experiment remotely. The ship's engines are situated underneath the deck where the POD was placed. The route taken during the trials is shown in figure 6.6b. During the ~ 2 h period while the ship was prepared to set sail, the experiment was switched on and set up to begin acquiring data. After embarking, there was a period of ~ 1 h while the ship remained within the dock, waiting for a slot to be allowed out of port. During this time, all tools and equipment were secured within the POD, which was then sealed, and researchers no longer had physical access to the experiment. The first day involved around 7 h of sailing time, with



(a) (b)

Figure 6.7: (a) Photograph of the NavyPOD, containing the quantum sensor, after being loaded onto a lorry for transportation from the QinetiQ technology centre to the HMNB Portsmouth. (b) Photograph of the POD being craned onto the XV Patrick Blackett from HMNB Portsmouth docks.

most of the time being spent in the open sea, more than 10 km from the shore. After the first day, the ship docked in Dover, and the experiment was inspected and prepared for the next day. The second day began at around 6am [3] where, again the ship remained in the port for around an hour before entering open waters. The ship travelled for around 5 h before entering the mouth of the Thames, where the ship's speed was reduced and vibrations of the ship also significantly decreased. Around 3 h later, we docked at HMS President in central London. The experiment was switched off and secured, and remained onboard the XV Patrick Blackett for ten days before the return journey. The second sea trial followed the same path as shown in figure 6.6b but in reverse, again with around 7 h of sailing per day. When arriving back in Portsmouth, the experiment was removed from the ship and driven back to the QinetiQ facility outside the city.

6.3.2 Vibrations

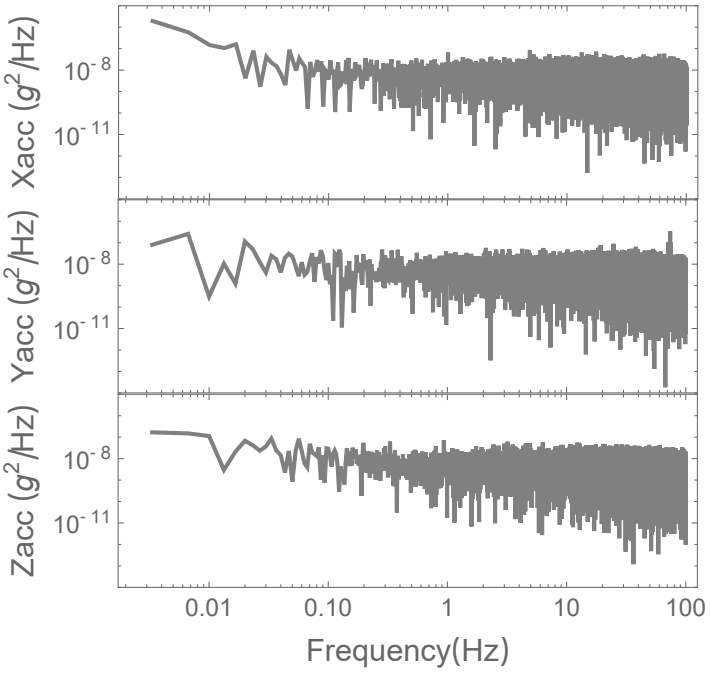
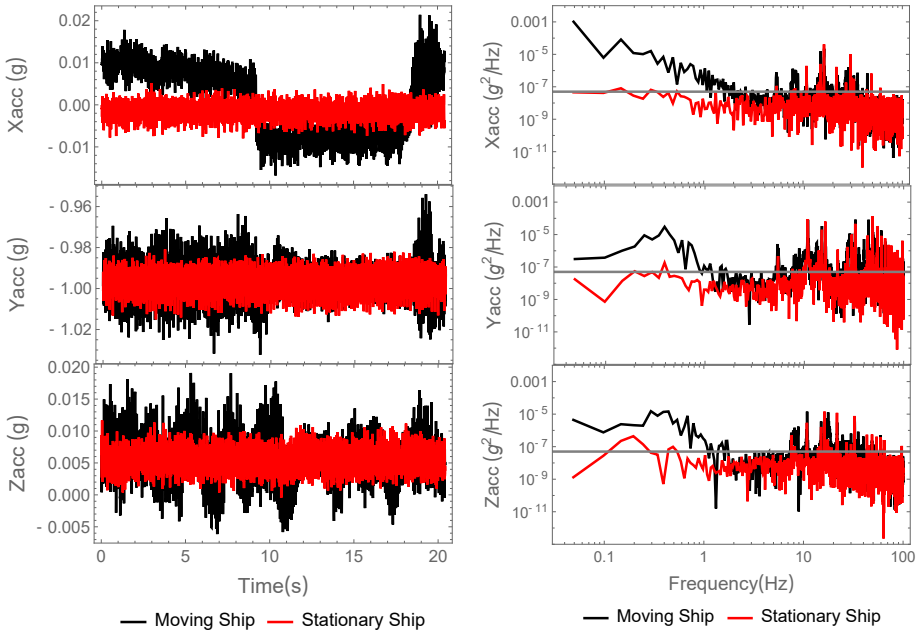


Figure 6.8: Power spectra of vibration data taken in the laboratory before the sea trials. This was used as a benchmark to measure increases in vibration due to the ship's motion.

[3]Preceded by a frantic last minute run along the seafront to the ship in fear of missing the time of departure.

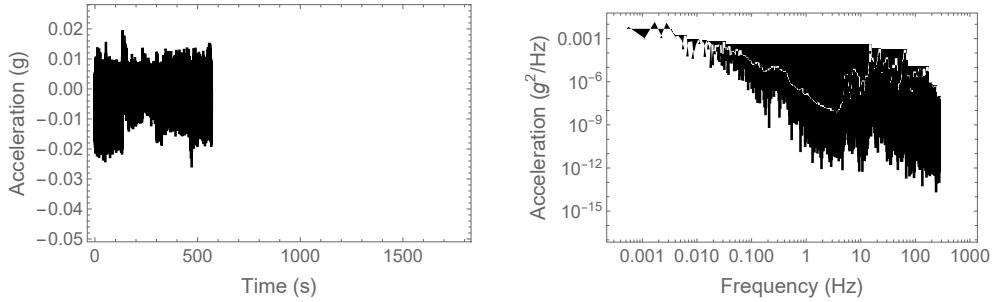


(a) (b)

Figure 6.9: (a) Time-series acceleration data taken during the mobile field trials with both a stationary and moving ship. The acceleration axes are (X) side to side across the ship, (Y) vertical, (Z) along the ship's direction of travel. During the stationary data, the ship's engine was switched on. The accelerometer was placed on the baseplate of the optical layer, as close as possible to the laser system. (b) Power series of the data shown in (a). The grey line shows the white noise level of the vibrations observed in the laboratory.

Before the field trials, a 200 Hz bandwidth, three axis accelerometer was placed on the baseplate of the optical box, next to the laser system, to measure the vibrations in laboratory conditions. Figure 6.8 shows the power spectra of the vibration data. In all three directions, the data shows white noise over almost the entire frequency range, at the level of around $5 \times 10^{-8}\,\mathrm{g^2\,Hz^{-1}}$. This was used as a benchmark to compare vibration data taken onboard the ship during the subsequent field trials.

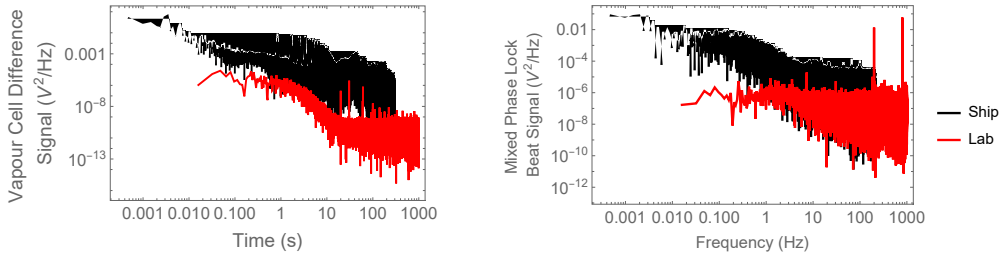
Moving platforms typically suffer from significantly more vibrations than a conventional quantum physics laboratory. Figure 6.9a shows the acceleration vibrations of the XV Patrick Blackett measured as a function of time using a MEMS accelerometer (bandwidth 200 Hz), while alongside at HMNB Portsmouth with the ship's engines on, and while moving in gentle waters (sea state 1) through the Solent strait. The accelerometer was placed on the baseplate of the optical box, next to the laser system.



(a) (b)

Figure 6.10: Time-series (a) and power spectrum (b) data taken with a 2 kHz bandwidth accelerometer along the ship travel direction during the second moving ship trial.

Figure 6.9b shows the power spectra corresponding to the time series data from figure 6.9a. The grey line shown is the level of white noise observed in the laboratory vibration data shown in figure 6.8. There is little difference between the vibration noise, alongside and while moving, at frequencies above 1 Hz, but both show increased vibrations compared to the laboratory data. This shows that the vibration from the ship's engines does not change significantly when stationary or moving, but contributes to most of the vibrations between 1 Hz and 100 Hz. Below 1 Hz, the moving vibrations are between 10 and 1000 times larger than when stationary due to the motion of the ship through the water. The stationary data shows white noise at a similar level to the laboratory data below 1 Hz. This shows that the majority of vibrations at this frequency are due to the boat's motion. During the second sea trial, data was also recorded using the 2 kHz bandwidth quartz oscillator accelerometer attached to the back of the Raman mirror. Figure 6.10 shows the recorded acceleration data, as well as the power spectrum. The accelerometer only has one axis of measurement and was oriented along the ship's direction of travel. Similarly to the z-axis data in figure 6.9, there is a significant increase in the power spectrum below 1 Hz. However, between around 10 Hz and 100 Hz, there is a significant increase for the quartz oscillator data. It is not obvious what the cause of this increased vibration is, but the variation in spectra for the two sensors is most likely due to the difference in position of the accelerometers while taking the data. In future trials, it will be useful to measure vibration data at various positions on the experiment, to gain more information about how vibrations can propagate through the system, and indicate where damping materials may be necessary.



(a) (b)

Figure 6.11: Vapour cell lock difference signal (a) and phase lock error signal (b) power spectra for both the mobile field trial and in the laboratory.

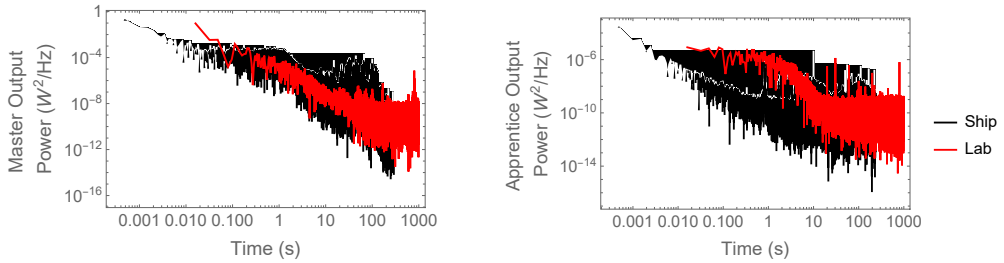
6.3.3 Laser and Laser Lock Noise

Over the course of the mobile field trials, challenges with the laser lock stability were encountered. Laser frequency noise can have a range of causes, but a common source is motion of components within the laser cavity. Increased frequency noise was observed at several points during the mobile field trials, with unlocking being more frequent during rougher periods of the journey. All data presented in this section was recorded with the Master and Apprentice lasers stabilised to the cooling and repumper frequencies respectively throughout.

Figure 6.11a shows a comparison of the power spectra of the vapour cell lock difference signal in the laboratory and during the ship trial. The spectrum is around three orders of magnitude larger on the ship than in the laboratory at all measured frequencies. As the vibration data in figure 6.9, shows increased vibrations on the ship over the same frequency range, it is likely that this is the cause of the increased Master frequency noise. Figure 6.11b shows the power spectrum of the mixed pahse lock beat (MPLB) signal taken over the same time period. As for the vapour cell lock difference signal, the MPLB signal spectrum is larger than the laboratory data at all frequencies within the measured range. At frequencies below 1 Hz, the MPLB spectrum is around four orders of magnitude larger. Above 10 Hz, the spectrum shows white noise, two orders of magnitude larger than seen in the laboratory. This is also likely caused by vibrations of the experimental system while in motion.

Figure 6.12 shows power spectra of the Master and Apprentice output powers taken during the same time period as the lock data in figure 6.11. The Master spectrum shows little difference to the laboratory data over the whole frequency range. The Apprentice power shows lower oscillation than in the laboratory at frequencies below 10 Hz, with similar spectra at higher frequen-

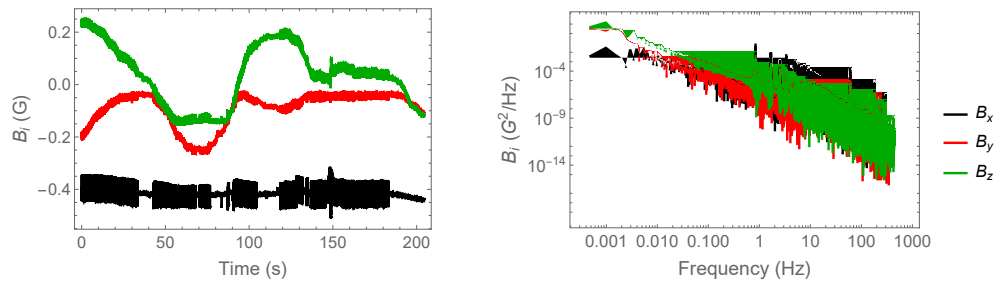
cies. Further investigation will be performed in the near future to investigate why this difference is observed at low frequencies.



(a) (b)

Figure 6.12: Power spectra for both Master (a) and Apprentice (b) optical output power taken during the mobile field trials and in the laboratory.

6.3.4 Magnetic Fields



(a) (b)

Figure 6.13: (a) Time series data showing the magnetic field in the NavyPOD during the mobile field trials. The ship was travelling along the south coast of the UK, from east to west. The coordinate axes are: x- side to side of the ship, pointing roughly along Earth's magnetic field, y- vertically, z- along the ship's direction of travel. (b) Power spectrum of the data shown in (a). The peaks at 1 Hz and higher harmonics are due to the coils on the experiment itself.

In our laboratory in London, the Earth's magnetic field has magnitude of around 480 mG, orientated 0.8 ° from grid north (British National Grid) [85]. For most experiments this constant background field can be cancelled by applying fixed currents through the bias compensation coils. At sea, there are few magnetic dipoles which can generate fields to perturb the quantum sensor. However, a ship is free to move on the surface of the water, changing the projection of the Earth's magnetic field onto the apparatus. Figure 6.13a shows the magnetic field recorded using a three-axis magnetic flux gate inside the POD over 200 s, while the ship was moving along the south coast.

Figure 6.13b shows the corresponding power spectrum. The peaks at 1 Hz, and corresponding harmonics up to around 10 Hz, result from magnetic fields applied during the experimental sequence (predominantly through the MOT coils) which was running throughout. The majority of variation in the magnetic field is at frequencies lower than 1 Hz. This will be effectively cancelled out by the magnetic compensation system, which works at the repetition rate of the experiment, $\sim$ 1 Hz. Faster time-varying magnetic fields can induce phase shifts on the interferometer by altering the detuning of each interferometry pulse. This will be discussed in detail, and the compensation system will be upgraded to account for such magnetic fields, in a future PhD thesis.

6.3.5 Laser Cooling and Cloud Temperature

Non-zero magnetic fields during the molasses stage of the experimental sequence significantly decrease cooling efficiency. For a change in magnetic field of 400 mG along the z direction, as in figure 6.13, molasses temperatures of $T_y = 67\,\mu K$ and $T_z = 39\,\mu K$ are predicted from characterisation measurements from the lab. At this temperature, in comparison to the temperatures measured in the laboratory, the density of the atomic cloud after 100 ms of expansion will be 3.2 times lower, and the spread in velocities will be 2.8 times higher along the Raman beam direction. Both of these factors will cause an increase in interferometer measurement noise. Figure 6.13b shows that the magnetic field noise on the ship is dominated by low frequency components, below 1 Hz. Because the dominant magnetic field variations occur on a time scale shorter than our experimental duty cycle ($\sim$ 1 s), we employed a sample and hold correction scheme to null the magnetic field at the atom position. Before leaving dock, stray magnetic fields were cancelled by manually setting the currents in the bias coils to maximise the cloud density after molasses cooling. While at sea, only the compensation system was used

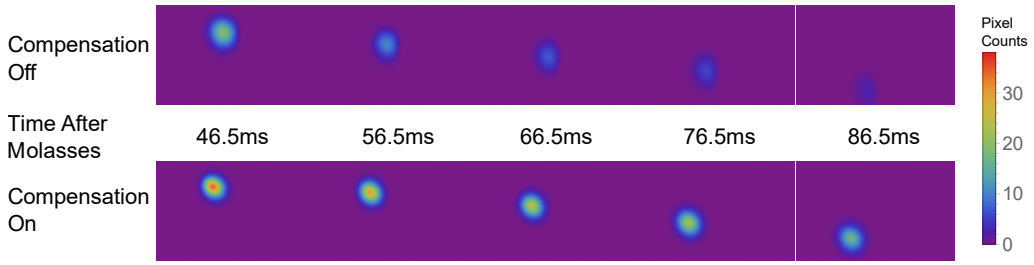


Figure 6.14: Expansion of the atom cloud after molasses cooling on the moving ship, with and without magnetic field compensation. The colour map is normalised to the maximum pixel count of the first image with compensation switched on.

to null changing fields.

Figure 6.14 shows camera images of the free falling atom cloud taken after the molasses cooling stage, with and without the compensation system engaged. The atoms are excited using the two vertical MOT beams containing 25 mW of cooling light and 2.5 mW of repump light. The camera exposure is 500 µs. The colour map is normalised to the maximum pixel count of the first compensated image. The data taken with compensation on has a higher cloud density throughout the images, compared with the images without magnetic compensation. The cloud position is also clearly shifted towards the right of the images for the non-compensation data, due to uncancelled background magnetic fields moving the position at which the atom cloud formed. This caused the cloud to clip the edge of the vertical MOT beams during this measurement.

Figure 6.15 shows the ballistic expansion of the atom cloud while the ship was moving, with the compensation system engaged. We observe horizontal and vertical cloud temperatures of 4.52 µK and 5.77 µK respectively, which is comparable to the 3.93 µK and 5.17 µK observed in the lab. A small oscillation in the cloud widths around the line of best fit can be observed, and correlates with the large vibrations at frequencies below 1 Hz shown in figures 6.9b and 6.10b, as well as the increase in low frequency vapour cell lock dif-

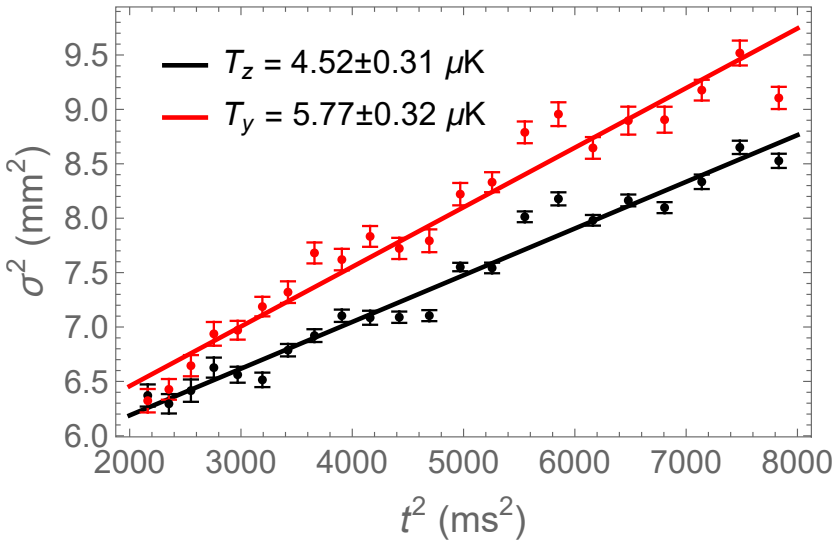


Figure 6.15: Atom cloud width measurement taken during the ship trial with the magnetic field compensation system engaged and with the ship moving in a straight line. The measured temperatures from the linear fits are shown inset.

ference signal oscillation, shown in figure 6.11a. Without the compensation system, reliable temperature measurements were not possible.

Background magnetic fields will also affect the position of the magnetic field zero of the quadrupole used by the MOT, relative to the intersection of the laser beams. This can have the knock-on effect of the atoms being outside the detection region. Figure 6.16 shows the centre-of-mass position and width of the atom cloud 40.5 ms after the molasses stage. Both the cloud position and width shows less variation when the compensation system is engaged. This is consistent with both the clipping of the atom cloud, and the reduced cloud density shown in figure 6.14, when the compensation system was switched off.

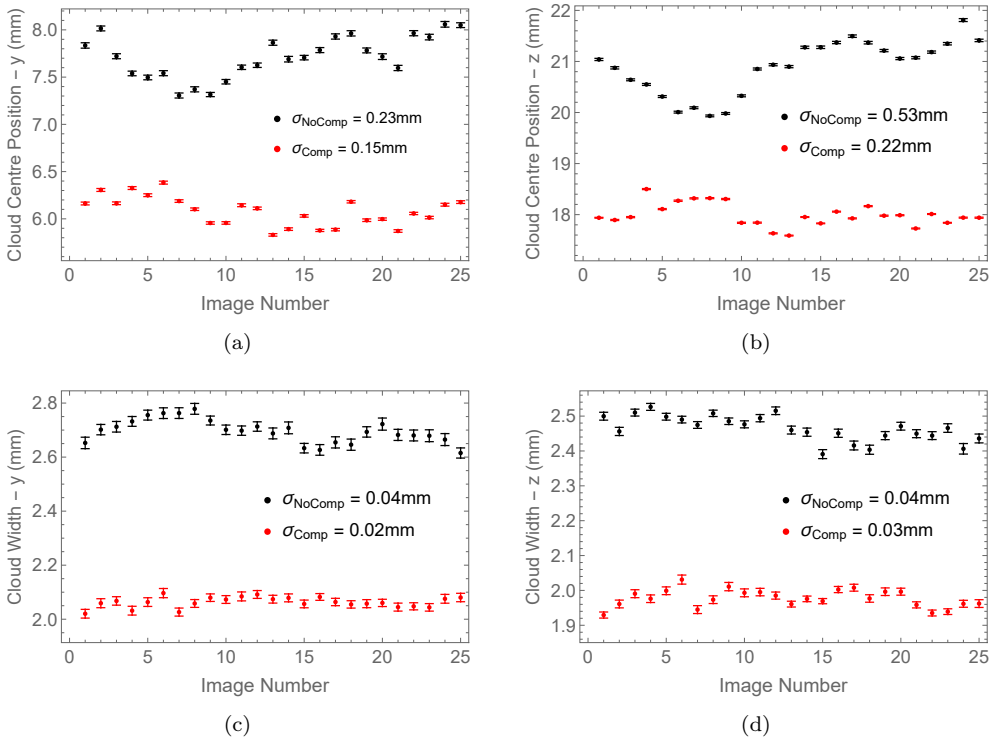


Figure 6.16: Atom cloud centre position ((a) and (b)) and width ((c) and (d)) variation at a constant time after molasses cooling both with and without magnetic field compensation. Camera images were repeatedly taken at 40.5 ms after the molasses ramps and the images were integrated along each pixel direction, where y is vertical and z is horizontal. No clipping of the atom cloud on the detection beams was observed for any of the images. No launches were applied during any of the experimental shots. The plot legends show the standard deviations of each set of data.

6.3.6 Coherent Control

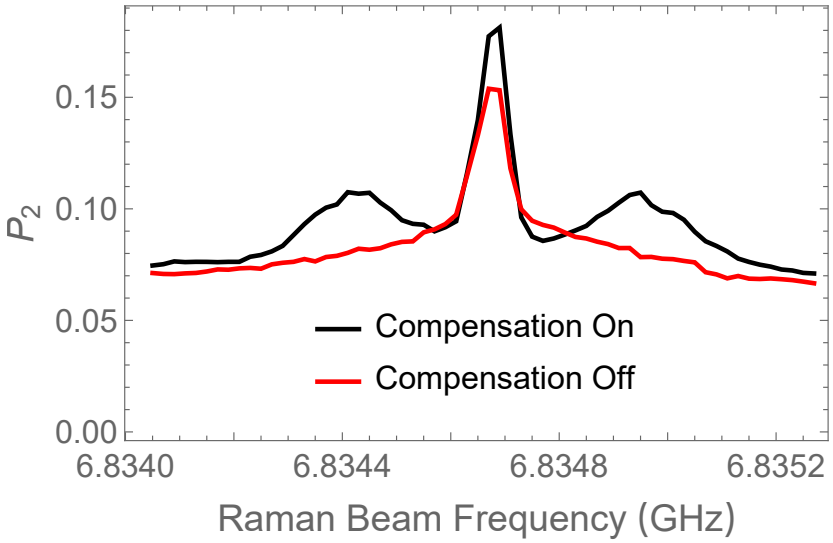


Figure 6.17: Raman spectra taken during the first mobile field trial both with and without magnetic compensation engaged. The Raman pulse duration for both spectra was 10 µs. State selection stages one and two were performed but no further stages were used.

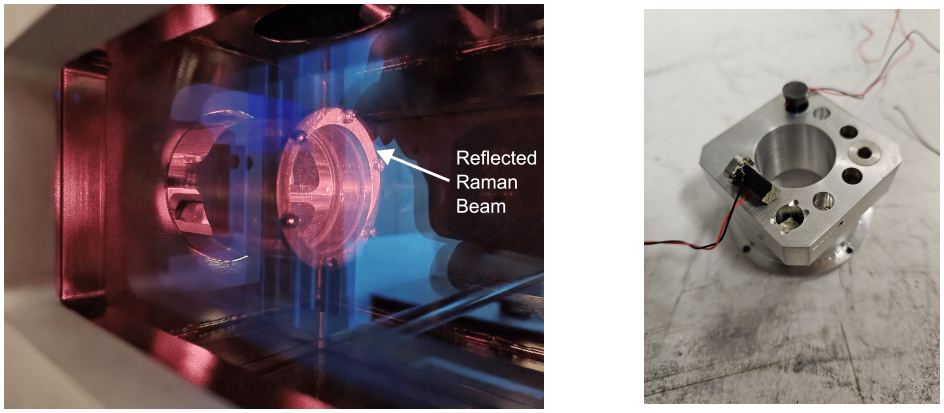
Figure 6.17 shows Raman spectra obtained while moving at sea, with and without the magnetic compensation system engaged. The Raman pulse duration was 10 µs and a horizontal launch velocity of 12 cm s^{-1} was applied. State selection stages one and two were performed before the Raman pulse. Without magnetic field compensation, only a co-propagating peak in the Raman spectra could be observed, on top of a wide pedestal. This is consistent with a high temperature cloud, above around 30 µK. The pedestal also appears to be centred at ν_{hf}, which shows that the moving molasses did not effectively launch the atoms when the compensation system was not engaged. With the magnetic field compensation engaged, the counter propagating Raman peaks are clearly visible, 250 kHz from the co-propagating peak. While some coherent control was performed, a full interferometer was not observed. It was not established why this was the case during the trial, as time constraints prevented further investigation.

6.4 Ruggedness

After each field trial, a review of the apparatus was conducted to identify points of weakness and failure. The most frequent impact of the trials was the misalignment of optics due to system vibrations. This was very easily and

quickly corrected, but future versions of the experiment will include improved damping of the system to prevent such misalignments from occuring. The following sections will describe two more significant sources of failure in the experimental setup, and how they will be mitigated in the future.

6.4.1 Raman Mirror Mount



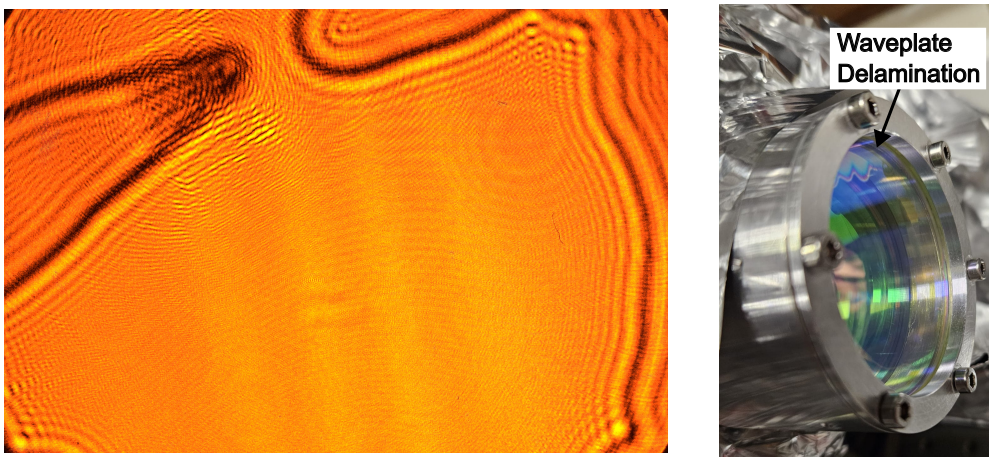
(a) (b)

Figure 6.18: (a) Camera image of the scatter from the retro-reflected Raman beam after the mirror mount piezo had collapsed. The camera is pointed towards the end of the Raman telescope. The reflected beam should be well aligned to the telescope, but most of the light scatter is on one side of the optics mount, showing significant misalignment. (b) Photograph of the broken piezoelectric actuator which caused the Raman mirror misalignment while in-vacuum.

The mount for the Raman mirror used in this transportable demonstrator is based on a design successfully used in the Imperial laboratory accelerometers and gyroscopes for some time. However, trials revealed a weakness in this design when deployed in a high vibration environment.

Figure 6.18a shows the end of the Raman telescope, with the reflected beam clipping the edge of one side, indicating a misalignment of the Raman mirror. After removing the mirror from the science chamber, it was discovered that the piezo-electric actuators used to align the mirror had sheared in two, resulting in a misalignment of around 15 °. Figure 6.18b shows the mirror mount and broken piezo. The timing of this shearing event is unclear. A new gimballed mirror mount with additional restraints to help prevent hyperflexion of the piezos in noisy environments is currently being developed.

6.4.2 Raman Telescope



(a) (b)

Figure 6.19: (a) Camera image of the Raman beam taken through the Raman window. The camera was positioned at the same distance from the Raman mirror as the atoms. (b) Photograph showing part of the pattern on the telescope quarter waveplate which caused the aberration seen in (a). The waveplate is made up of several layers of substrate, so it is likely that the different layers had delaminated to cause this pattern.

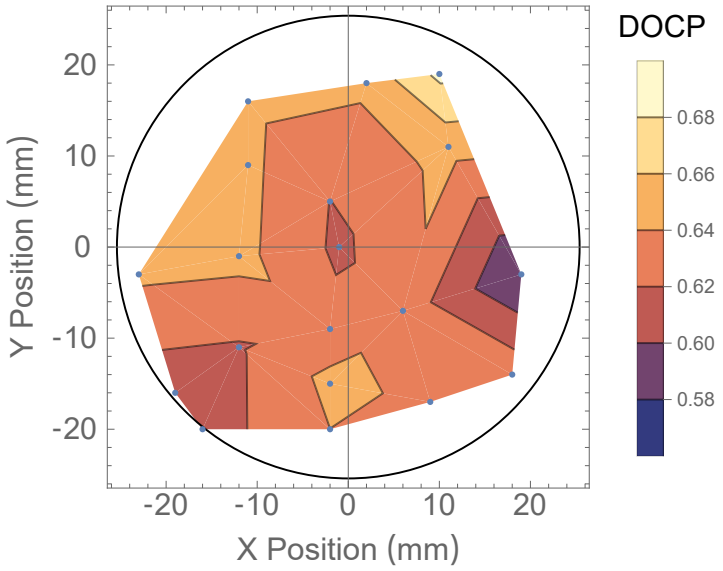


Figure 6.20: Measured degree of circular polarisation across the Raman telescope after it was damaged and removed from the vacuum. The blue points show the positions measured and the colour scale is shown in the legend.

Inspection of the Raman telescope after the trials revealed damage to one of the telescope optics. Figure 6.19a shows an ex-vacuo image of the Raman beam, 30.5 cm from the quarter waveplate. The dark lines and diffraction fringes result from a delamination of the waveplate, seen in figure 6.19b. Figure 6.20 shows a contour plot of the measured degree of circular polarisation (DOCP), as defined in equation (5.8) at different positions in the Raman beam, using the method described in section 5.4.1.2. Firstly, the overall DOCP decreased by around 20%, which means that a significant amount of Raman beam power was not of the correct polarisation to drive counter-propagating Raman transitions. There are also changes of up to 10% in the DOCP across the beam, which led to changes in differential light shift across the atom cloud, giving each atom a slightly different two-photon detuning. When the damage to the telescope occurred is also unclear, and investigations into its cause are ongoing. Preliminary findings suggest that localised pressure points, arising from the retaining ring, stressed the waveplate to the point of breaking under the influence of high vibrations. A new design for the retaining ring which reduces pressure on the waveplate is currently under development.

6.5 Lessons Learned During Sea Trials

Deploying quantum sensors outside of a laboratory environment presents significant technical and practical challenges. Here, I will review some of the lessons learned from our first maritime tests. I hope this will help steer development of a more robust system and help those continuing this work on future trials.

Electrical power - We typically power our quantum sensor from a lithium-ion battery, under constant trickle charge. During trials we were unable to charge this battery from the ships generators. The reason for this is currently not well understood, but preliminary investigations suggest that the protection circuitry of the battery rejected the input supply because the ship's ground is different to a domestic mains supply or due to high-frequency noise on the input. The battery could be successfully charged from shore supplies, while alongside, and could power the entire system for 5 hours if fully charged. Once the battery ran flat, the experiment was connected directly to the ship's power. However, this is noisy and unreliable[4], and reduced the total operating time available. Using a maritime battery during future

[4]During cleaning of the decks it was observed that the combined power drawn by our quantum sensor and the crew's vacuum cleaner was enough to trip the generator.

trials will help prevent unnecessary down-time of the experiment.

Pressure - We observed that the pressure in the science chamber, recorded using the ion pump current, increased during the field trials, peaking at a maximum value of 7×10^{-7} mbar, compared to a pressure of 2×10^{-8} mbar recorded while in the Portsmouth HMNB. This coincided with a ten-fold reduction in MOT atom number. Back in the lab, after the trial, the ion pump current continued to fluctuate by up to two orders of magnitude, although the MOT atom number returned to the pre-trial level of around 8×10^{8}. We attribute the reduced MOT atom number during the trial to a genuine increase in pressure caused by out-gassing of the sublimation pump caused by mechanical agitation[5]. The ion pump current fluctuations after the trial appear to result from an increase in leakage current, potentially caused by the out-gassing spikes. An independent cold cathode pressure gauge, installed after the trial, recorded a consistent pressure of 4×10^{-8} mbar after the test. Alternative pumps, less effected by mechanical agitation, would improve the background pressure that can be achieved during trials, and therefore the coherence times of the interferometer. New pump free vacuum technologies may prove to deliver ultimate performance, although more testing is required.

Laser performance - The feedback loops stabilising the Master and Apprentice lasers struggled during trials. The birefringent filter of the Apprentice laser was particularly affected, resulting in regular 2 GHz mode-hops. This ultimately limited the operational time available during trials. Further mechanical damping of the system as a whole, as well as targeted local damping of key optical components are underway in preparation for future trials.

[5]Based on discussion with the pump manufacturer.

Chapter 7

Conclusion and Future Work

7.1 Summary of this work

During this PhD I have built Imperial's first transportable quantum accelerometer. The system loads more the 10^9 atoms in 400 ms in a 3D MOT, loaded from a $2D^+$ MOT. Sub-Doppler cooling is then used to cool the trapped atomic cloud to around 5 µK, and launch the atoms both vertically and horizontally using a moving molasses technique. Next, atoms are efficiently prepared, with a narrow velocity class, in the $|F = 1, m_F = 0\rangle$ hyperfine state through the use of six state preparation and blowaway steps. A custom telescope has been constructed to provide collimated, circularly polarised light to drive stimulated Raman transitions in the experiment. Interference fringes with a contrast of 0.139 ± 0.004 for an interferometer time of 20 ms have been shown in the laboratory, after preliminary optimisation of the contrast. Field trials have been undertaken with the demonstrator, alongside the Royal Navy, characterising its robustness to transportation, and highlighting parts of the apparatus where improvements are needed to work in a turbulent environment.

I have characterised the performance of my transportable demonstrator in the laboratory and undertaken an initial comparison of its performance in the field with the lab. This is a critical first step towards developing a robust and reliable sensor that can operate as well in the field as it does in the lab. As a result of the work undertaken as part of this PhD, and after implementing the changes described in chapter 6, acceleration sensitive fringes have now been demonstrated onboard a moving train. This data will be presented and described in detail in a future PhD thesis. Development of the Imperial sensor remains ongoing.

7.2 Outlook

7.2.1 Current Landscape of Atom Interferometry for Navigation

The development of atom interferometers for navigation is already a global endeavour. Research groups have demonstrated gravimeters [86] and gravity gradiometers [87] in the field, and the technology has even developed into commercial products, with gravimeters sold by AOSense [88], Vector Atomic [89], and Muquans [90]. Despite the advancements in gravimeter technology, only one other group, based in France, has publicly demonstrated a horizontal quantum accelerometer on a moving platform [91, 92].

7.2.2 Next steps for this sensor

The position error for current, classical, inertial navigation systems is limited by the bias drift of the underpinning inertial sensors. Quantum sensors offer the advantage of much smaller drift, allowing more accurate long-term navigation. A key next step for characterising the performance of transportable quantum sensors will be to directly measure the bias drift in the field. Preliminary work on this is already underway using one of the Imperial College laboratory-based systems [44]. In the lab, colleagues have shown that the Allan deviation for the interferometer noise averages down at $1/t$ for over 18 hours, corresponding to a drift $< 1\,\mathrm{ng\,h^{-1}}$. To make an absolute measurement of the relative drift rate, a comparison to second, independent, sensor is required. A second transportable system is currently under construction and will be presented in future work.

The long term aim of creating a full navigation system will involve the inclusion of multiple axes of both acceleration and rotation measurement. The system built during this PhD was designed to also function as a gyroscope, and future work on this experiment will also be to demonstrate the effectiveness of both acceleration and rotation measurements in the field.

More field trials on a range of different moving platforms are planned for the near future, which will allow further testing of how the system performs in new environments. The work undertaken in this PhD will continue to highlight necessary upgrades to the system, most notably in the improvement of vibration isolation and improvement of the laser frequency stability.

Bibliography

[1] Hilary Costa, Erin Sprout, Santani Teng, Melissa McDaniel, Jeff Hunt, Diane Boudreau, Tara Ramroop, Kim Rutledge, and Hilary Hall. Navigation - National Geographic Society - Education, Oct 2023. https://education.nationalgeographic.org/resource/navigation/.

[2] Chris Whitty and Mark Walport. *Blackett review: Satellite-derived Time and Position: A Study of Critical Dependencies*. Government Office for Science, 2018.

[3] Charles Jeffrey. *An introduction to GNSS: GPS, GLONASS, Galileo and other Global Navigation Satellite Systems*. NovAtel, 3 edition, 2010.

[4] Léon Foucault. Astronomie: Sur une nouvelle démonstration expérimentale du mouvement de la Terre, fondée sur la fixité du plan de rotation. *Comptes rendus hebdomadaires des séances de l'Académie des Sciences*, 35:135–138, 1852.

[5] M. Schuler. Storung von Pendel-und Krieselapparaten durch die Beschleunigung des Fahrseuges. *Physik Zeitschr*, 24(344), 1923.

[6] W. Wrigley. History of Inertial Navigation. *NAVIGATION: Journal of the Institute of Navigation*, 24(1), 1977.

[7] EE Learning Center Bill Schweber. PIGAs can indeed fly — and are still the best, Part 2: Operation, Mar 2022. https://www.sensortips.com/featured/pigas-can-indeed-fly-still-best-part-2-operation-faq/.

[8] Analog Devices. Accelerometer and gyroscopes sensors: Operation, sensing, and applications, Nov 2022. https://www.analog.com/en/technical-articles/accelerometer-and-gyroscopes-sensors-operation-sensing-and-applications.html.

[9] Ericco Inertial System. How does the quartz accelerometer work?, Jul 2023. https://medium.com/@ericcointernational001/how-does-the-quartz-accelerometer-work-1ded5ec7171a.

[10] W. T. Pike, I. M. Standley, and S. Calcutt. A silicon microseismometer for Mars. In *2013 Transducers & Eurosensors XXVII: The 17th International Conference on Solid-State Sensors, Actuators and Microsystems (TRANSDUCERS & EUROSENSORS XXVII)*, pages 622–625, 2013.

[11] iXblue. Marins M11, Mar 2023. https://www.ixblue.com/store/marins-m11/.

[12] T. Young. Ii. the Bakerian lecture on the theory of light and colours. *Philosophical Transactions of the Royal Society of London*, 92:12–48, 1802.

[13] Albert Abraham Michelson and Edward W. Morley. On the relative motion of the Earth and the luminiferous ether. *American Journal of Science*, s3-34:333 – 345, 1887.

[14] L. Zehnder. Ein neuer Interferenzrefraktor. *Zeitschrift fr Instrumentenkunde*, 11:275–285, 1891.

[15] R. Colella, A. W. Overhauser, and S. A. Werner. Observation of Gravitationally Induced Quantum Interference. *Phys. Rev. Lett.*, 34:1472–1474, Jun 1975.

[16] Mark Kasevich and Steven Chu. Atomic interferometry using stimulated Raman transitions. *Phys. Rev. Lett.*, 67:181–184, Jul 1991.

[17] Estermann I. and A. Stern. Begung von molekularstrahlen- bending of molecular rays. *Z. Phys.*, 61, 1930.

[18] Helmut Rauch and Samuel A. Werner. *Neutron Interferometry: Lessons in Experimental Quantum Mechanics, Wave-Particle Duality, and Entanglement*. Oxford University Press, Jan 2015.

[19] O. Carnal and J. Mlynek. Young's double-slit experiment with atoms: A simple atom interferometer. *Phys. Rev. Lett.*, 66:2689–2692, May 1991.

[20] David W. Keith, Christopher R. Ekstrom, Quentin A. Turchette, and David E. Pritchard. An interferometer for atoms. *Phys. Rev. Lett.*, 66:2693–2696, May 1991.

[21] Stefan Gerlich, Sandra Eibenberger, Mathias Tomandl, Stefan Nimmrichter, Klaus Hornberger, Paul Fagan, Jens Tüxen, Marcel Mayor, and Markus Arndt. Quantum interference of large organic molecules. *Nature Communications*, 2:263, 04 2011.

[22] Roberto Colella and Albert W. Overhauser. Neutrons, Gravity, and Quantum Mechanics: Is it possible to observe gravitational effects in experiments in which quantum theory plays a dominant role? *American Scientist*, 68(1):70–75, 1980.

[23] Vincent Ménoret, Pierre Vermeulen, Nicolas Le Moigne, Bonvalot Sylvain, Philippe Bouyer, Arnaud Landragin, and Bruno Desruelle. Gravity measurements below 10^{-9} g with a transportable absolute quantum gravimeter. *Scientific Reports*, 8, 08 2018.

[24] Cristian D. Panda, Matt Tao, Miguel Ceja, Andrew Reynoso, and Holger Müller. Atomic gravimeter robust to environmental effects. *Applied Physics Letters*, 123(6):064001, 08 2023.

[25] Liang Hu, Nicola Poli, Leonardo Salvi, and Guglielmo M. Tino. Atom Interferometry with the Sr Optical Clock Transition. *Phys. Rev. Lett.*, 119:263601, Dec 2017.

[26] Holger Müller. Standard model of particle physics tested by the fine-structure constant. *Nature*, 588(7836):37–38, December 2020.

[27] J. B. Fixler, G. T. Foster, J. M. McGuirk, and M. A. Kasevich. Atom Interferometer Measurement of the Newtonian Constant of Gravity. *Science*, 315(5808):74–77, 2007.

[28] Peter Asenbaum, Chris Overstreet, Minjeong Kim, Joseph Curti, and Mark A. Kasevich. Atom-Interferometric Test of the Equivalence Principle at the 10^{-12} Level. *Phys. Rev. Lett.*, 125:191101, Nov 2020.

[29] G. Rosi, G. D'Amico, L. Cacciapuoti, F. Sorrentino, M. Prevedelli, M. Zych, C. Brukner, and G. M. Tino. Quantum test of the equivalence principle for atoms in superpositions of internal energy eigenstates. *Nature Commun.*, 8:5529, 2017.

[30] Xiao-Bing Deng, Yao-Yao Xu, Xiao-Chun Duan, and Zhong-Kun Hu. Precisely Mapping the Absolute Magnetic Field in Vacuum by an Optical Ramsey Atom Interferometer. *Phys. Rev. Appl.*, 15:054062, May 2021.

[31] J. K. Stockton, K. Takase, and M. A. Kasevich. Absolute Geodetic Rotation Measurement Using Atom Interferometry. *Phys. Rev. Lett.*, 107:133001, Sep 2011.

[32] Xuejian Wu, Zachary Pagel, Bola S. Malek, Timothy H. Nguyen, Fei Zi, Daniel S. Scheirer, and Holger Müller. Gravity surveys using a mobile atom interferometer. *Science Advances*, 5(9):eaax0800, 2019.

[33] Simon Templier, Pierrick Cheiney, Quentin d'Armagnac de Castanet, Baptiste Gouraud, Henri Porte, Fabien Napolitano, Philippe Bouyer, Baptiste Battelier, and Brynle Barrett. Tracking the vector acceleration with a hybrid quantum accelerometer triad. *Science Advances*, 8(45):eadd3854, 2022.

[34] T. Müller, M. Gilowski, M. Zaiser, P. Berg, Ch Schubert, T. Wendrich, Wolfgang Ertmer, and E. Rasel. A compact dual atom interferometer gyroscope based on laser-cooled rubidium. *The European Physical Journal D*, 53:273–281, 06 2009.

[35] Hayden J. McGuinness, Akash V. Rakholia, and Grant W. Biedermann. High data-rate atom interferometer for measuring acceleration. *Applied Physics Letters*, 100(1):011106, 01 2012.

[36] J. M. McGuirk, M. J. Snadden, and M. A. Kasevich. Large Area Light-Pulse Atom Interferometry. *Phys. Rev. Lett.*, 85:4498–4501, Nov 2000.

[37] Xuejian Wu, Fei Zi, Jordan Dudley, Ryan J. Bilotta, Philip Canoza, and Holger Müller. Multiaxis atom interferometry with a single-diode laser and a pyramidal magneto-optical trap. *Optica*, 4(12):1545–1551, Dec 2017.

[38] Tim Kovachy, Sheng-wey Chiow, and Mark A. Kasevich. Adiabatic-rapid-passage multiphoton Bragg atom optics. *Phys. Rev. A*, 86:011606, Jul 2012.

[39] Tommaso Mazzoni, Xian Zhang, Ruben del Aguila, Leonardo Salvi, Nicola Poli, and G. Tino. Large-momentum-transfer Bragg interferometer with strontium atoms. *Physical Review A*, 92, 10 2015.

[40] Pierre Cladé, Saïda Guellati-Khélifa, François Nez, and François Biraben. Large Momentum Beam Splitter Using Bloch Oscillations. *Phys. Rev. Lett.*, 102:240402, Jun 2009.

[41] P.Cladé. Bloch oscillations in atom interferometry. *La Rivisita del Nuovo Cimento*, 38:173–207, 2015.

[42] Xiaxi Cheng. *Building a Sensitive Atom Interferometer for Navigation*. Thesis, Imperial College of Science, Technology and Medicine Faculty of Natural Science Department of Physics, September 2019.

[43] Shane De Silva. *A 2D Atom Interferometer Accelerometer in the Horizontal Plane*. PhD thesis, Imperial College of Science, Technology and Medicine Faculty of Natural Science Department of Physics, May 2021.

[44] Nicola Bilton. *Development of a Two-Axis Cold Atom Interferometer System for Acceleration and Rotation Measurements*. PhD thesis, Imperial College of Science, Technology and Medicine Faculty of Natural Science Department of Physics, December 2022.

[45] Alan Corney. *Atomic and Laser Spectroscopy*. Oxford University Press, 10 2006.

[46] Pippa Storey and Claude Cohen-Tannoudji. The Feynman path integral approach to atomic interferometry: A tutorial. *J. Phys. II*, 4(11):1999–2027, 1994.

[47] Christian Schubert, Sven Abend, Matthias Gersemann, Martina Gebbe, Dennis Schlippert, Peter Berg, and Ernst Rasel. Multi-loop atomic Sagnac interferometry. *Scientific Reports*, 11, 08 2021.

[48] E. Collett. *Field Guide to Polarization*. Field Guides. Society of Photo Optical, 2005.

[49] Alan L. Migdall, John V. Prodan, William D. Phillips, Thomas H. Bergeman, and Harold J. Metcalf. First Observation of Magnetically Trapped Neutral Atoms. *Phys. Rev. Lett.*, 54:2596–2599, Jun 1985.

[50] E. L. Raab, M. Prentiss, Alex Cable, Steven Chu, and D. E. Pritchard. Trapping of Neutral Sodium Atoms with Radiation Pressure. *Phys. Rev. Lett.*, 59:2631–2634, Dec 1987.

[51] D. E. Pritchard, E. L. Raab, V. Bagnato, C. E. Wieman, and R. N. Watts. Light Traps Using Spontaneous Forces. *Phys. Rev. Lett.*, 57:310–313, Jul 1986.

[52] Steven Chu, J. E. Bjorkholm, A. Ashkin, and A. Cable. Experimental Observation of Optically Trapped Atoms. *Phys. Rev. Lett.*, 57:314–317, Jul 1986.

[53] J. Dalibard and C. Cohen-Tannoudji. Laser cooling below the Doppler limit by polarization gradients: simple theoretical models. *J. Opt. Soc. Am. B*, 6(11):2023–2045, Nov 1989.

[54] W.D. Phillips, P.D. Lett, S.L. Rolston, C.E. Tanner, R.N. Watts, C.I. Westbrook, C. Salomon, J. Dalibard, A. Clairon, and S. Guellati. Optical molasses: cold atoms for precision measurements. *IEEE Transactions on Instrumentation and Measurement*, 40(2):78–80, 1991.

[55] J. Schoser, A. Batär, R. Löw, V. Schweikhard, A. Grabowski, Yu. B. Ovchinnikov, and T. Pfau. Intense source of cold Rb atoms from a pure two-dimensional magneto-optical trap. *Phys. Rev. A*, 66:023410, Aug 2002.

[56] V. Letokhov, V. Minogin, and B. Pavlik. Cooling and capture of atoms and molecules by a resonant light field. *Soviet Journal of Experimental and Theoretical Physics*, 45:698, 03 1977.

[57] C.J. Foot. *Atomic physics*. Oxford University Press, USA, 2005.

[58] Daniel Steck. Rubidium 87 D Line Data. Jan 2003.

[59] D. J. Berkeland and M. G. Boshier. Destabilization of dark states and optical spectroscopy in Zeeman-degenerate atomic systems. *Phys. Rev. A*, 65:033413, Feb 2002.

[60] Alexander Dunning, Rachel Gregory, James Bateman, Nathan Cooper, Matthew Himsworth, Jonathan A. Jones, and Tim Freegarde. Composite pulses for interferometry in a thermal cold atom cloud. *Phys. Rev. A*, 90:033608, Sep 2014.

[61] Steffen Schmidt-Erbele. *Phase and Frequency Locking of Diode Lasers: TOPTICA Photonics AG*. 2022.

[62] Holger Müller, Sheng wey Chiow, Quan Long, and Steven Chu. Phase-locked, low-noise, frequency agile titanium:sapphire lasers for simultaneous atom interferometers. *Opt. Lett.*, 31(2):202–204, Jan 2006.

[63] Teodor Krastev. Axel Suite Software, 2019. https://axelsuite.com/.

[64] Hermann Uys, John D. Perreault, and Alexander D. Cronin. Matter-wave Decoherence due to a Gas Environment in an Atom Interferometer. *Phys. Rev. Lett.*, 95:150403, Oct 2005.

[65] L. Marcassa, V. Bagnato, Y. Wang, C. Tsao, J. Weiner, O. Dulieu, Y. B. Band, and P. S. Julienne. Collisional loss rate in a magneto-optical trap for sodium atoms: Light-intensity dependence. *Phys. Rev. A*, 47:R4563–R4566, Jun 1993.

[66] Magnus Haw, Nathan Evetts, Will Gunton, Janelle Van Dongen, James L. Booth, and Kirk W. Madison. Magneto-optical trap loading rate dependence on trap depth and vapor density. *J. Opt. Soc. Am. B*, 29(3):475–483, Mar 2012.

[67] P. Redhead. Hydrogen in vacuum systems: An overview. 671:243–254, 07 2003.

[68] S. Bali, K. M. O'Hara, M. E. Gehm, S. R. Granade, and J. E. Thomas. Quantum-diffractive background gas collisions in atom-trap heating and loss. *Phys. Rev. A*, 60:R29–R32, Jul 1999.

[69] Infleqtion. Quantum Cores, 2023. https://www.infleqtion.com/quantum-cores.

[70] Matthias Hauth. A mobile, high-precision atom-interferometer and its application to gravity observations. Mathemathisch-Naturwissenschaftlichen Fakultät Humboldt-Universität zu Berlin, 2015.

[71] Harold J. Metcalf and Peter van der Straten. *Laser Cooling and Trapping*. Springer-Verlag, New York, 1999.

[72] V. Schkolnik, B. Leykauf, M. Hauth, C. Freier, and A. Peters. The effect of wavefront aberrations in atom interferometry. *Applied Physics B: Lasers and Optics*, 120(2):311–316, August 2015.

[73] C Freier, M Hauth, V Schkolnik, B Leykauf, M Schilling, H Wziontek, H-G Scherneck, J Müller, and A Peters. Mobile quantum gravity sensor with unprecedented stability. *Journal of Physics: Conference Series*, 723:012050, Jun 2016.

[74] Pierrick Cheiney, Lauriane Fouché, Simon Templier, Fabien Napolitano, Baptiste Battelier, Philippe Bouyer, and Brynle Barrett. Navigation-Compatible Hybrid Quantum Accelerometer Using a Kalman Filter. *Physical Review Applied*, 10(3), Sep 2018.

[75] Norman G. Worku and Herbert Gross. Propagation of truncated Gaussian beams and their application in modeling sharp-edge diffraction. *J. Opt. Soc. Am. A*, 36(5):859–868, May 2019.

[76] S. Pollock, J. P. Cotter, A. Laliotis, and E. A. Hinds. Integrated magneto-optical traps on a chip using silicon pyramid structures. *Opt. Express*, 17(16):14109–14114, Aug 2009.

[77] David Guéry-Odelin, Johannes Söding, P Desbiolles, and Jean Dalibard. Strong evaporative cooling of a trapped cesium gas. *Optics Express*, 2:323–9, 05 1998.

[78] Omur Sezerman and Garland Best. Accurate alignment preserves polarization. *Laser Focus World*, 33(12):27–30, 1997.

[79] E. Collett. *Field Guide to Polarization*. Field Guides. SPIE Press, 2005.

[80] G. Dick, John Prestage, Charles Greenhall, and L. Maleki. Local Oscillator Induced Degradation of Medium-Term Stability in Passive Atomic Frequency Standards. 06 1990.

[81] Barrett B., Gominet P.-A., Cantin E., Antoni-Micollier L., Bertoldi A., Battelier B., Bouyer P., Lautier J., and Landragin A. Mobile and remote inertial sensing with atom interferometers. *Proceedings of the International School of Physics;Enrico Fermi;*, 188(Atom Interferometry):493–555, 2014.

[82] Royal Navy. Pods: Persistent Operational Deployment Systems. https://www.royalnavy.mod.uk/news-and-latest-activity/features/think-differently.

[83] Royal Navy. Navyx — Royal Navy- XV Patrick Blackett, Mar 2021. https://www.royalnavy.mod.uk/news-and-latest-activity/operations/united-kingdom/navy-x.

[84] Navy Lookout: Independent Royal Navy news and analysis, Jun 2023. https://www.navylookout.com/royal-navy-takes-delivery-of-new-experimental-vessel/.

[85] British Geological Survey. 2021 High frequency magnetic field induction coil data from Eskdalemuir Observatory, UK (Dataset) - NERC EDS National Geoscience Data Centre, 2022.

[86] Xuejian Wu, Zachary Pagel, Bola S. Malek, Timothy H. Nguyen, Fei Zi, Daniel S. Scheirer, and Holger Müller. Gravity surveys using a mobile atom interferometer. *Science Advances*, 5(9), Sep 2019.

[87] Ben Stray, Andrew Lamb, Aisha Kaushik, Jamie Vovrosh, Anthony Rodgers, Jonathan Winch, Farzad Hayati, Daniel Boddice, Artur Stabrawa, Alexander Niggebaum, Mehdi Langlois, Yu-Hung Lien, Samuel Lellouch, Sanaz Roshanmanesh, Kevin Ridley, Geoffrey de Villiers, Gareth Brown, Trevor Cross, George Tuckwell, Asaad Faramarzi, Nicole Metje, Kai Bongs, and Michael Holynski. Quantum sensing for gravity cartography. *Nature*, 602(7898):590–594, Feb 2022.

[88] AOSense Inc. Sensors for a quantum world, Mar 2023. https://aosense.com/products/atom-optic-sensors/gravimeter/.

[89] Vector Atomic Inc. Infinitesimal forces. enormous impact., 2022. https://vectoratomic.com/.

[90] Muquans. Absolute quantum gravimeter, 2021. https://www.muquans.com/product/absolute-quantum-gravimeter/.

[91] R. Geiger, V. Ménoret, G. Stern, N. Zahzam, P. Cheinet, B. Battelier, A. Villing, F. Moron, M. Lours, Y. Bidel, A. Bresson, A. Landragin, and P. Bouyer. Detecting inertial effects with airborne matter-wave interferometry. *Nature Communications*, 2(1), Sep 2011.

[92] Brynle Barrett, Laura Antoni-Micollier, Laure Chichet, Baptiste Battelier, Thomas Lévèque, Arnaud Landragin, and Philippe Bouyer. Dual matter-wave inertial sensors in weightlessness. *Nature Communications*, 7(1), Dec 2016.